Optofluidic Devices for Droplet and Cell Manipulation

Shao Ning Pei
Ming C. Wu, Ed.

Electrical Engineering and Computer Sciences
University of California at Berkeley

Technical Report No. UCB/EECS-2015-119
http://www.eecs.berkeley.edu/Pubs/TechRpts/2015/EECS-2015-119.html

May 15, 2015

Optofluidic Devices for Droplet and Cell Manipulation

By

Shao Ning Pei

A dissertation submitted in partial satisfaction of the

requirements for the degree of

Doctor of Philosophy

in

Engineering - Electrical Engineering and Computer Sciences

in the

Graduate Division

of the

University of California, Berkeley

Committee in charge:

Professor Ming C. Wu, Chair

Professor Michel Maharbiz

Professor Amy Herr

Spring 2015

Optofluidic Devices for Droplet and Cell Manipulation

Abstract

Optofluidic Devices for Droplet and Cell Manipulation

By

Shao Ning Pei

Doctor of Philosophy in Engineering - Electrical Engineering and Computer Sciences

University of California, Berkeley

Professor Ming C. Wu, Chair

The field of lab-on-a-chip offers exciting new capabilities for chemical and biological assays, including increased automation, higher throughput, heightened sensitivity of detection, and reduced sample and reagent usage. This area of study has seen remarkable progress in the last decade, with applications ranging from drug development to point-of-care diagnostics. The research presented herein focuses on the development of semiconductor-based optoelectrowetting (OEW) and optoelectronic tweezers (OET) platforms, which can respectively perform operations on droplets and cells/particles. This thesis discusses progress achieved on both OEW and OET platforms. For OEW, a novel optimization model has been developed to accurately predict the interaction of droplets, semiconductor layers, and a programmable DLP-based optical source. Consequently, parallel and arrayed droplet manipulation is now possible over a large operational area (cm × cm). In addition, critical droplet operations such as mixing, splitting, and dispensing have been demonstrated. As a biological application of OEW, this work will discuss the parallel, real-time, isothermal polymerase chain reaction detection of Herpes Simplex Virus Type 1 in droplet arrays. For OET, the effort in long-term culture of adherent mammalian single cells into clonal colonies will be discussed; OET surface functionalization enables large (0.5-mm-diameter) growth patches in which positioned single cells can adhere and proliferate. Lastly, the link between the OEW and OET devices and how both droplet and particle manipulation can be enabled on a unified platform will be presented.

To my parents, Yuanhang Pei (裴远航) and Xiaowei Ma (马晓威)

Contents

List of Figures and Tables

Acknowledgements

I would like to express my sincerest gratitude to my advisor Professor Ming C. Wu for his guidance throughout my research. His scientific acumen, clarity of thinking, and depth of knowledge in a great variety of topics never cease to amaze me. I would also like to thank the other members of my dissertation committee, Professor Michel Maharbiz and Professor Amy Herr, for reviewing this dissertation. I am grateful to all the members of the Integrated Photonics Lab, from whom I have learned immensely. I would especially like to thank Justin Valley for his mentorship at the beginning of my PhD career. In addition, I would like to acknowledge people in the optofluidics sub-group, with whom I had the pleasure of working closely: Arash Jamshidi, Hsan-Yin Hsu, Steven Neale, Kavit Kumar, Yi-Lun Wang, and Jodi Loo. Also, I am very grateful to my collaborators in Bioengineering - Professor Song Li, Tiffany Dai, and members of the Cell and Tissue Engineering lab. I would also like to acknowledge Professor Pei-Cheng Ku, Professor Euisik Yoon, Professor Raoul Kopelman and Dr. Brandon McNaughton, at the University of Michigan, who instilled in me the passion for research during my undergraduate days. Finally, I would like to thank my parents and my wife for their sacrifices, support, and love.

Chapter 1 Introduction

Fifty years ago, Gordon Moore, co-founder of Intel, observed that the number of transistors on integrated circuits doubles every 18 months. This famous observation, termed "Moore's law," has resulted in ever-decreasing circuit device sizing and more cost effective logic operations. Consequently, the revolutionary improvements in computing power have enabled explosive productivity and economic growth [1].

Since the beginning of this century, many scientists and engineers started to take a keen interest in applying Moore's law to biology, whereby a certain bio-technological process can be scaled up, automated, and miniaturized, the most successful of which so far has been Next-Generation Sequencing (NGS) [2]. However, despite the plethora of biomedical advances, the operation of many biological and chemical assays remains manual, time consuming, qualitative, and cumbersome. These biomolecular assays, generally involving the addition and extraction of small amounts of liquids, solids, and biological agents, are still most often being performed by scientists and technicians in wet laboratories using pipetting methods. For example, DNA library preparation for NGS is extremely tedious and requires much dedication from the scientist in the preparation of buffers, reagents, and treatment of cells and tissues. The whole process often takes hours, and any deviations from assay protocol will result in sequencing failure.

Therefore, there remains a strong need in biotechnology for increased automation, sample throughput, sensitivity of detection, and reduced sample and reagent usage (miniaturization). By moving away from traditional bulk analysis and instead focus on analyzing biological agents at the microscale and at the single-cell level will yield crucial quantitative insights into topics ranging from stem cell research to drug screening.

The above-mentioned need is well addressed by microfluidics based lab-on-a-chip (LOC) systems [3]. This multidisciplinary field concerns the design of systems that handles small quantity of fluids or biological agents to perform complex assays using chip-scale devices. Typical fluid volumes range from micro-liters to a femto-liter. The field has seen remarkable progress in the last decade, with applications ranging from cancer research to point-of-care diagnostics. Figure 1.1 shows a LOC technology roadmap, summarizing the remarkable technological progress and marketization of products made in the LOC field [4].

Specifically, LOC confers these major advantages:

1. Miniaturization – First, the size of biological analytes ranges from nanometers, such as DNA, to micrometers, such as mammalian cells. Encapsulation and interrogation of these analytes can be carried out effectively at the single cell level. Compared to bulk level analysis, this will result in previously unobservable insights into analyte behavior. Second, usage of costly reagents can be reduced per assay. Microfluidics based devices are easily scalable and adaptable to analyzing these biological agents.
2. Automation - Programmable handling of fluids and biological agents can be

conducted on LOC devices, reducing the need for manual fluidic operations. Furthermore, LOC systems can easily leverage well-developed microfabrication techniques from the semiconductor industry to quickly prototype and scale-up chip production.

3. Throughput - microfluidic systems can handle many samples simultaneously; the compartmentalization of fluids and biological agents can enable parallel processing, which dramatically increases sample throughput.
4. Sensitivity of detection - due to the smaller sample volumes, reactions occur faster and detection may occur at a lower detection threshold.

Consequently, LOC technology is a good candidate to apply Moore's law scaling to biological assays, where LOC fluidic piping and biological agents such as droplets/particles/cells are the analog of electrical wiring and electrical components such as transistors/resistors/ capacitors. The promise of ever-increasing automation and throughput, and scaling down of sample size in biotechnology will provide revolutionary improvements in cost, productivity, and quality of healthcare.

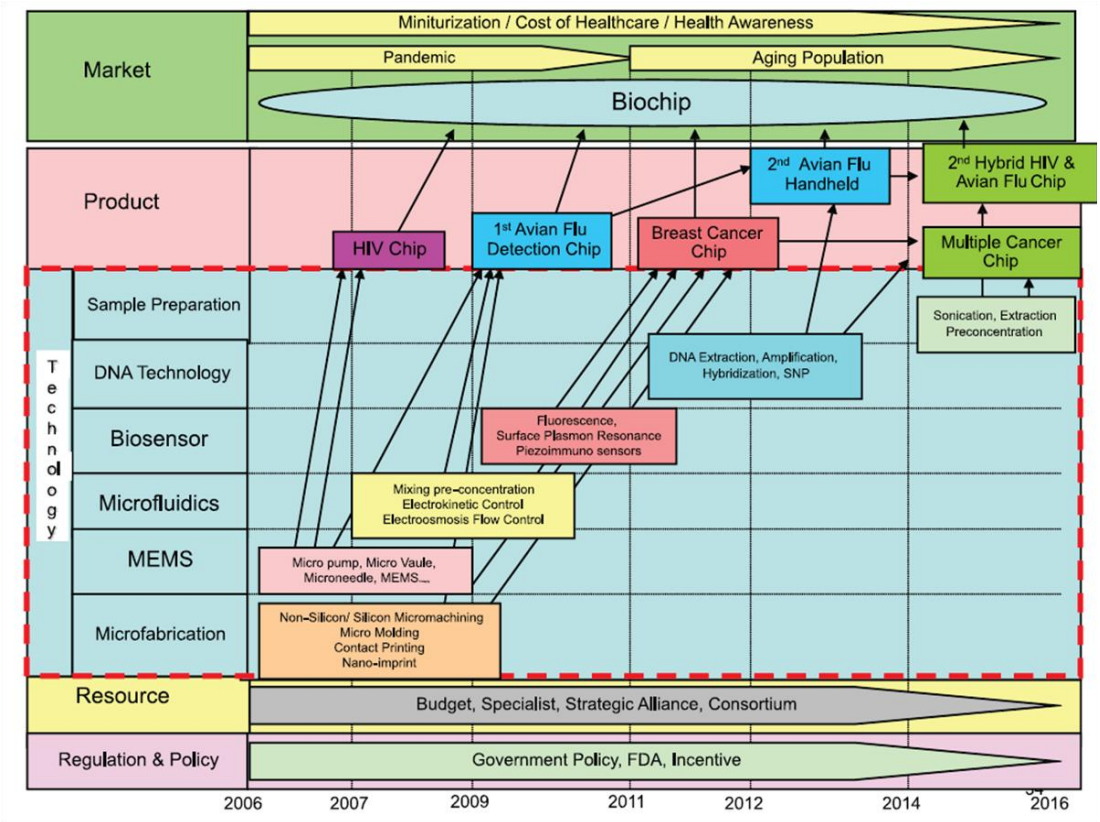

Fig. 1.1 Lab-on-a-chip product–technology roadmap, showing technology development to marketization of LOC products. This roadmap shows the tremendous progress the field of LOC has made over the past decade and its exciting potential going forward [4].

Since LOC was first proposed two and a half decades ago [5], many different ways of implementing LOC have been proposed. The most common platforms include channels and valves [6], emulsion-based droplets in channels [7, 8, 9], droplets over a two-dimensional surface [10, 11], and wells and traps where DNA, beads, or cells can be immobilized [12]. Optofluidics that integrates optics and microfluidics has spurred the development of many interesting technological advances, such as optofluidics microscopy, fluidic lens, and droplet/particle manipulation [13].

Our group has focused on the development of semiconductor-based optofluidic platforms for droplet and cell manipulation. The platforms, shown in Fig. 1.2(a)-(b), are named optoelectrowetting (OEW) and optoelectronic tweezers (OET), respectively. For OEW, light-induced electrowetting is able to move liquid droplets over the device surface reconfigurably. OEW is also known in literature as light-actuated digital microfluidics [14]. For OET, light-induced dielectrophoresis has the ability to manipulate a large number of particles/cells within its fluidic chamber.

Optoelectrowetting (OEW)

- Light-Induced Electrowetting
- pl to µl droplet Manipulation
- OEW force 100s µN/cm
- Speed 10s mm/s

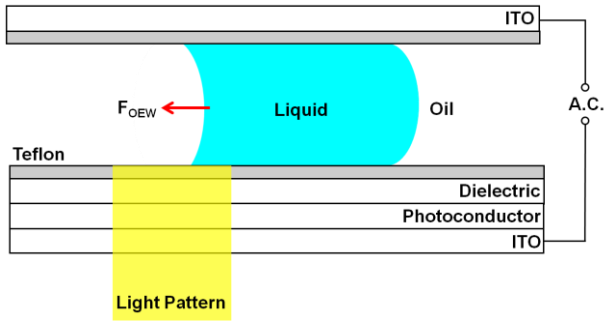

Fig. 1.2(a) Optoelectrowetting. Light defines the virtual electrode, which switches the AC voltage drop locally from the photoconductor layer to the dielectric layer. Capacitive energy in the dielectric layer imparts an electrowetting force on droplets, thereby moving them.

Optoelectronic Tweezers (OET)

- Light-Induced Diectrophoresis
- Microparticle/Cell Manipulation
- OET force 100s pN
- Speed 10s µm/s

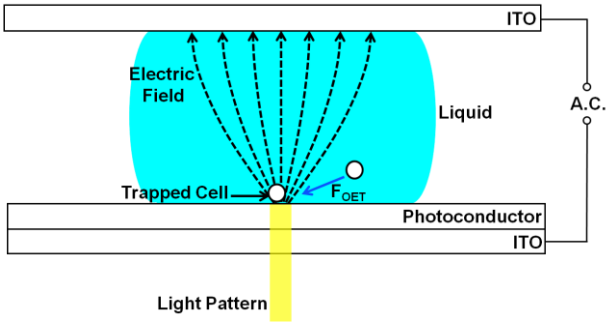

Fig. 1.2(b) Optoelectronic Tweezers. Light defines the virtual electrode, thereby switching the AC voltage drop locally from the photoconductor layer to the liquid layer. A non-uniform electric field in liquid layer imparts a dielectrophoretic force on cells, thereby trapping them.

For both devices, the common theme is the usage of light to pattern "virtual electrodes," thus eliminating the need for physically patterned electrodes to impart electrowetting or dielectrophoresis force. Therein lays the biggest strength of the optofluidic devices: the manipulation of droplets and particles using light can be highly reconfigurable, programmable, parallel, and indexed. This thesis will present recent progress made on both the OEW and OET platforms.

Chapter 2 describes the development of a novel OEW optimization model that can accurately predict the interaction of droplets, semiconductor layers, and a programmable Digital Light Processing (DLP)-based optical source. Chapter 3 describes the development of a single-sided OEW device utilizing surface metal ground mesh without the need for a top cover. Due to the optimization of the OEW device, shown in Chapter 4, it is now possible to manipulate parallel and arrayed droplets over a large operation area (cm × cm); critical droplet operations such as mixing, splitting, dispensing, and novel electrode designs will be demonstrated. In Chapter 5, work on a biological application using OEW will be demonstrated: droplet array based parallel, real-time, isothermal polymerase chain reaction (PCR) detection of Herpes Simplex Virus Type 1.

Switching gears to the OET device, efforts in long-term culture of adherent mammalian single cells into colonies in the OET platform is discussed in Chapter 6. The OET surface functionalization enables large (0.5-mm-diameter) growth patches where single cells can adhere and proliferate. Chapter 7 explains the link between the OEW and OET devices and how both droplets and particle manipulation within the droplets can be enabled on a unified platform. Chapter 8 concludes that the OEW and OET platforms are versatile LOC systems that are potentially applicable in a variety of biological applications.

Chapter 2 Optoelectrowetting (OEW) Principle, Design, and Optimization

2.1 Introduction

Droplet-based digital microfluidics offers new capabilities for chemical/biological assays. In this lab-on-a-chip (LOC) format, a large number of samples can be processed simultaneously. The small droplet volume greatly reduces the sample and reagent use, and increases the sensitivity of detection. There are two primary types of droplet-based microfluidics: (1) surfactant-stabilized water-in-oil emulsions that can be rapidly generated in microfluidic channels [8, 15, 16], but can only be addressed/processed sequentially; and (2) individually addressable digital microfluidic system such as electrowetting-on-dielectric (EWOD) devices [17, 18, 19, 20]. Here, each droplet can be independently addressed by voltage, making it possible to perform parallel manipulation of droplets. This chapter will focus on the second type of digital microfluidics.

Though several biological and chemical functions are now possible, including glucose assays [21], DNA amplification with polymerase chain reaction [22, 23], purification of peptides and proteins from heterogeneous mixtures [24], mammalian cell culturing [25] and chemical synthesis [26], the number of droplets that can be simultaneously processed in EWOD devices is limited by the number of electrodes in two-dimensional arrays. To eliminate the electrical interconnect bottleneck, we have previously proposed optoelectrowetting (OEW) devices that use projected light patterns to turn on "virtual electrodes" [27, 28]; the droplet follows the movement of light. This is made possible by using a photoconductor as light-sensitive electrodes. The initial OEW devices still have pixelated electrodes [28]. The subsequent devices used a featureless continuous film of photoconductors, thus decoupling the smallest droplet volume with electrode size [29]; droplet sizes as small as 10 pl have been demonstrated. However, these OEW devices require a focused laser beam to move the droplets, unlike the optoelectronic tweezers (OET) that can be powered by commercially available digital light projectors [30, 31]. Substantial reduction of the optical power density requirement (from 250 W/cm^2) is needed since the light intensity available from typical projects is around 1 W/cm^2. Though droplet manipulation using digital projector has been reported, the droplets were trapped in the dark gap between two illuminated areas in lateral devices at very high operating voltages [32].

A new challenge arises when using a projector to power OEW devices. Since projectors are designed for display, they produce light with multiple colors over the entire visible regime. The optical absorption coefficient in typical photoconductors - such as hydrogenated amorphous silicon (a-Si:H) - varies by as much as an order of magnitude from red to blue spectra. Blue light

is absorbed within 0.3 μm, while red light penetrates several micrometers; therefore, the distribution of photo-generated carriers is non-uniform. The previous model that treated the photoconductor as a lumped variable resistor completely breaks down. Color-based studies of optoelectronics tweezers device has been reported by Lin et al., [33] and Liang et al., [34], but their study is limited to optically induced dielectrophoresis with very different requirements. Hence, a detailed optimization study of the a-Si:H layer's switching ability with respect to the projector's color spectrum and power output would provide very useful insights into optimum device design in layer thicknesses and maximum droplet actuation force.

This chapter reports on the optoelectrowetting principle, design, and optimization. Most importantly, a distributed circuit model that takes into consideration color dependence and the non-uniform distribution of photo-generated carriers is presented. Using this model, we will derive the optimum thickness of photoconductors for given output spectra of selected projectors. This has resulted in 200× reduction in the optical power requirement and enabled us to design an optimized OEW device powered by projectors, as illustrated in Fig. 2.1. The digital projector will provide a programmable, versatile light source for different droplet operations. We will demonstrate movement and positioning of droplets with movement speed of 2 cm/s; more demonstrations of droplet functionalities and applications will be explored in Chapters 4 and 5.

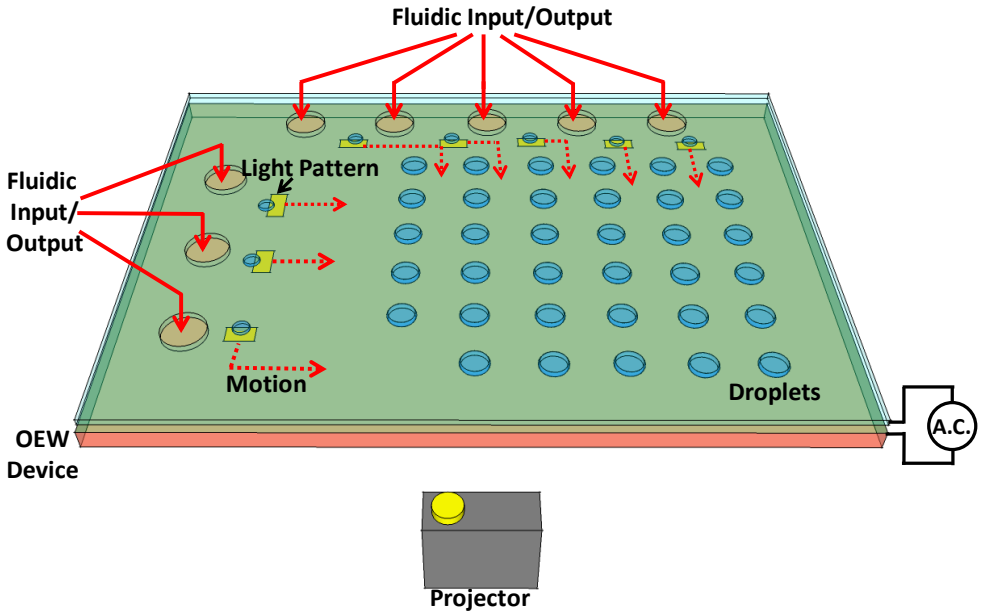

Fig. 2.1 Schematic of the light-actuated digital microfluidic device. The droplets are transported by projected light patterns from a digital light projector.

2.2 Optoelectrowetting Principles

We begin our discussion with electrowetting theory, followed by how electrowetting can be used to impart an actuation force that moves droplets. Finally, optoelectrowetting principles and basic device design will be presented.

2.2.1 Electrowetting Theory

Electrowetting is defined as the change in the contact angles of a liquid on a solid surface when different electrical potential is applied to the solid-liquid interface [35]. We begin our discussion from a free-standing liquid droplet in gas, as seen in Fig. 2.2(a). At the three-phase interface between a solid, a liquid and a gas, there exists liquid-solid interfacial tension γ_{ls}, solid-gas interfacial tension γ_{sg}, and liquid-gas interfacial tension γ_{lg}. The angle between liquid and solid interface is θ_0. The balance of these interfacial tensions in the *z*-direction follows Young's equation:

$$\gamma_{ls} = \gamma_{sg} - \gamma_{lg}\cos\theta_0 \tag{2.1}$$

As illustrated in Fig. 2.2(b), when an electrical potential V is applied to the liquid-solid interface, the potential will drop across the electric double layer at the liquid-solid interface, capacitance per unit area c (units: Farad/meter^2) is supplied, resulting in the reduction of γ_{ls} governed by the Liepmann equation:

$$\gamma_{ls}(V) = \gamma_{ls}(0) - \frac{1}{2}cV^2 \tag{2.2}$$

The balance of these interfacial tensions, shown in Fig. 2.2(b) in the *z*-direction, results in:

$$\gamma_{ls}(0) - \tfrac{1}{2}cV^2 = \gamma_{sg} - \gamma_{lg}\cos\theta_{EW} \tag{2.3}$$

Substituting Equation (2.3) into (2.1), we will arrive at the Young-Liepmann equation:

$$\cos\theta_{EW} = \cos\theta_0 + \frac{1}{2\gamma_{lg}}cV^2 \tag{2.4}$$

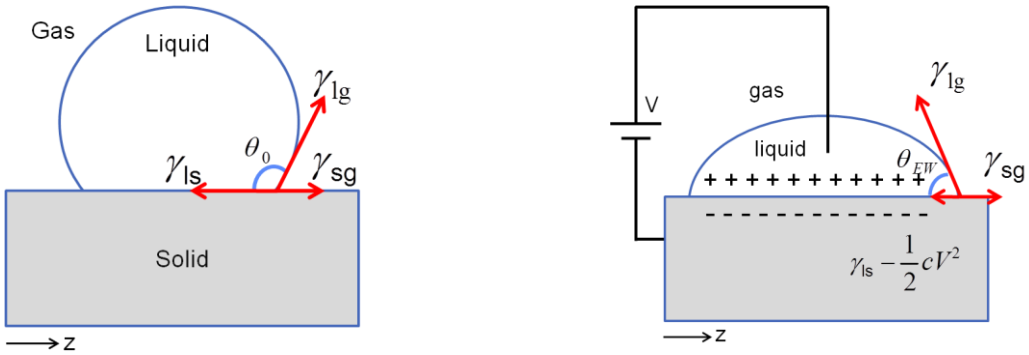

(a) **(b)**

Fig. 2.2 (a) A droplet on a hydrophobic surface where the balance of the three-phase surface tension vectors results in the contact angle and shape of the droplet; and (b) a droplet on a surface with voltage applied. The liquid–solid surface tension value is decreased by the capacitance per unit area, resulting in the reduction of contact angle.

2.2.2 Moving a Droplet with Electrowetting Force

Figure 2.3 shows a situation where voltage is applied to only half of a droplet. Specifically, one side of the droplet is at a non-electrowet angle of θ_0 [see Fig. 2.1(a)], and the other side of the droplet is at an electrowet angle of θ_{EW} [see Fig. 2.1(b)]. The droplet will experience a net force towards the direction (+*z* in Fig. 2.3) of the electrowet side.

The net force per unit length F can be derived from looking at interfacial tension γ_{lg} and θ_{EW} and θ_0 in the *z*-direction:

$$F = \gamma_{lg}\cos\theta_{EW} - \gamma_{lg}\cos\theta_0 \tag{2.5}$$

Alternatively, we can use γ_{ls} on a droplet that has been electro-wet on one side:

$$F = \gamma_{ls}(V) - \gamma_{ls}(0) \tag{2.6}$$

Now if we substitute Equation (2.5) into Equation (2.3), or substitute Equation (2.6) into (2.2), we can derive a net electrowetting force per unit length [35, 36]:

$$F = \frac{1}{2}cV^2 \tag{2.7}$$

where, again, c is the capacitance per unit area, and thus the net force per unit length F will have the units of Newton/meter.

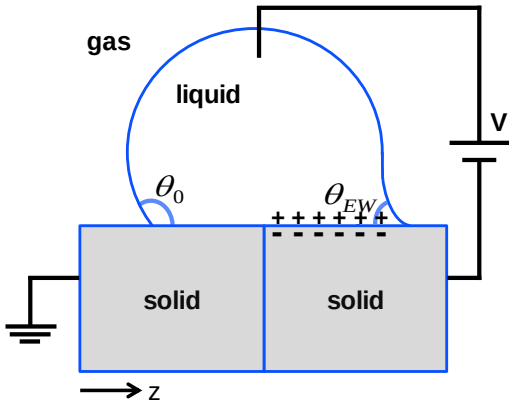

Fig. 2.3 Selective electrowetting of a droplet. The voltage is applied only to the right half of the droplet. The droplet will experience a net force towards the right half as governed by Equation (2.7).

2.2.3 Electrowetting-on-Dielectric Principle

Pioneered by R.B. Fair's group at Duke University [17] and C.J. Kim's group at UCLA [18], several key practical improvements have been made to manipulate droplets effectively over a device surface. A typical configuration is shown in Fig. 2.4. The manipulation of droplets now happens over a dielectric layer, which in turn is deposited over individually addressable electrodes. These electrowetting devices have been named Electrowetting-on-Dielectric (EWOD)

and Digital Microfluidics (DMF or DM). In this thesis, we will refer to this device configuration as EWOD.

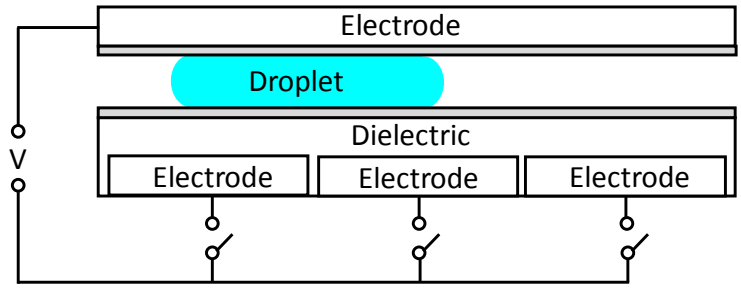

Fig. 2.4 A typical EWOD device consisting of a dielectric layer on top of individually addressable electrodes. By applying a voltage sequentially to the electrode array, an electrowetting force is imparted on the droplet, which then translates the droplets through the electrowetting force.

Several key improvements have enabled the EWOD device to be a viable platform for effective droplet actuation. The first improvement involves the addition of a dielectric layer between the conductive electrodes and the liquid. This is because only a small voltage can be sustained in the electric double layer before dielectric breakdown occurs. By using a dielectric layer, a much higher voltage can be applied for droplet actuation. Factoring in the dielectric layer, now Equation (2.7) can be simplified into [36]:

$$F = \frac{1}{2}\frac{\varepsilon_{di}\varepsilon_o}{t_{di}}V^2 \tag{2.8}$$

where ε_o is the permittivity of free space, ε_{di} is the relative permittivity of the dielectric layer, and t_{di} is the thickness of the dielectric layer.

The second improvement involves the use of a planar top electrode instead of a metallic pin. The top cover is typically made of electrically conductive indium-tin-oxide (ITO) covered glass. The ground electrode is always in contact with the droplet, no matter where the droplet moves to over the surface of the device.

The third improvement involves the use of electrode array, as shown in Fig. 2.4. A voltage can be applied sequentially to electrodes, which in turn induces the electrowetting force on one side of a droplet to transport them.

The fourth improvement involves the use of oil as a filler liquid. The oil serves two purposes: (1) it lubricates the droplet motion over the surface of the device, and (2) it prevents evaporation of liquid. When oil is used as a filler liquid for water droplets, the previously mentioned liquid-gas interfacial tension γ_{lg} becomes water-oil interfacial tension γ_{wo}. The oil-water interfacial tension can be calculated using Fowkes equation [37]. Alternatively, droplet actuation in air has been conducted [18] and has found specific applications such as protein sample preparation [24].

2.2.4 Optoelectrowetting Principle

The number of droplets that can be simultaneously addressed in EWOD is limited by the size of the electrode array. Optoelectrowetting replaces the electrode array with a photoconductor in which dynamic "virtual electrodes" can be instantly generated by projected optical images. The electrode size can be varied by changing the light patterns. It also eliminate the electrical interconnect bottleneck in large NxN electrode array.

Figure 2.5 illustrates the structure and operating principle of the device. The bottom part of the device consists of an electrically conductive indium-tin-oxide (ITO)-coated glass substrate, a photoconductive layer of hydrogenated amorphous silicon (a-Si:H), a dielectric layer of aluminum oxide (Al_2O_3), and a thin hydrophobic layer of Teflon AF. The top layer consists of an ITO- and Teflon-coated glass. The microfluidic droplet manipulation chamber is defined between the top and bottom substrates with a spacer. An AC voltage is applied between the top and bottom ITO layers.

In the absence of light, the applied AC voltage drops primarily across the highly resistive a-Si:H layer. Upon illumination, the conductivity of the a-Si:H increases by more than 10× [38]. This shifts the voltage drop to primarily across the dielectric layer. In other words, the a-Si:H layer acts as a photo-activated switch that turns on/off the voltage across the dielectric layer. Thus, the illuminated area is analogous to an electrically biased electrode, or a "virtual electrodes". If the virtual electrode is created only on one-half of the droplet, a net electrowetting force, governed by Equation (2.8), acts on the droplet and translates it towards the illuminated region.

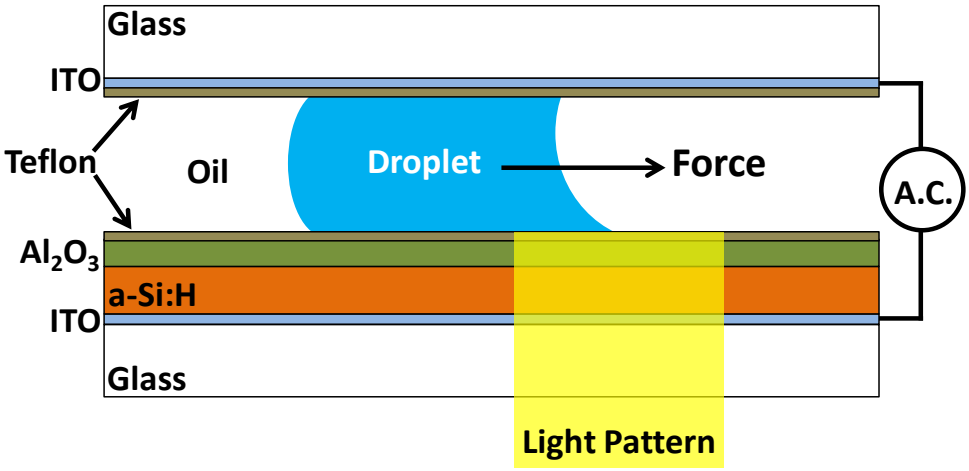

Fig. 2.5 Schematic of an OEW device showing incident light creating a localized area of high conductivity in the a-Si:H film. This switches the voltage drop from the a-Si:H layer to the oxide layer. A net electro-mechanical force then acts on the droplet, translating it towards the light pattern.

2.3 Optoelectrowetting Optimization Model

2.3.1 Dielectric Layer Thickness Optimization

The dielectric layer acts as a capacitor and has been studied extensively in the EWOD community [39]. The actuation voltage is inversely proportional to the areal capacitance of the dielectric layer. Therefore, the actuation voltage can be reduced by using a thinner insulator and/or an insulator with higher dielectric constant. Advances in atomic layer deposition (ALD), widely used by the semiconductor industry for high-K (high dielectric constant) dielectric deposition in state-of-the-art complementary metal-oxide-semiconductor (CMOS) transistors, have made it possible to deposit high-quality, conformal, pinhole-free layers of dielectric films on the devices [40, 41]. Hence, ALD is a good candidate for aggressively scaling down dielectric thickness to increase actuation force as governed by Equation (2.8). ALD Al_2O_3 was chosen for its high relative dielectric constant (~10), a high dielectric strength (~ 500 MV/m), and its ready availability in the fabrication laboratory. Table 2.1 shows a list of commonly used dielectric materials and their dielectric constants and dielectric strengths [42, 43].

However, there is a fundamental limit on how thin the dielectric layer can be; this is due to dielectric breakdown [39]. Fig. 2.6 shows the dielectric breakdown voltage as a function of the dielectric thickness, along with the voltages needed to achieve a range of forces on droplet. As expected, reduction of dielectric thickness results in lower actuation voltage needed to achieve a given force. However, because the breakdown voltage scales linearly while the electrowetting voltage scales with the square root of the dielectric thickness, there exists a minimum thicknesses (for example, 25 nm dielectric for 2500 μN/cm force) below which dielectric breakdown will occur before the electrowetting voltage. Dielectric breakdown results in irreversible damage to the dielectric layer and causes electrolysis in water droplets. ALD Al_2O_3 layer thickness of 100 nm was appears to be a reasonable choice to achieve high actuation force but not susceptible to dielectric breakdown. We will use this value for all subsequently calculations.

Table 2.1 List of commonly used dielectric materials and their dielectric properties

Material	Relative Dielectric Constant	Dielectric Strength (MV/m)
PTFE/Teflon AF	2	21
Cytop	2.1	110
PDMS	2.3–2.8	21.2
Polyimide	3.4	22
Parylene–C	3.15	268
Silicon Dioxide	3.9	400–600
Silicon Nitride	7	500
Aluminum Oxide	10	500
Hafnium Oxide	25	850

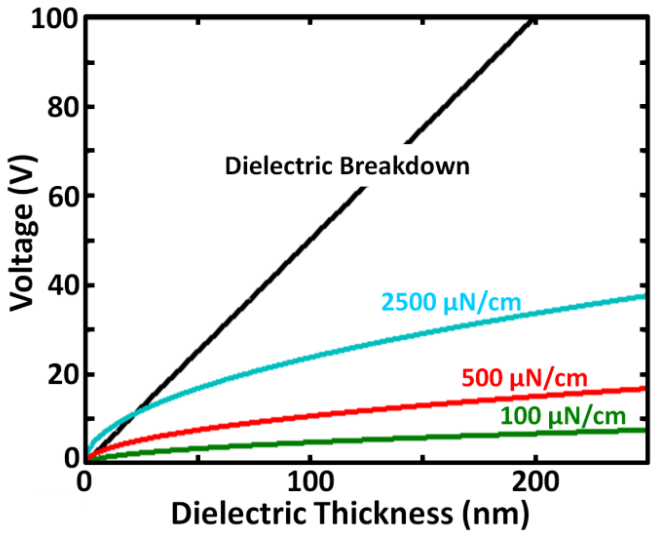

Fig. 2.6 Plot of voltage applied vs. dielectric thickness. Dielectric breakdown voltage for Alumina and voltage necessary to impart a certain amount of force per length is shown. Although thinner dielectric result in higher force, below a certain thickness dielectric breakdown will occurs before the necessary droplet actuation force can be reached. For example, to achieve 2500 µN/cm, dielectric layer cannot be thinner than 25 nm.

2.3.2 Photoconductive Layer Thickness Optimization

This section will focus on the optimum thickness of the photoconductive a-Si:H layer. When the a-Si:H layer is too thin, there is not enough impedance difference between "on" and "off" states. However, when the a-Si:H layer is too thick, a very high-intensity light source is needed to turn on the virtual electrode. This is the case in the previous demonstration [29], where a 250 W/cm^2 laser was used to switch a thick 5 µm a-Si:H layer. However, a typical data projector, produces ~1W/cm^2 of optical intensity over an area of 1 cm^2. Further complicating the matter, data projectors are programmed to output a spectrum of colors when projecting white light. Hence, a detailed study of the a-Si:H layer's response to the projector's output is needed.

The choice of a-Si:H for photoconductive layer material is two-fold. First, a-Si:H has a high absorption coefficient in the visible optical range. Its absorption coefficient is 10 to 100 times that of crystalline silicon [44]. Consequently, only a thin film (1 µm) is needed to absorb a majority of the visible spectrum. Second, large-scale fabrication of a-Si:H is well established in the solar cell industry. The infrastructure can easily be used for low cost production of OEW devices.

For efficient OEW actuation, the thickness of the photoconductor should be optimized. In previous analysis [29, 30], the photoconductor was modeled as a lumped variable resistor whose resistance changes with incident light intensity. In the physical device, however, the photogenerated carriers are not distributed uniformly in the photoconductor. They follow the distribution of the light intensity, which decays exponentially from the surface. The decay length is the inverse of the absorption coefficient, which is highly sensitive to the wavelength. The output of a digital projector covers the entire visible spectrum.

The output spectra and power density of the projector (Dell 4210X DLP) used in experiment reported herein is characterized in Fig. 2.7. Figure 2.7(a) shows the spectra when the projector is programmed to produce red, green, blue, and white colors. The spectra are measured with spectrometer Princeton Instruments SP2750. The power densities, measured by a thermopile at a distance of 7 cm from the projector, are 0.15, 0.25 and 0.27 W/cm^2 for red, green, and blue light, respectively. The power density of white light (1.38 W/cm^2) is about twice of the combined powers of red, green, and blue light due to the design of the color wheel and operation of the DLP chip.

The absorption coefficient of different light spectrums in the a-Si:H layer is measured using the experimental set-up shown in Fig. 2.7(b). Incident light is shone onto the a-Si:H film at an angle of 15°, light is absorbed in the a-Si:H film, and the transmitted light power and reflected light power were captured using a thermopile sensor. Power absorbed in the film can be calculated by subtracting the transmitted and reflected light power from the source light power.

The measured and reported [34, 45] absorption coefficient for hydrogenated amorphous silicon (a-Si:H) is shown in Fig. 2.7(c). The wavelength band is simplified to be 450 nm for blue, 550 nm for green, and 700 nm for red. The absorption coefficient varies by an order of magnitude across the visible spectrum: the absorption coefficient for blue wavelength, α_{blue}, is measured to be 15× higher than that for red wavelength, α_{red}. As confirmed qualitatively in Fig. 2.7(d), the red light penetrates deeper in a-Si:H than the blue light due to the lower attenuation constant.

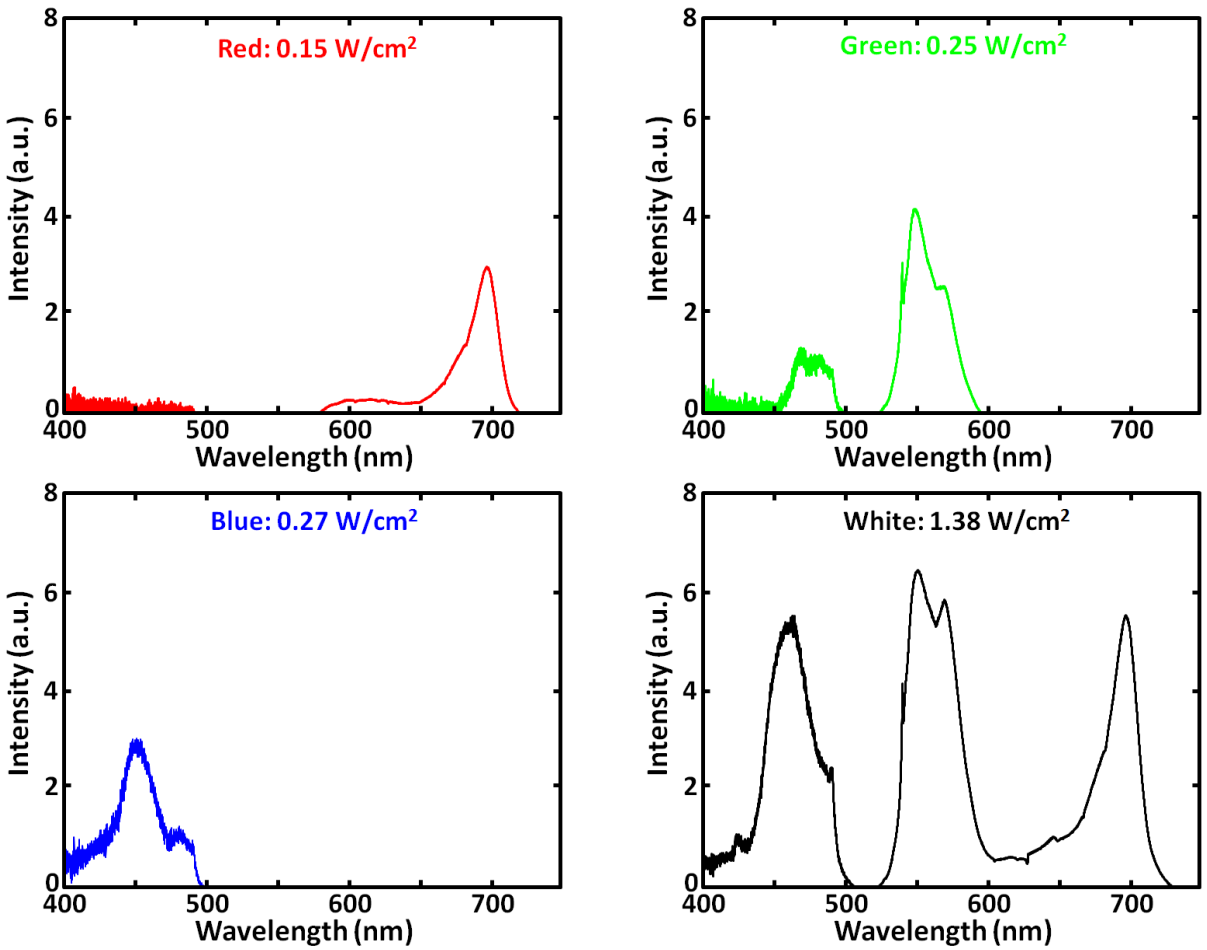

Fig. 2.7(a) The output spectra and power densities of the projector used in this experiment (Dell 4210X). White light output is 2× stronger than the combined red, green and blue light due to the design of the projector's color wheel.

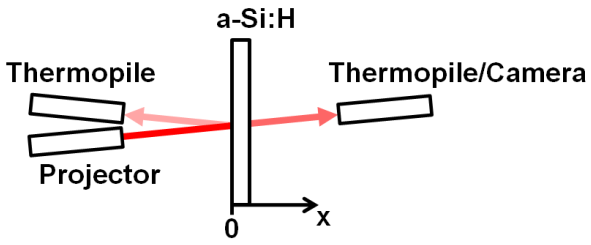

Fig. 2.7(b) Experimental set-up for measurement of absorption coefficient. Incident light from projector is absorbed in the a-Si:H film, transmitted and reflected light power captured using thermopile sensors.

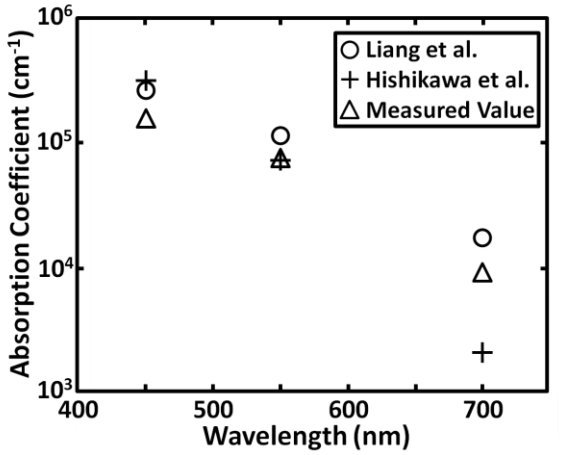

Fig. 2.7(c) Absorption coefficients of amorphous silicon measured at blue, green and red color. Data from literature is also plotted for comparison.

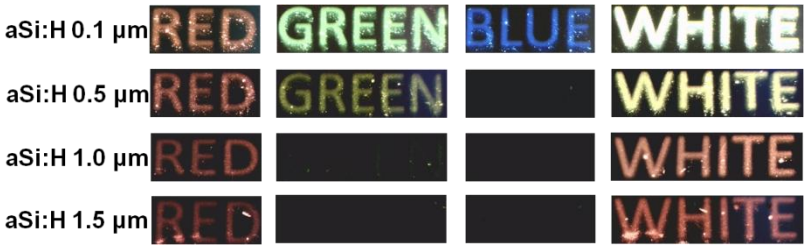

Fig. 2.7(d) Qualitative absorption of different colored light (red, green, blue, white) projection using a data projector through different thicknesses of a-Si:H.

Previously, the photoconductor was modeled as a parallel combination of a variable resistor, R_{ph}, and a capacitor, C_{ph} [see Fig. 2.8(a)]. Our distributed model is shown in Fig. 2.8(b). The photoconductor consists of many infinitesimal slices of thickness δx; each slice is modeled as a parallel combination of a resistor $R_{ph}(x) = \rho(x)\delta x$ and a capacitor $C_{ph}(x) = \epsilon_0\epsilon_{ph}/\delta x$, both are normalized to area. x is the distance from the surface of the photoconductor facing the projector, ρ(x) is the resistivity of the photoconductor, ϵ_0 is the free-space permittivity, and ϵ_{ph} is the relative dielectric constant of the photoconductor. The AC impedance of the slice per unit area is therefore:

$$Z_{\delta x}(x) = \frac{\rho(x)\delta x}{1+j\omega\varepsilon_{ph}\varepsilon_0\rho(x)} \tag{2.9}$$

where ω is the AC frequency. The light intensity decays exponentially inside the photoconductor due to absorption:

$$I(x) = I_0 e^{-\alpha x} \tag{2.10}$$

where α is the absorption coefficient of the photoconductor. The local distribution of the projected red, green, blue light at a certain depth *x* are plotted in Fig. 2.9(a) using the measured power

density and the measured blue (450 nm), green (550 nm), and red (700 nm) absorption coefficients shown in Fig. 2.7(c). The blue and green light are attenuated much faster than red light in a-Si:H. The intensity distribution of white light and "dark" output are also shown in the same plot. It should be mentioned that the projector still outputs a small amount of light even in the dark state (when the color of the projector is set to black).

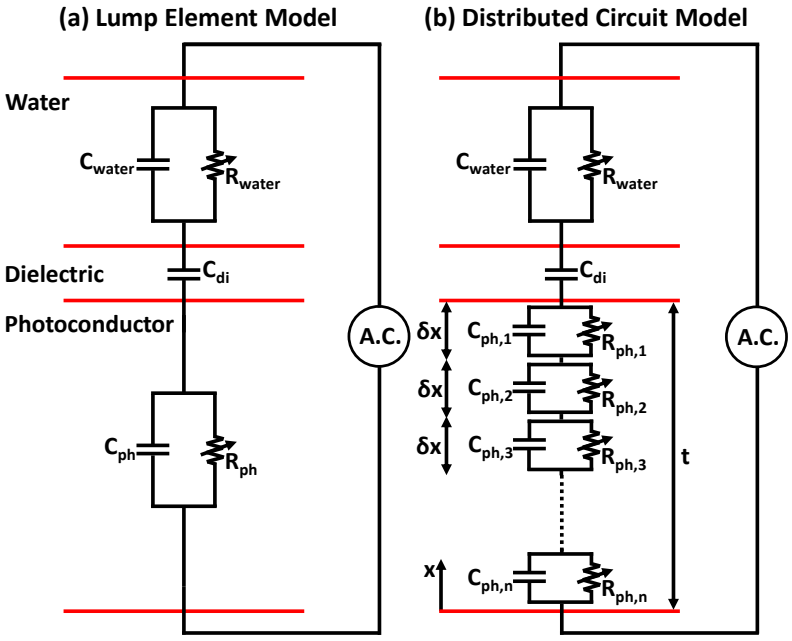

Fig. 2.8 (a) Lumped element equivalent circuit used to model previous OEW devices; and (b): the distributed circuit model proposed here to account for the color dependence and non-uniform distributions of photo-generated carriers.

The local electron and hole concentrations, $\delta n(x)$ and $\delta p(x)$, are related to the carrier generation rate $G_{\delta x}$:

$$G_{\delta x}(x) = \frac{I_0}{h\upsilon\delta x}\left(e^{-\alpha x} - e^{-\alpha(x+\delta x)}\right) \tag{2.11}$$

$$\delta n(x) = G_{\delta x}(x)\tau_n \tag{2.12}$$

$$\delta p(x) = G_{\delta x}(x)\tau_p \tag{2.13}$$

where h, υ, τ_n, and τ_p are Planck's constant, optical frequency, electron and hole lifetimes, respectively. For simplicity, we assumed 100% internal quantum efficiency and 100% optical transmittance at all interfaces.

The resistivity at location *x* is:

$$\rho(x) = \frac{1}{q\mu_n\delta n(x) + q\mu_p\delta p(x)} \tag{2.14}$$

where μ_n and μ_p are the electron and hole mobility, respectively. The local impedance at a certain depth *x*, normalized to the impedance of the dielectric layer, is shown in Fig. 2.9(b) for various color illuminations. Here, low impedance means the illuminated spot is turned on. Figure 2.9(b) clearly shows that blue and green lights are much more effective in turning on the photoconductor (i.e., reducing the total impedance), but only for thin photoconductors (d < 0.28 μm for blue light, and < 0.45 μm for green light).

The total impedance, $Z_{ph,total}$, for a photoconductor with thickness *t* can be calculated by integrating $Z_{\delta x}(x)$:

$$Z_{ph,total} = \int_0^t Z_{\delta x}(x)dx \tag{2.15}$$

The applied voltage is split between the ALD dielectric layer and the photoconductor. The impedance of the dielectric layer is:

$$Z_{di} = \frac{1}{j\omega C_{di}} \tag{2.16}$$

where C_{di} is the capacitance of the ALD layer per unit area. The voltage drop across the dielectric layer can be calculated using a voltage divider on the applied voltage V:

$$V_{di} = \frac{Z_{di}}{Z_{di}+Z_{ph,total}}V \tag{2.17}$$

Finally, because only the advancing half of a droplet is illuminated during droplet actuation, force imparted on a droplet is calculated to be the advancing side's force (light) minus off the unilluminated trailing side's force (dark). The actuation force per unit length of the contact line, F, can be calculated as [24]:

$$F = \frac{1}{2}\frac{\varepsilon_{di}\varepsilon_o}{t_{di}}\left(V_{di,light}^2 - V_{di,dark}^2\right) \tag{2.18}$$

where ε_{di} and t_{di} are the relative permittivity and thickness of the dielectric layer, respectively. $V_{di,light}$ and $V_{di,dark}$ are the voltage dropped across the dielectric layer, calculated using Equation (2.8), when the photoconductor is illuminated with and without light, respectively.

The droplet actuation force per unit length for a given thickness of a-Si:H is calculated for projected light with different colors for an OEW device with 100nm Al_2O_3 and an AC frequency of 10 kHz, using incident light intensity I_0 in Fig. 2.7(a). The calculated force as a function of photoconductor thickness *t* is plotted in Fig. 2.9(c). From the plot, it can be seen that a-Si:H thickness of 0.28 μm, 0.41 μm, and 0.8 μm imparts the most force on the droplet for blue, green, and red light, respectively. White light's force is significantly stronger due to its higher incident power.

To validate the new model, OEW devices with different a-Si:H thicknesses (0.1 μm, 0.5 μm, 1 μm, and 1.5 μm) were fabricated. The Al_2O_3 thickness is kept at 100 nm. Details of fabrication and methods are presented in Section 2.4.1. The maximum droplet actuation speeds are measured at an AC bias of 40 V_{ppk} and 10 kHz frequency. The microfluidic chamber height is

300 μm, and the conductivity of the liquid is 10 mS/m. The measured results shown in Fig. 2.9(d) are in good agreement with the theoretical model in Fig. 2.9(c). The ratio of the measured speeds under white light and single-color light actuation is higher than that predicted by the theoretical model. The difference might be due to the friction experienced by the droplet [46].

The distributed model enables optimization of the OEW device design and reduce optical power requirement by 200×. The power reduction allows the use of a commercially available data projector rather than a focused laser beam. Droplet speed of more than 1 cm/s is observed consistently in devices with 0.5 to 1 μm thick a-Si:H under white light illumination. Although the analysis is carried out with a specific light source and device parameters, changes can be easily incorporated for different light sources/devices.

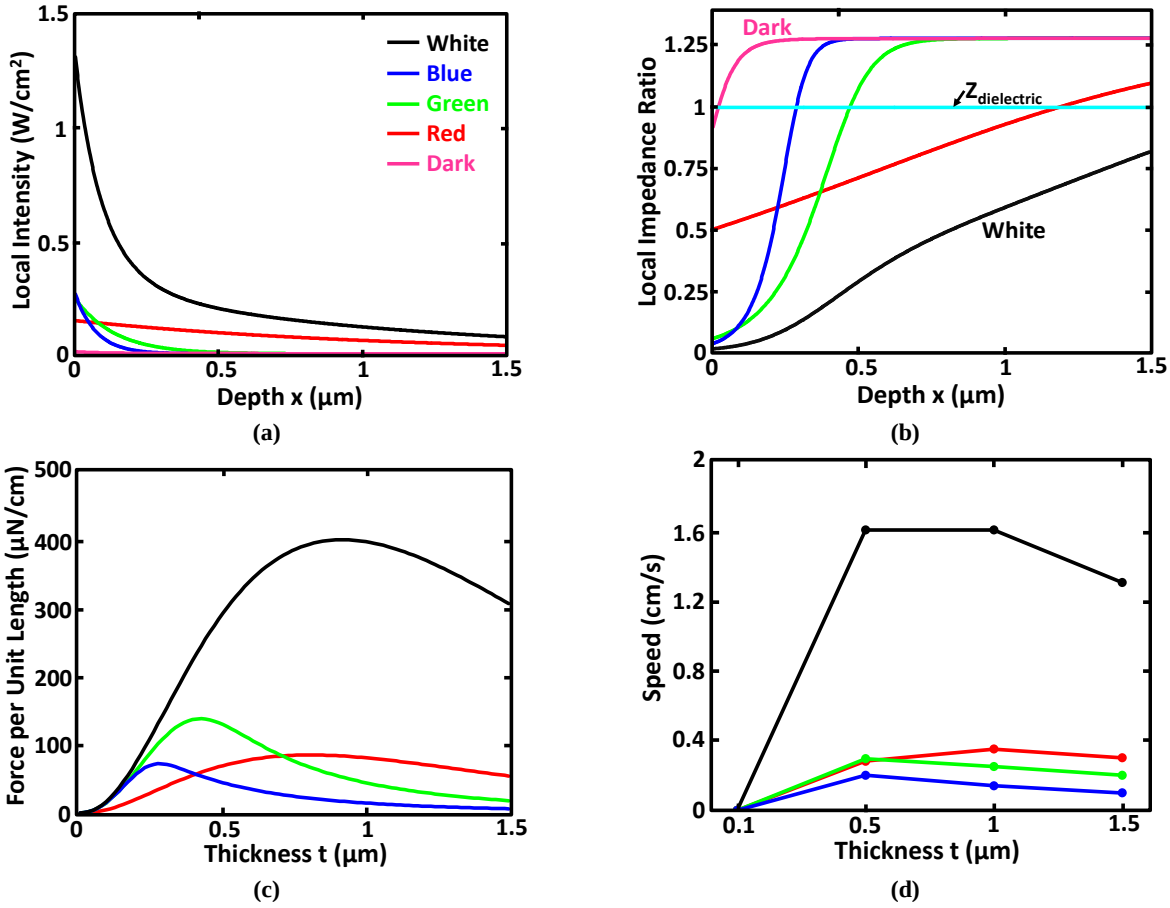

Fig. 2.9 (a) Optical intensity distribution in amorphous silicon photoconductor for various colors light from the projector. Blue and green is attenuated rapidly while red light penetrates more than 1.5 μm; and (b) local impedance versus distance from the illuminated surface for amorphous silicon under various colors light from the projector. The impedance is normalized to that of the dielectric layer; (c) the calculated force per unit length imparted on the droplet versus the thickness of a-Si:H for various colors of light from the projector (white, red, green, blue). The optimum thickness for white light is about 0.91 μm; and (d) the measured maximum velocity of the droplet versus the thickness of the amorphous silicon under various color light from the projector. The general trends agree well with the theoretical prediction.

2.4 OEW Droplet Speed and Frequency Verification

2.4.1 OEW Fabrication and methods

Fabrication of the OEW device begins with 300 nm ITO-coated glass substrates, followed by a photoconductive a-Si:H layer with various thicknesses (0.1, 0.5, 1.0, and 1.5 μm) deposited via plasma-enhanced chemical vapor deposition (PECVD) (Oxford Plasmalab 80plus). A 100 nm Al_2O_3 is then deposited by atomic layer deposition (ALD) (Picosun Sunale R150) and a 25 nm spin-coated (3000 rpm, 30s) 0.2% v/v Teflon AF film (Dupont, Wilmington, DE). The top electrode is made of another Teflon-coated ITO glass wafer. The fabrication process does not require any photolithography. The two substrates are bonded face-to-face with a spacer layer of double-sided tape (100-500 μm), forming a microfluidic chamber. The step-by-step fabrication protocol is presented in Appendix A.

During operation, an alternating current (AC) voltage is applied between the two ITO electrodes. A commercially available digital projector (Dell 4210X DLP) is used as a spatial light modulator for generating light patterns. The projected area is 1.6 cm × 1 cm, and the resulting pixel is 10 μm × 10 μm on the device. The liquid droplets can be actuated with one or multiple pixels at a time. Optical patterns are generated on a computer. Bright-field illumination, a continuous zoom microscope (Navitar 12X), and a CCD camera (Sony XCD-X710) are used for visualization and recording. No external optical lenses other than those from the projector and microscope are used. During operation, the fluidic chamber is first filled with silicone oil (1.0 cSt DMS Trimethylsiloxy-terminated Polydimethylsiloxane, Gelest Inc. Morrisville, PA). Aqueous droplets (10 mS/m deionized water with added KCl) are then introduced into the fluidic chamber via a syringe pump (KD Scientific, 780210) and Teflon tube (Cole-Parmer Microbore PTFE). The oil surrounding the aqueous droplets reduces the friction during movement as well as minimizes the evaporation of the droplets.

2.4.2 Droplet Speed Dependence on Voltage

In order to investigate droplet speed dependence on applied voltage, using the methods outlined in Section 2.4.1, OEW devices with a 1 μm-thick photoconductive a-Si:H layer and 100 nm ALD deposited Al_2O_3 were fabricated. White-light projector patterns and 1 μm a-Si:H photoconductive layer thickness was chosen as the combination for optimal droplet operation both theoretically and experimentally. Subsequent OEW devices operations described in Chapters 3-7 will all utilize this combination.

A square light pattern was projected onto the substrate near a 200 nl droplet. The microfluidic chamber height is 300 μm, and the conductivity of the liquid is 10 mS/m. The resulting maximum velocity was recorded for various applied voltages (see Fig. 2.10) at a frequency of 10 kHz. A maximum speed of 2 cm/s was achieved at 52 Vppk. Compared with prior work [29], the current device's manipulation speed is 20× higher. The droplet can be actuated with lower voltage bias, though at somewhat reduced speed (as per the quadratic dependence of actuation force on voltage [Equation (2.18)]. Voltages as low as 16 V_{ppk} have been used, which are amongst the lowest reported for digital microfluidics [39]. At high voltages, the actuation speed deviates from the quadratic relationship with respect to voltage as predicted by Equation (2.18) due to larger frictional forces acting on the droplet when speed increases [46].

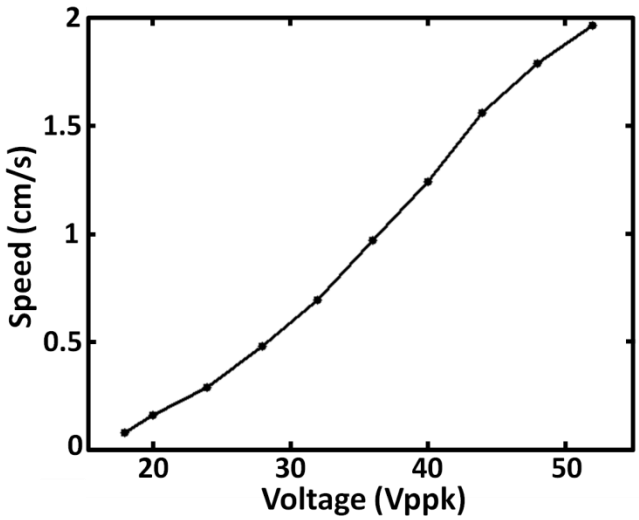

Fig. 2.10 The measured maximum speed of 200 nl droplets versus the voltage applied, for an OEW device with 300 µm height and biased at AC frequency of 10 kHz.

2.4.3 Droplet Motion Dependence on AC Frequency

An AC voltage bias is needed to transport droplets in the OEW device. This is because in the DC state, all voltage will drop across the dielectric layer (open circuit) even if photoconductivity is varied. To determine the best AC frequency, the same distributed circuit model was used to calculate the frequency response of the device, as shown in Fig. 2.11. The best response is observed at around 10 kHz. This agrees well with experimentally measured maximum speed of 190 nl droplets at an applied voltage of 40 V_{ppk}. The microfluidic chamber height is 300 µm, and the conductivity of the liquid is 10 mS/m.

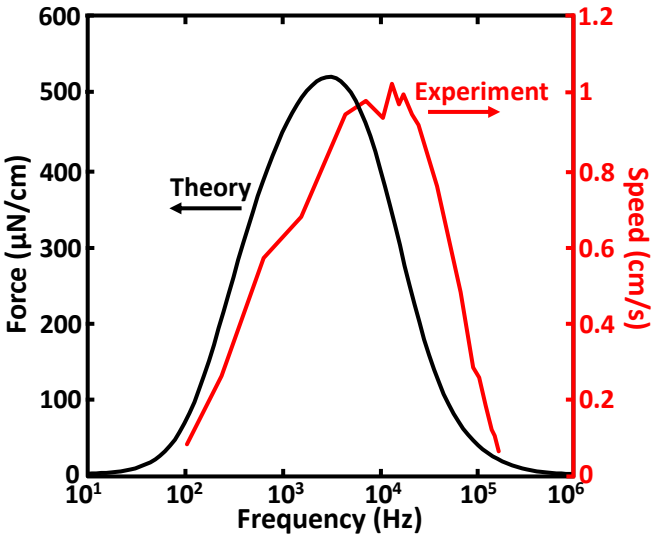

Fig. 2.11 The calculated force and the measured maximum speed of 190 nl droplets versus the frequency of the AC bias for an OEW device with 300µm height and biased at 40 V_{ppk}.

2.5 Conclusion

Chapter 2 has presented a distributed circuit model for light response of photoconductor in optoelectrowetting (OEW) device. This model correctly predicts the optimum thickness of photoconductor when used with a multi-color light source, such as a digital light projector. The optimized OEW device has 200× lower optical power requirement compared to previous devices. The ability to use digital light projector greatly reduces the cost and complexity of the optoelectrowetting system. Droplet speeds of > 1 cm/s are achieved consistently. This OEW platform offers many advantages over other droplet manipulation methods, including versatility and flexibility of the programmable microfluidic systems, and the simplicity and low cost of the consumables. More demonstrations of OEW droplet functionalities and applications will be explored in Chapters 4 and 5.

Chapter 3 Single-Sided Optoelectrowetting

3.1 Introduction

Droplet-based digital microfluidics has many applications ranging from sample preparation for sequencing to single cell genomics. Single-sided digital microfluidics (no top covers) provides many advantages over the conventional digital microfluidics configuration presented in Chapter 2. Specifically, the advantages are: (1) easy integration with microfluidic structures (e.g., PDMS); (2) more options for fluidic input/output (I/O) functionalities such as direct droplet extraction; (3) hanging droplets culture (such as those used in colony formation for stem cells [47]); and (4) droplet array transfer by contact printing.

Conventional electrowetting-on-dielectric (EWOD) [17, 18] devices have demonstrated efficient manipulation of droplets. Single-sided EWOD devices have been developed with a droplet's leading part positioned on bias electrodes and its trailing part on ground electrodes [48, 49]. However, the wiring of EWOD devices is limited by the number of electrodes, thus limiting the number of droplets manipulated. The optoelectrowetting (OEW) device [50] presented in Chapter 2 replaces the physical electrodes with light-patterned virtual electrodes, eliminating the issues of wiring bottleneck and complex addressing schemes. These OEW devices require electrically conductive top covers, which limit the versatility of the device, especially in packaging and fluidic I/O. Single-sided OEW devices have been reported using lateral electrodes, but this is at the expense of reduced electrowetting force [51] or increased actuation voltage [32].

This chapter describes a single-sided optoelectrowetting-based digital microfluidic device with integrated metal mesh ground replacing the conductive indium-tin-oxide (ITO) top covers. In this single-sided configuration (illustrated conceptually in Fig. 3.1), droplets are no longer confined between two plates, leaving the topside open for microfluidic integration or direct droplet extraction. Droplets in this format are often termed “sessile droplets.” This single-sided device enables two-dimensional motion of droplets over the device surface. Both square and circular motion paths have been demonstrated, with a maximum droplet speed of 2.8 cm/s. Grid electrodes on EWOD was proposed conceptually by Fair et al. [52], but to the best of our knowledge, no working device has been demonstrated.

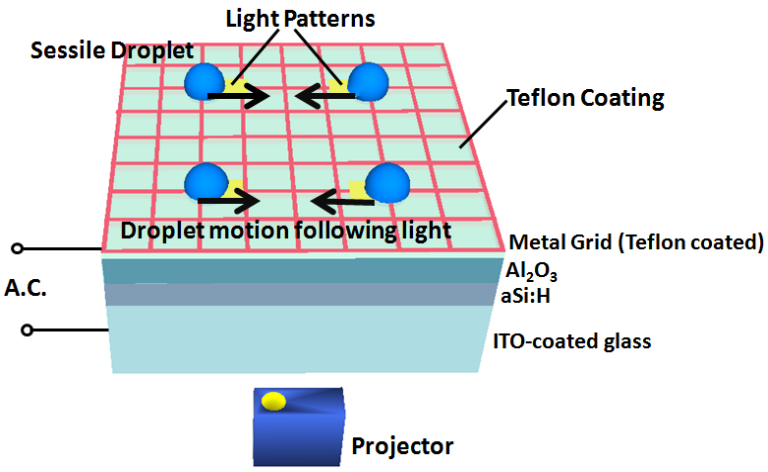

Fig. 3.1 Schematic of single-sided optoelectrowetting (OEW) device with integrated mesh ground electrode. The mesh ground is directly deposited on the surface of the dielectric layer, eliminating the need of top conductive electrode. A digital projector is used to project light patterns on OEW. Droplets will follow the projected light pattern through light-induced electrowetting.

3.2 Single-Sided OEW Design

3.2.1 Single-Sided OEW Principle

The single-sided OEW device design is shown in Fig. 3.2. The basic OEW structure is similar to the standard OEW device: a 1 μm hydrogenated amorphous silicon (a-Si:H) photoconductor is sandwiched between a 150 nm Al_2O_3 dielectric and an ITO bottom electrode. Instead of a conductive top cover as the ground electrode, a gold metal mesh (5 nm Ti, 25 nm Au) is directly evaporated on Al_2O_3 as the ground electrode and 25 nm Teflon is then spun onto the device surface. AC voltage is applied between the ITO and the meshed ground. The aqueous droplet is placed on top of the meshed ground, and a layer of oil is injected onto the device surface for lubrication and reduction of evaporation.

At the illuminated areas, the conductivity of the a-Si:H increases by more than 10×. This shifts the voltage drop to the dielectric layer, thus creating "virtual electrodes" on the device surface. If the virtual electrode is created on part of a droplet, a net optoelectrowetting force [Equation (2.18)] [36, 50] acts on the droplet and translates it towards the illuminated region. Comparing the single-sided OEW and the conventional OEW device discussed in Chapter 2, the main structural difference is that the ground electrode is now below the droplet.

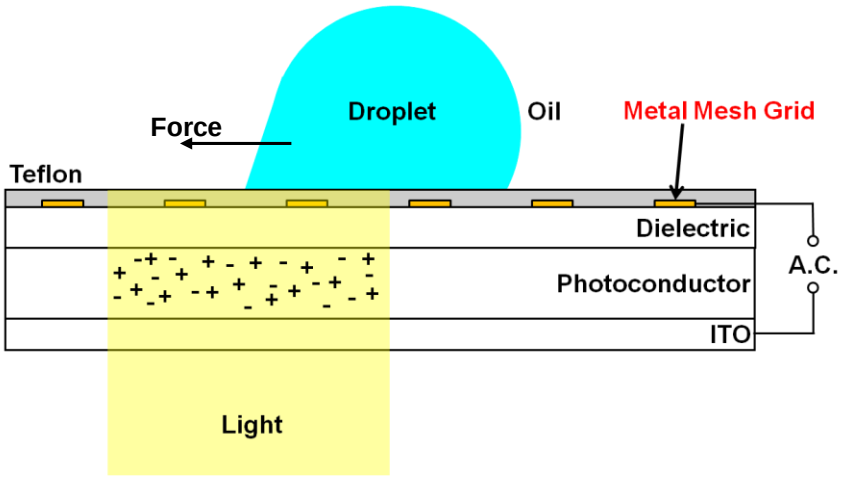

Fig. 3.2 Single-sided OEW device schematic and operation. Incident light creates electron-hole pairs within the photoconductor layer, therefore defining a localized area of high conductivity in the a-Si:H film; this switches the voltage drop locally, where the light shines, from the a-Si:H layer to the oxide layer. A net optoelectrowetting force then acts on the droplet at the illuminated area, moving it towards the light pattern. The ground electrode is now below the droplet.

3.2.2 Modeling and Design of Single-Sided OEW

A top view illustration of the metal mesh ground is shown in Fig. 3.3, where a Manhattan square grid of metal is deposited on top of the dielectric layer. Here, we define the metal line width as W and the pitch between metal lines as P. We then define the linear fill factor of the mesh ground as β, as a ratio between metal width and pitch (for example, β=1% for 10-μm-wide wire on 1 mm pitch):

$$\beta = \frac{W}{P} \tag{3.1}$$

The single-sided OEW devices can be modeled using an equivalent circuit shown in Fig. 3.4. The distributed circuit model for photoconductor layer used in Chapter 2 (Fig. 2.8(b)) is used again to model this photoconductor layer. The dielectric layer and hydrophobic layer are modeled as capacitors. A liquid droplet is modeled as a RC element, although its resistivity is relatively small and negligible. Contrary to the model shown in Fig. 2.8(b), where only one conductive path is possible in conventional OEW devices, two conductive paths now exist in the single-sided device due to the design of the surface metal grid. There is a new "shunting" path below the ground metal electrode. The shunting path, and its associated ground metal mesh area, reduces the effective voltage for electrowetting. We will use the circuit model to understand and reduce the shunting effect.

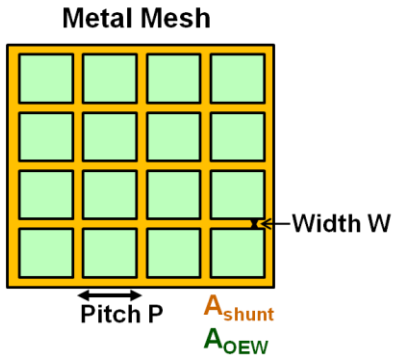

Fig. 3.3 A Manhattan square grid network of metal is deposited on top of the dielectric layer, where W is the metal line width, and P is the pitch. The linear fill factor of the mesh ground is defined as β = W/P.

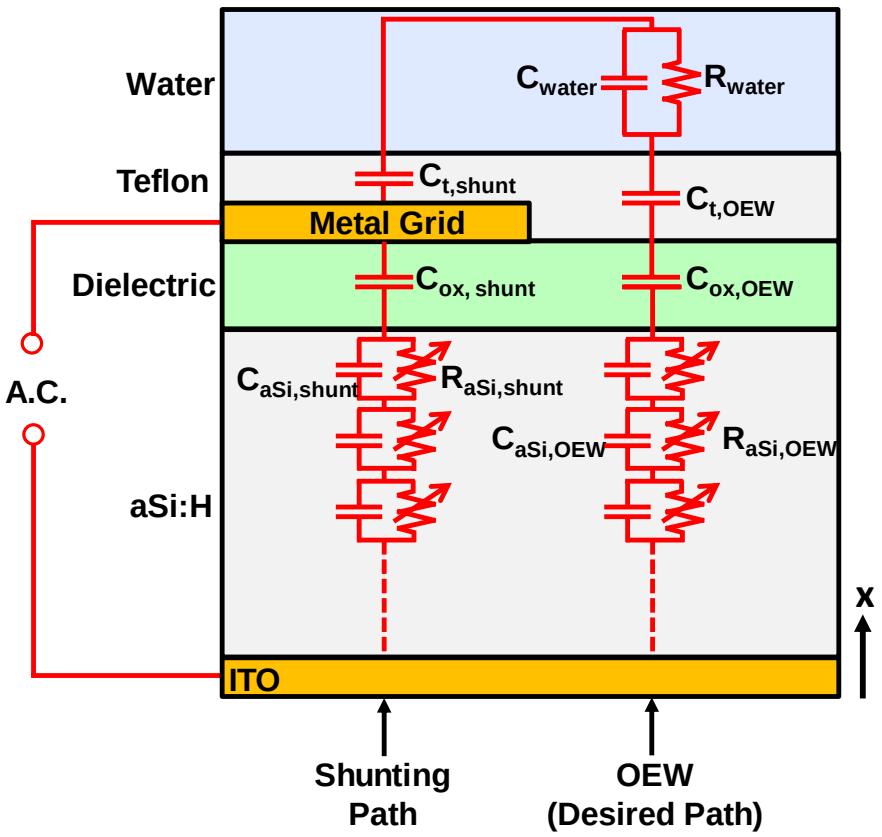

Fig. 3.4 Circuit model of single-sided OEW. Voltage dropped across the oxide layer results in droplet actuation. The shunting path reduces the effective voltage across the oxide. Hence, metal grid patterns should be kept as small as possible.

A larger metal surface electrode area will increase the electric field shielding effect. The useful OEW voltage, and consequently OEW force, reduces due to the ground metal mesh area, which in turn is related to fill factor β.

To derive the shunting effect of the single-sided OEW device for a certain P and W, we begin by calculating the shunting area A_{shunt}, which is the area below the metal mesh, and OEW area A_{OEW}, which is the useful area not covered by metal.

$$A_{shunt} = 2PW - W^2 \tag{3.2}$$

$$A_{OEW} = (P - W)^2 \tag{3.3}$$

The distributed circuit model for photoconductor layer shown in Section 2.3.2 is used again here. However, shunting and OEW areas needs to be taken into consideration. The a-Si:H photoconductor is modeled as a parallel combination of a variable resistor, R_{ph}, and a capacitor, C_{ph} [see Fig. 3.4]. The photoconductor in the distributed model consists of many infinitesimal slices of thickness δx; each slice is modeled as a parallel combination of a resistor $R_{ph}(x) = \rho(x)\delta x/A$ and a capacitor $C_{ph}(x) = \epsilon_0\epsilon_{ph}A/\delta x$, where A is the area of interest. x is the distance from the surface of the photoconductor facing the projector, ρ(x) is the resistivity of the photoconductor, ϵ_0 is the free-space permittivity, ϵ_{ph} is the relative dielectric constant of the photoconductor, and ω is the angular frequency. The AC impedance of the slice for the OEW area is therefore:

$$Z_{\delta x,OEW}(x) = \frac{\rho(x)\delta x}{A_{OEW}\left(1+j\omega\varepsilon_{ph}\varepsilon_0\rho(x)\right)} \tag{3.4}$$

Subsequent calculations of the local impedance change of photoconductor in response to photo-generated carriers are similar to the derivation presented in Section 2.3.2 [Equations (2.10)-(2.14)]. The total impedance for the OEW area, $Z_{ph,total,OEW}$, for a photoconductor with thickness t can be calculated by integrating $Z_{\delta x,OEW}(x)$:

$$Z_{ph,total,OEW} = \int_0^t Z_{\delta x,OEW}(x)dx \tag{3.5}$$

The AC impedance of the dielectric layers for the OEW path, $Z_{di,OEW}$, is:

$$Z_{di,OEW} = \frac{t_{di}}{j\omega\varepsilon_{di}\varepsilon_0 A_{OEW}} + \frac{t_{tef}}{j\omega\varepsilon_{tef}\varepsilon_0 A_{OEW}} + \frac{t_{tef}}{j\omega\varepsilon_{tef}\varepsilon_0 A_{shunt}} \tag{3.6}$$

where t_{di} and t_{tef} are thicknesses of the dielectric and Teflon layers, and ϵ_{di} and ϵ_{tef} are the relative dielectric constants of the dielectric and Teflon layers, respectively. The impedance of water is negligible.

The voltage drop across the dielectric layer in the OEW path, $V_{di,OEW}$, can be calculated using a voltage divider between the dielectric impedance and the impedance of the OEW path on the applied voltage V. In addition, Shunting areas A_{shunt} results in shielding effect and does not impart an electrowetting force. Therefore, A_{shunt} needs to be discounted accordingly. Thus, $V_{di,OEW}$ can be expressed as:

$$V_{di,OEW} = \frac{A_{OEW}}{A_{OEW} + A_{shunt}} \frac{Z_{di,OEW}}{Z_{di,OEW} + Z_{ph,total,OEW}} V \tag{3.7}$$

Finally, because only the advancing half of a droplet is illuminated during droplet actuation, force imparted on a droplet is calculated to be the advancing side's force (light) minus off the unilluminated trailing side's force (dark). The actuation force per unit length of the contact line on the single-sided OEW device, F_{SSOEW} (following Equations 2.8 and 2.18), can be calculated as:

$$F_{SSOEW} = \frac{1}{2} \frac{\varepsilon_{di}\varepsilon_o}{t_{di}} \left(V_{di,OEW,light}^2 - V_{di,OEW,dark}^2\right) \tag{3.8}$$

where $V_{di,OEW,light}$ and $V_{di,OEW,dark}$ are the voltage dropped across the dielectric layer, calculated from Equation (3.7), when the photoconductor is illuminated with and without light, respectively.

The single-sided OEW droplet actuation force per unit length, F_{SSOEW}, normalized to the standard OEW device with top ITO (calculated using Equation 2.18), is plotted in Fig 3.5. As shown in the plot, a fill factor below 1% will maintain droplet actuation above 95% relative to the conventional OEW device. For this calculation, a-Si:H thickness used is 1 μm, Al_2O_3 dielectric layer thickness is 150nm, AC frequency used is 10 kHz.

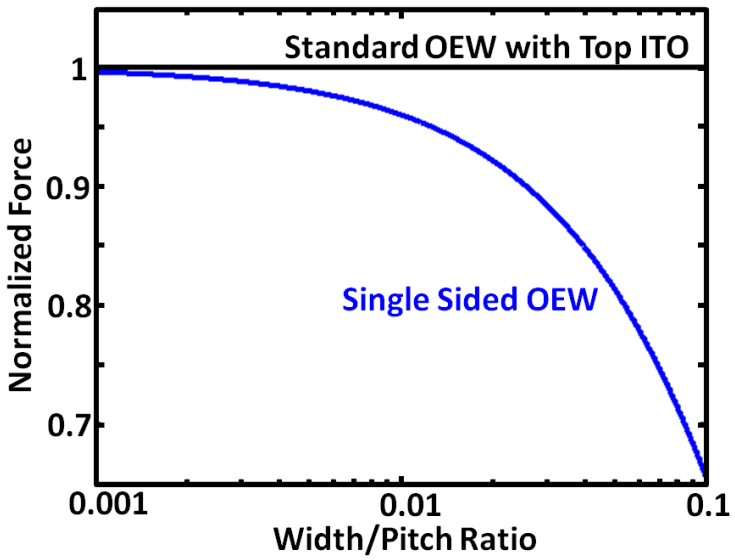

Fig. 3.5 Shunting effect on electrowetting force for single-sided OEW. Voltage and hence electrowetting force lost to shunting path can be minimized by keeping fill factor β small, making a small W and large P desirable.

Small fill factor requires narrow wire width, W, and large mesh pitch, P. The pitch is limited by the size of droplet. Since the droplet needs to overlap with the mesh ground, the droplet area presents an upper limit for the pitch. The minimum droplet size, S, is calculated assuming droplets form a hemisphere on the device surface (contact angle $\theta = 90°$):

$$S = \frac{1}{12}\pi(P - W)^3 \tag{3.9}$$

The relationship between width W, pitch P and smallest droplet volume is shown in Fig. 3.6. In this plot, β is fixed at 1% and the diameter of smallest droplet is equal to the pitch of the mesh. To maintain β of 1%, the wire width needs to be reduced to manipulate small droplets. For example, pico-liter droplets requires a mesh with W = 100 nm. In practice, the wire width is limited by lithography resolution and ultimately by the resistivity of the wires.

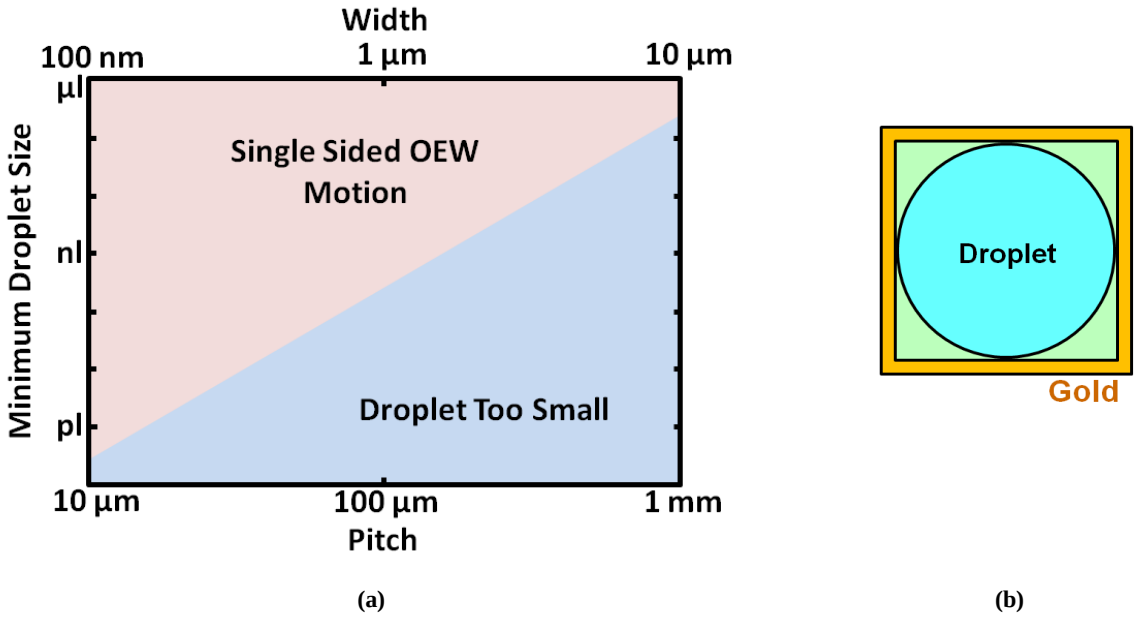

Fig. 3.6 (a) Minimum volume of the droplet as a function of the mesh pitch with β kept constant at 1%. Manipulation of pico-liter droplets will require a wire width of W = 100 nm. (b) schematic illustrating the minimum droplet size for a given mesh ground. A droplet is trapped if its diameter does not overlap with any part of the metal.

An additional consideration is the resistance of the metal wiring and its effect on electrowetting force. Since the ground metal mesh wiring designed is very thin (< 50 nm), it may have a large resistivity and a significant voltage drop, thus decreasing the electrowetting force. However, because of the metal wire grid network (Fig. 3.3), resistivity is decreased significantly compared to a single long wire. The resistance of a metal mesh grid is roughly equal to the resistivity of a single grid "segment", not the entire length of the wire [53]. Consequently, calculations with gold metal lines of 3 µm width, 25 nm height and 300 µm length equals ~100 Ω, which is orders of magnitude smaller than the resistance of the photoconductor layer and the dielectric layer. Hence, the metal grid conductivity issue is negligible.

3.3 Demonstration of Droplet Actuation

3.3.1 Single-Sided OEW Fabrication and methods

For single-sided OEW device, we used 300 nm ITO-coated glass substrates, followed by a 1 μm-thick-photoconductive a-Si:H layer deposited via plasma-enhanced chemical vapor deposition (PECVD) (Oxford Plasmalab 80plus), and then a 150 nm Al_2O_3 dielectric layer deposited by atomic layer deposition (ALD) (Picosun Sunale R150). A gold metal mesh (5 nm Ti, 25 nm Au) is evaporated on the Al_2O_3 layer as the ground electrode via a one-mask photolithography and lift-off process. The width W and the pitch P of the mesh are 3 μm and 300 μm, respectively. Finally, a 25 nm spin-coated (3000 rpm, 30s) 0.2% Teflon AF film (Dupont, Wilmington, DE) is coated on top of the device. The detailed fabrication process is presented in Appendix B.

During operation, an AC voltage is applied between the bottom ITO electrode and the metal mesh ground. A commercially available digital projector (Dell 4210X DLP) is used as spatial light modulator for generating light patterns. The projected area is 1.6 cm × 1 cm, and the resulting pixel is 10 μm × 10 μm on the device. The liquid droplets could be actuated with one or multiple pixels at a time. Optical patterns are generated on a computer. Bright-field illumination, a continuous zoom microscope (Navitar 12X), and a CCD camera (Sony XCD-X710) are used for visualization and recording. During operation, the surface of the device is first primed with a layer of silicone oil (7.0 cSt low volatility DMS Trimethylsiloxy-terminated Polydimethylsiloxane, Gelest Inc. Morrisville, PA). The oil surrounds the aqueous droplets and reduces friction during movement as well as minimizes the evaporation of the droplets. Aqueous droplets (10 mS/m deionized water with added KCl) are then introduced into the fluidic chamber via a syringe pump (KD Scientific, 780210) and Teflon tube (Cole-Parmer Microbore PTFE).

3.3.2 Droplet Motion Demonstration and Speed Measurement

We have experimentally demonstrated the operation of single-sided OEW devices with mesh grounds. A single 1 μl droplet was injected onto the device. A square white-light pattern was projected onto the substrate near the droplet and was able to transport the droplet around the device surface at 0.33 cm/s by moving the light pattern (Fig. 3.7). For maximum speed, a similar 1 μl water droplet was translated as fast as possible at a bias of 40 V_{ppk} and 10 kHz. The maximum velocity was measured at 2.8 cm/s, which is faster compared to speeds obtained using conventional OEW devices with top covers. It is hypothesized that this increase is speed is due to the elimination of the friction from the top cover [46].

Droplets are free to move in any arbitrary direction as long as the droplets maintain electrical contact with the meshed ground. Figure 3.8(a) and (b) show four 1 μl water droplets motion along a square path and circular path, respectively, (AC bias of 40 V_{ppk} at 10 kHz). For the droplets, the second meniscus on top of the contact line is due to water droplet contact with oil film.

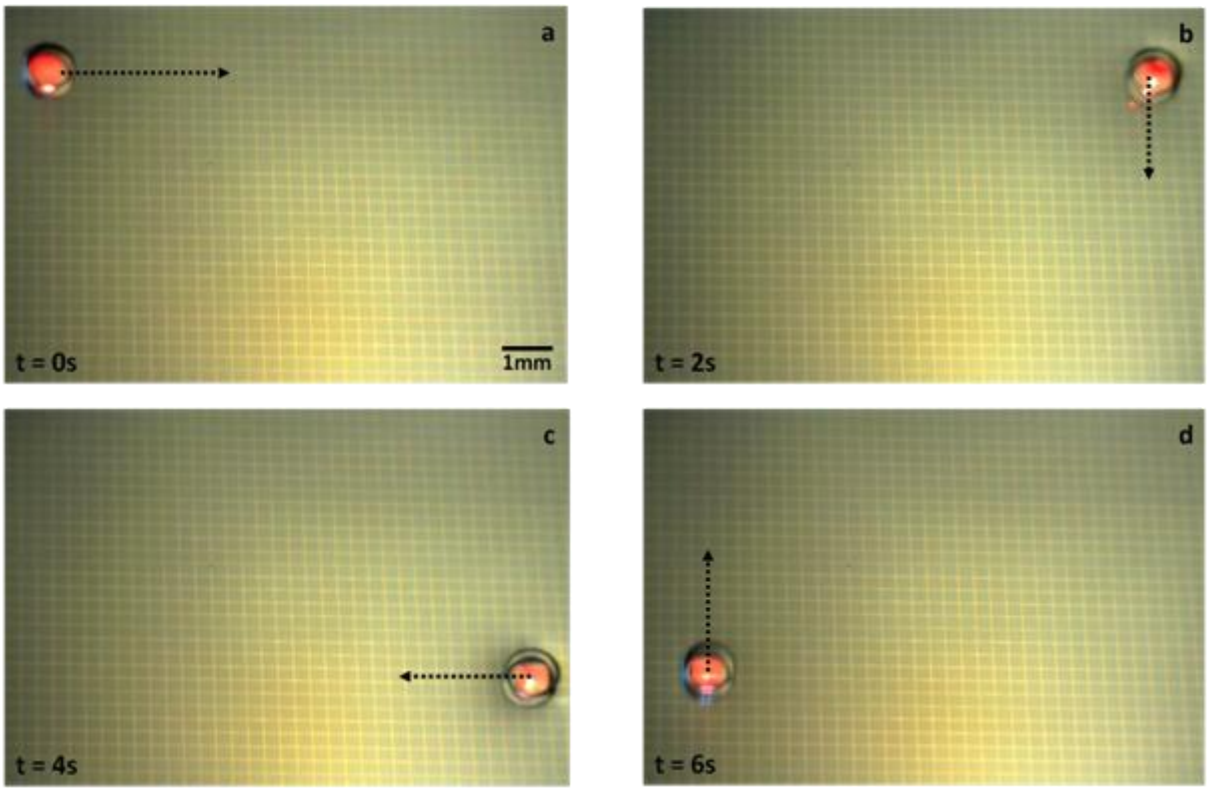

Fig. 3.7 Droplet actuation on single-sided OEW. A 1 µl droplet was injected onto the device. A light pattern was able to translate the droplet at 0.33 cm/s across the device surface (10 mS/m, 40 V_{ppk} at 10 kHz, W = 3µm, P = 300 µm).

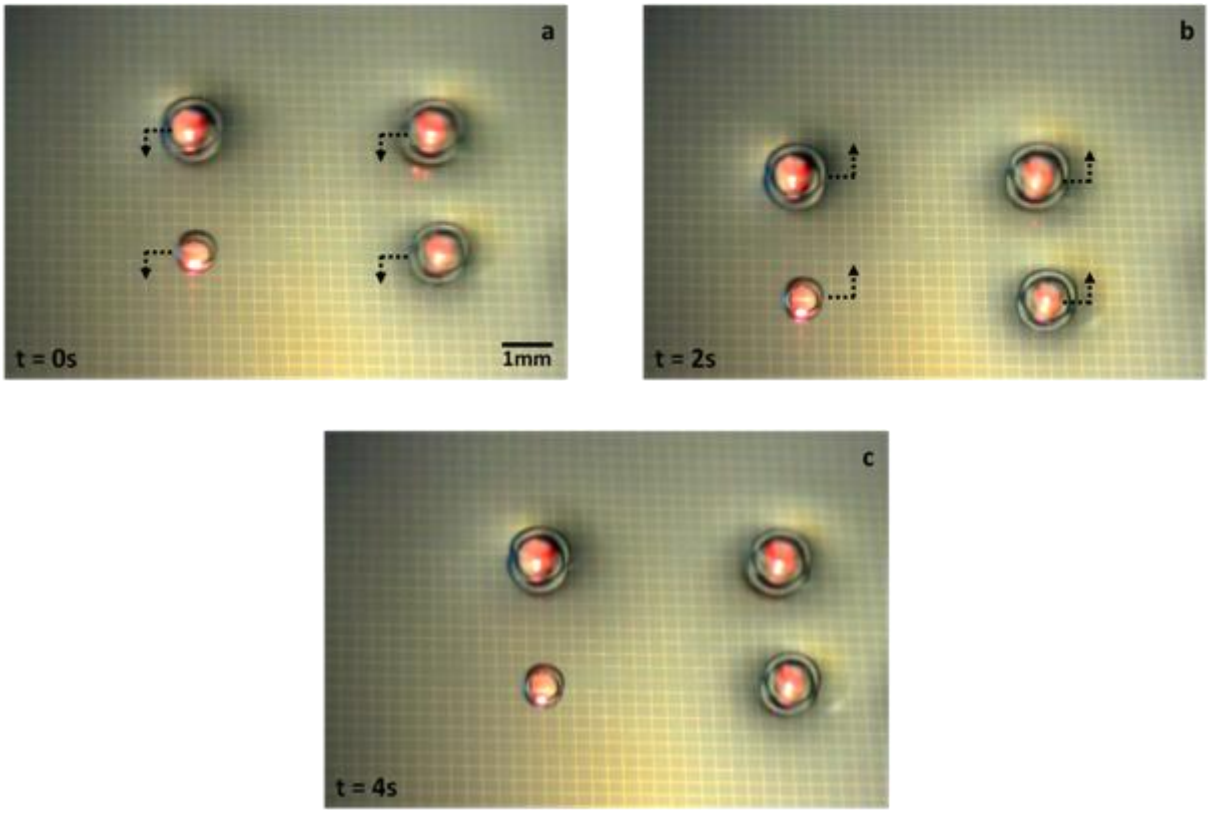

Fig. 3.8 (a) Array motion of droplets in square paths. Four 1 µl water droplets were injected onto the device surface and moved by light patterns in square paths (10 mS/m, 40 V_{ppk} at 10 kHz, W = 3µm, P = 300 µm).

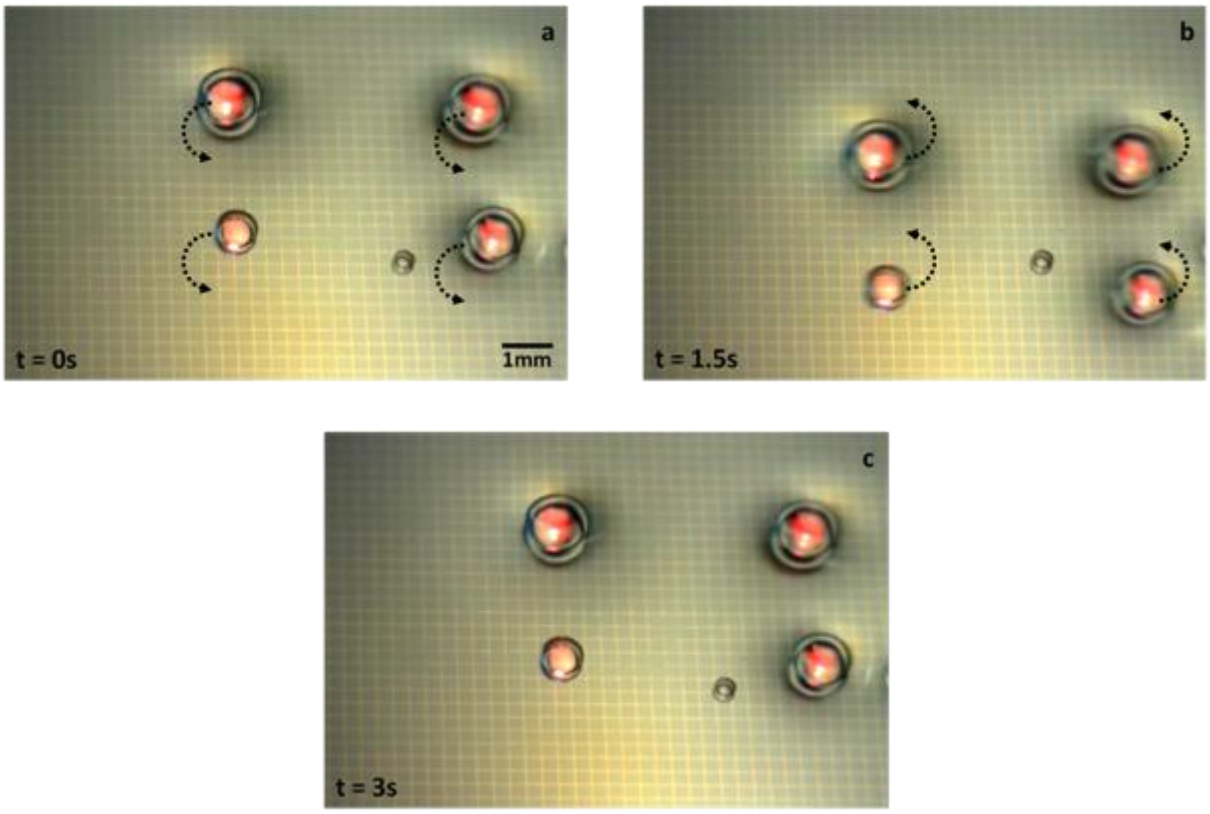

Fig. 3.8 (b) Array motion of droplets in circular paths. Four 1 µl water droplets were injected onto the device surface and moved by light patterns in circular paths (10 mS/m, 40 V_{ppk} at 10 kHz, W = 3µm, P = 300 µm).

3.4 Conclusion

In conclusion, we have demonstrated the efficacy of a new single-sided optoelectrowetting device with metal meshed ground directly deposited on the device surface. The surface metal mesh fill factor will directly affect droplet actuation force and minimum droplet volume. High-speed movements (2.8 cm/s) and parallel motion of droplets were successfully demonstrated on OEW device with integrated meshed ground comprising 3 µm wide wires on 300 µm pitch. This new structure makes it easier to integrate OEW with microfluidic devices (e.g., PDMS channels/chambers) and offers an exciting paradigm for many biological applications.

Chapter 4 Optoelectrowetting Droplet Functionalities

4.1 Introduction

For a droplet-based lab-on-a-chip (LOC) system to be truly useful in biological or chemical analysis, fluidic operations need to be seamlessly conducted. As previously demonstrated, the optoelectrowetting (OEW) device by Chiou et al. was proof-of-concept [29], where only the movement of droplets was shown. In Chapter 2, we optimized the OEW device such that a digital light projector could be used to manipulate droplets on the device surface. The projector enables easy, reconfigurable, and programmable creation of light patterns on the device surface to manipulate droplets. Hence, all desired fluidics operation functionalities could be realized.

This chapter will demonstrate that the OEW device is versatile and well suited to miniaturize and automate biological or chemical analysis currently performed using well plates and pipettes. This will greatly reduce the amount of reagent used as well as the reaction time. We will begin our demonstration with basic functionalities, such as droplet dispensing, parallel motion, arraying, splitting and merging, and different sized droplet motion. We then elaborate on the following: (1) droplet mixing and a novel rolling mixing motion path for enhanced mixing speed; (2) a novel crescent-shaped electrodes for reduction of heating within droplets; and (3) an on-chip Teflon blade for accurate splitting of droplets.

4.2 Demonstration of Basic Functionalities

4.2.1 OEW Device Fabrication and Methods

All OEW devices described in this chapter have top covers. Please refer to Section 2.2.4 for OEW device operation, Section 2.4.1 for OEW device fabrication and methods, and Appendix A for detailed fabrication method. All devices described in this chapter are fabricated with 1-μm-thick photoconductive a-Si:H layer and 100 nm ALD Al_2O_3 dielectric layer. Water used is 10 mS/m deionized water with added KCl.

4.2.2 Droplet Dispensing from Reservoir

The ability to create droplets from on-chip reservoirs is important for LOC applications. The reservoirs here are defined optically. Their areas are usually much larger than individual droplets. Figure 4.1 shows three snapshots of a video clip demonstrating the droplet generation process. 120 nl droplets are generated at a rate of 0.18 droplet/sec using a moving light pattern with an area of 1 mm × 1 mm.

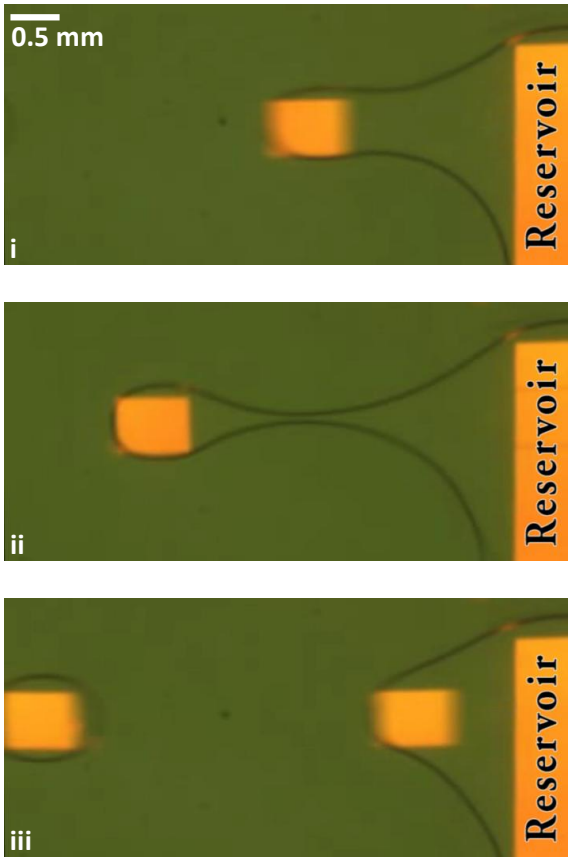

Fig. 4.1 Snap shots of a video clip showing dispensing 120 nl droplets from an optically defined reservoir. One droplet is generated every 5.5 seconds. The OEW device is biased with 60 V_{ppk} at 10kHz. Fluidic chamber height = 300 µm.

4.2.3 Parallel Droplet Motion

Figure 4.2 demonstrates that OEW is well positioned to effect real-time, reconfigurable droplet manipulation. The simultaneous movement of seven droplets is demonstrated. The four outer droplets move clockwise in a circular manner, while the three inner droplets move anti-clockwise.

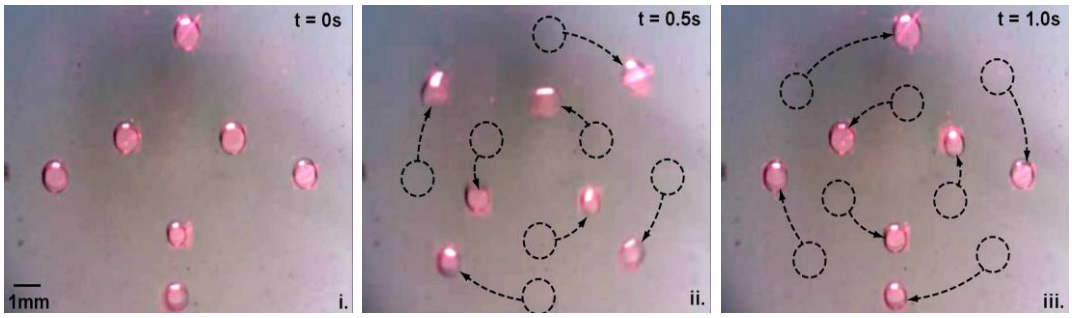

Fig. 4.2 Parallel movement of droplets. Seven droplets undergo simultaneous movement. Four outer droplets move clockwise in a circular manner, while three inner droplets move anti-clockwise in a circular manner (50 Vppk, 10 kHz). Fluidic chamber height = 300 µm.

4.2.4 Droplet Splitting and Merging

The ability to separate and merge droplets is a critical component of any digital microfluidic system because chemical reactions require reagents to be added or separately analyzed. In Fig. 4.3(a), two light patterns move two individual 900 nl droplets towards each other until they merge into one large droplet (1800 nl). Figure 4.3(b) demonstrates the splitting of an 1800 nl droplet into two 900 nl droplets; this is achieved by moving two light patterns in opposite directions.

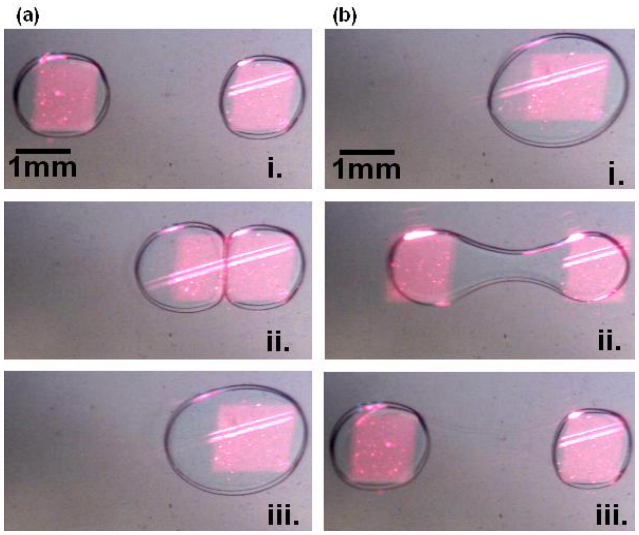

Fig. 4.3 (a) Droplet merging. Two 900 nl droplets (i) are merged (ii) by moving one light pattern towards the other resulting in a single droplet (iii) (50 Vppk, 10 kHz); and (b) droplet splitting; a single 1800 nl droplet (i) is pulled apart using two light patterns, with one pattern moving towards the left (ii), resulting in two distinct droplets (iii) (50 Vppk, 10 kHz). Fluidic chamber height = 300 µm.

4.2.5 Droplet Array Formation

High-density array of droplets enables high throughput multiplexed assays. Figure 4.4 demonstrates the device's ability to form 96-droplet (8 × 12) array. Light patterns extract 220 nl droplets dispensed from a Teflon tube and arrange the droplets in rows of 12 before transporting them into a rectangular array; the positioning of the array mimics a 96 well plate.

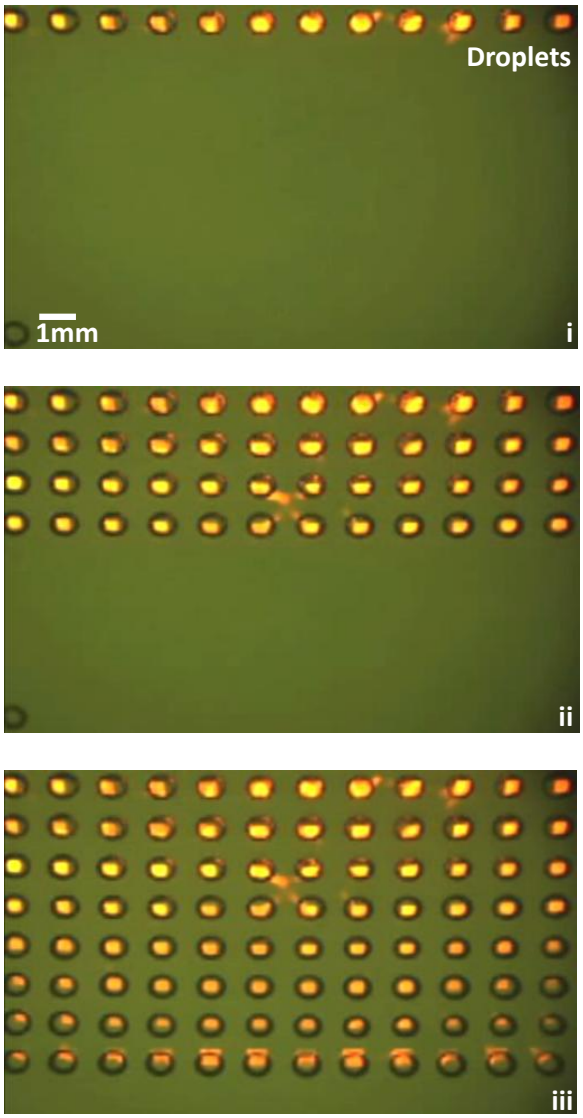

Fig. 4.4 Snapshots of a video clip showing the formation of 96 (8 × 12) droplet array by OEW actuation. The 220 nl droplets are dispensed by a syringe pump and a Teflon tube. The OEW device is biased with 60 V_{ppk} at 10 kHz. Fluidic chamber height = 300 µm.

4.2.6 Different Sized Droplet Motion

Manipulation of droplets with different volume is not easily achieved using EWOD devices because of the fixed electrode size. The OEW addresses this issue easily by simply changing the size, shape, and number of the optical patterns to define different virtual electrodes. Droplets with a wide range of volumes can be manipulated on the same chip, which enables applications where droplet size changes over the course of the application (e.g. addition of reagents during chemical/biological processing). As demonstrated in Fig. 4.5, two droplets of 3.3 µl and 190 nl (17× volume difference) are manipulated simultaneously on the same chip device surface.

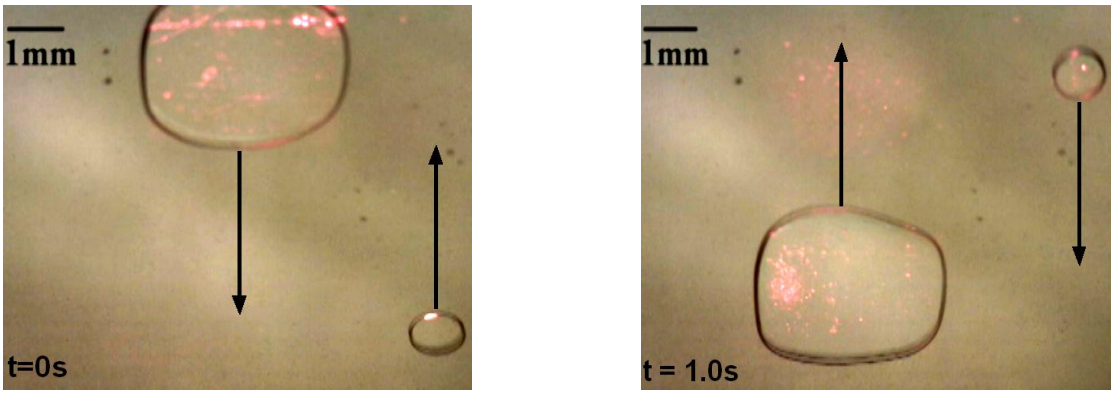

Fig. 4.5 Manipulation of bigger (3.3 µl) and smaller (190 nl) droplets on the same device surface; the volume differs by ~17× (40 Vppk, 10kHz, fluidic chamber height = 300 µm).

4.3 Rapid Droplet Mixing

4.3.1 Introduction

Rapid mixing of analytes and reagents in microfluidic devices is important for virtually all biochemical analysis. Mixing in microfluidics, however, is very slow due to laminar flow and low Reynolds numbers [54]. The EWOD-based digital microfluidics enables rapid mixing by rolling the droplets to increase the interfacial area, allowing much faster diffusion between reagents [55, 56, 57]. This section explores different ways of achieving mixing on the OEW device, including low-frequency pulsing of droplets, electro-thermal heating of droplets, and rolling mixing over the device surface. Here, we use the mixing time as a metric for comparing different mixing methods.

4.3.2 Diffusion

Reynolds number Re for an OEW droplet can be calculated as:

$$\mathrm{Re} = \frac{\rho U L}{\eta} \tag{4.1}$$

where ρ is the density of liquid (water = 1000 kg/m^3), U is the speed of droplet (1 cm/s), L is the characteristic linear dimension (1 mm), and η is the dynamic viscosity of liquid (water = 10^{-3}

kg/ms). Using these characteristic values, the Reynolds number for an OEW droplet is 10. Although this value is relatively large compared to channel-based microfluidic systems, mixing solely by diffusion would be very time consuming.

Fig. 4.6 illustrates the process we used to measure the diffusion time when two droplets mix. A water droplet (200 nl) is brought in contact with another smaller water droplet (50 nl) loaded with blue colored food dye at t=0. The diffusion process began and it was noted that the diffusion process from one end of the droplet to another end (1.8 mm) took around five minutes. Ideally, the mixing time for on-chip mixing should be on the order of seconds, not minutes.

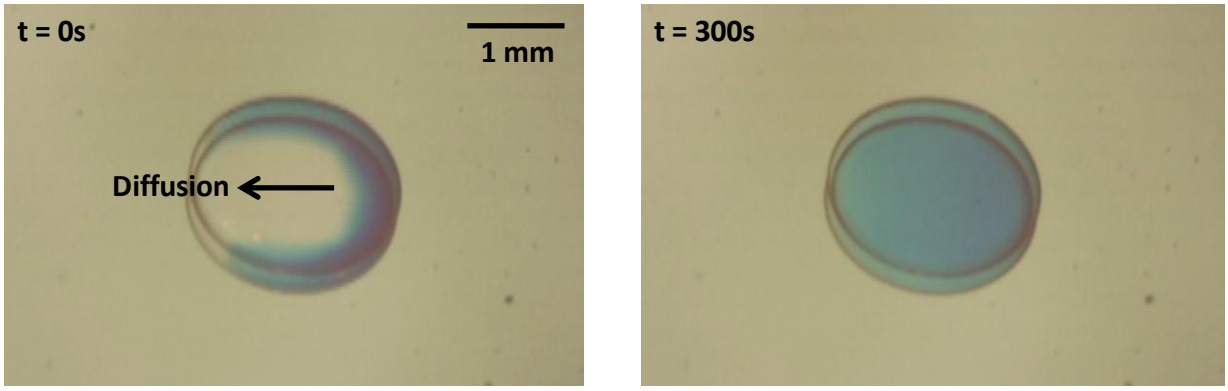

Fig. 4.6 A 50 nl droplet containing blue food dye is joined with another 200 nl water droplet. At t = 0 s the two droplets are merged, and the blue dye starts diffusion towards the left. After 300 s (five minutes), diffusion was complete and the droplet is mixed. Fluidic chamber height = 100 µm.

4.3.3 Low-Frequency Pulsing Mixing

The idea of applying a low-frequency driving voltage to a sessile droplet (with no top cover) was investigated by Mugele et al. [58]. This "pulsing" perturbation is able to introduce a mixing effect to the droplet. Experimentally, we carried out this concept with an OEW device with a top cover (the chamber gap being 100 µm as was similar to that described in Section 4.4.2) and a water droplet, with another water droplet loaded with blue colored food dye. A low-frequency voltage was then applied and pulsing of droplets was observed. However, because there was a top cover in this configuration, the perturbation introduced was much reduced. Nevertheless, the mixing time was reduced to 150 s at a frequency of 200 Hz.

4.3.4 High-Frequency Electro-thermal Mixing

Using high frequency, Garcia-Sanchez et al. [59] was able to heat up a sessile droplet locally using a pin. This localized heating causes a thermal gradient within the droplet, causing fluids to flow and mix. Experimentally, we carried out this concept with an OEW device with a top cover, 100 µm chamber gap, and an AC frequency of 100 kHz. As before, a water droplet with another water droplet loaded with blue colored food dye. A very small light pattern was shone onto the middle of the droplet to mimic the pin heating effect. Flow was observed within the droplet, and mixing time was reduced to 30 s.

4.3.5 Rolling Mixing

Finally, the concept of rolling mixing was explored by Paik et al. [55, 56] and Fowler et al. [57] as a way of introducing striation layers within the droplet. A roll is defined as one complete fold of the droplet striation layer, after N rolls, 2^N striation layers are formed. This greatly decreases the diffusion length between mixtures and exponentially decreases the mixing time. In addition, a mixing path was explored to find a certain path with the least flow reversibility.

The OEW device is well suited to explore rolling mixing and least reversible flow paths. The OEW will allow droplets to mix anywhere on chip and in any path configuration. Different mixing paths, with droplet translation speed 1 cm/s, were explored including straight line path (mixing time 3 s), circular mixing path (mixing time 2 s), square mixing path (mixing time 2 s), and a figure-eight path (1.5 s). The figure-eight path (Fig. 4.7) was observed to have the fewest "dead spots" and the fastest mixing time.

In conclusion, due to its low Reynolds number, diffusive mixing in droplet microfluidics is slow. Rolling mixing, which introduces striation layers and facilitates shorter diffusion length, results in faster mixing times. We found that rolling in figure-eight path is the fastest mixing method, with a 200× increase in mixing speed when compared to passive diffusion.

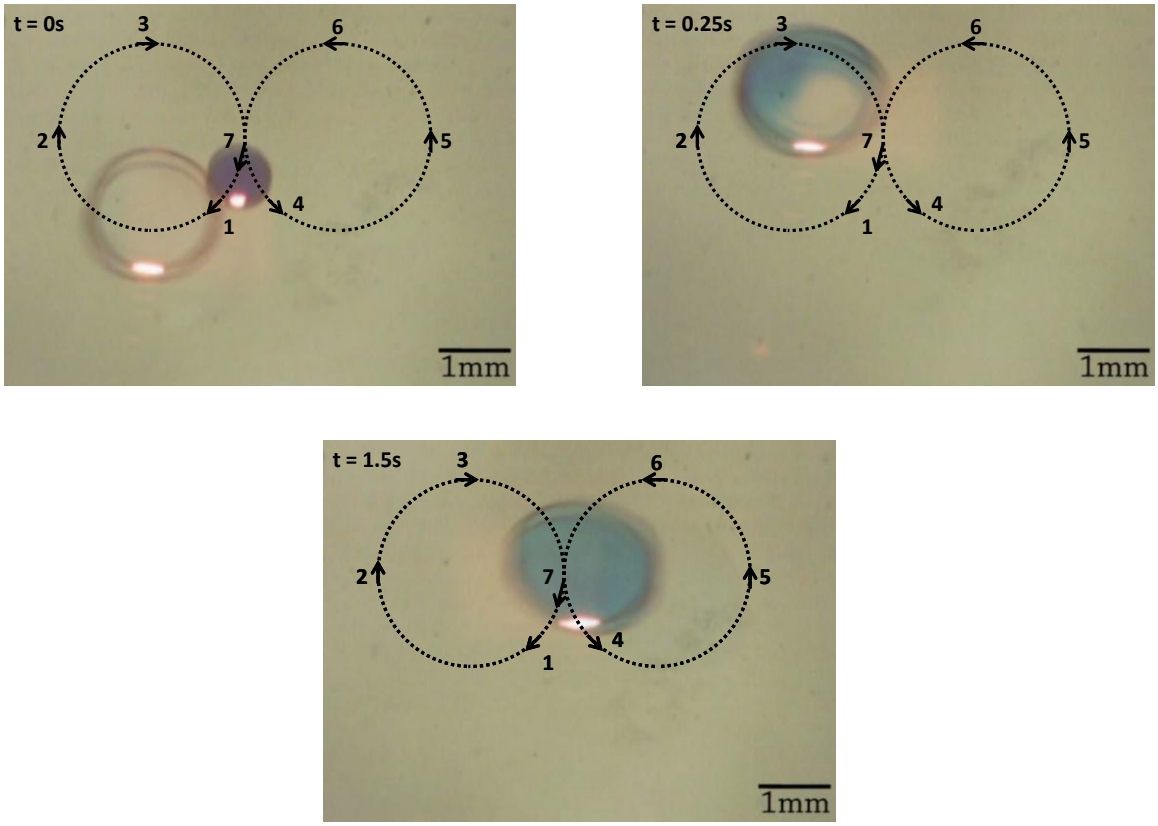

Fig. 4.7 A 50 nl droplet containing blue food dye is mixed with joint with another water droplet. At *t* = 0 s the two droplets are merged. Rolling the droplet increases striation layers, which then decreases diffusion length. The figure-eight mixing path was observed to have the fewest "dead spots," the least flow reversibility, and the fastest mixing time. After 1.5 s, rolling was complete and the droplet was mixed. Chamber height = 100 µm.

4.4 Crescent Electrode for Heating Reduction

4.4.1 Introduction

Chapter 2 presented the OEW device in operation, with a digital light projector and square light patterns. However, the light intensity (~1 W/cm^2) used in OEW causes a temperature rise in the droplets due to absorptive heating in the photoconductive layer. Excessive heating is undesirable, as many chemical or biological reactions are temperature sensitive. This section proposes a novel ring-shaped virtual electrode to reduce heating. Experimentally, the temperature of the droplet is measured using temperature-sensitive hydrogel microspheres as an *in situ* temperature sensor. The maximum temperature rise of 0.35°C is 15 times lower than droplets actuated by square virtual electrodes.

4.4.2 Ring Electrode Droplet Actuation Efficiency

Figure 4.8(a) shows a 2 µl droplet actuated by a square light pattern. The droplet is immersed in oil, and moves at 3 mm/s with a bias voltage of 24.8 V_{ppk} at 10 kHz. The amount of heating is proportional to the two-dimensional area of the illumination, while the droplet actuation force is proportional to the one-dimensional contact line of the droplet experiencing an electrowetting force. Therefore, we can reduce heating by using ring-shaped electrodes around the water/oil interface [see Fig. 4.8(b)].

This has been verified experimentally. Figure 4.8(b) shows that although the droplet transported at the same speed (3 mm/s) using a half-ring-shaped light pattern, the actuation voltage of the ring electrode is only 3% higher (25.6 Vppk) and within experimental error. We have also investigated the effectiveness of the ring electrode as a function of the angle it subtends (see inset of Fig. 4.9). Figure 4.9 shows the actuation voltage required to move droplet at 3 mm/s versus the angle. As expected, the minimal voltage (the most effective actuation) occurs at θ = 90°. However, good movement of the droplet is achieved with angles as small as θ = 45°.

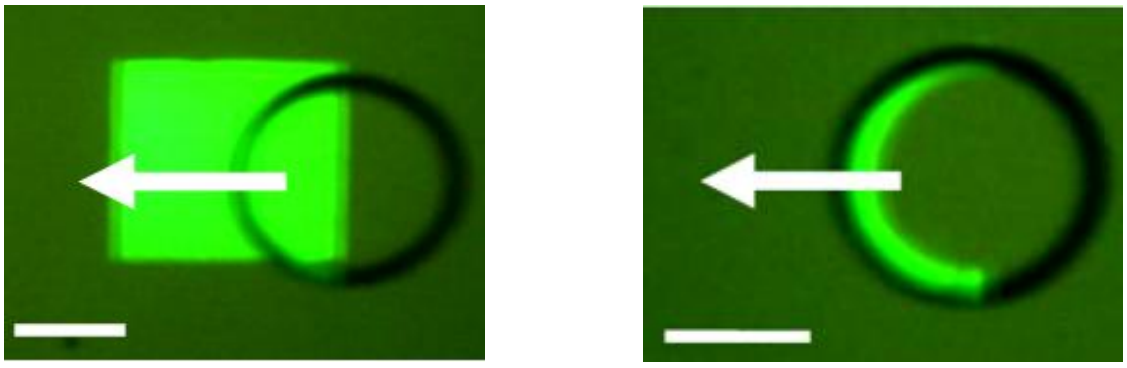

(a) **(b)**

Fig. 4.8 (a) 2 µl droplet actuated in the direction of arrow using square electrode at a speed = 3 mm/s, a voltage = 24.8 Vppk, a frequency = 10 kHz, and a scale bar = 1mm; and (b) 2 µl droplet actuated in the direction of arrow using half-ring electrode at a speed = 3 mm/s, a voltage = 25.6 Vppk, a frequency = 10 kHz, and a scale bar = 1mm.

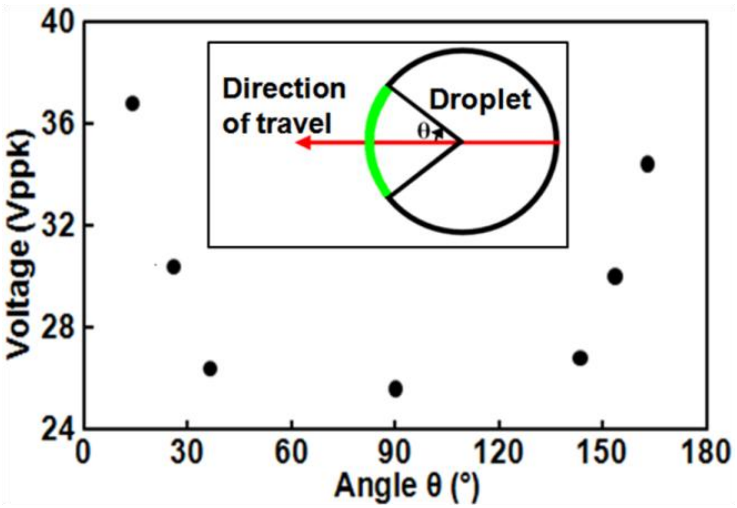

Fig. 4.9 Bias voltage required to move droplet at 3 mm/s versus angle θ subtended by the ring electrode (see inset). Minimum voltage (strongest actuation) is obtained at θ = 90°. Effective actuation of droplets is achieved with angles as small as θ = 45°.

4.4.3 Temperature Monitoring and Reduction

The temperature of droplets is monitored by thermo-sensitive hydrogel microspheres whose size changes rapidly with temperature [60]. The hydrogel microspheres are contained within the droplets, as shown in Fig. 4.10. The size of hydrogel microspheres within droplets can be tracked in real time under various illumination patterns. Consequently, the temperature within droplets can be referenced using temperature calibrated against hydrogel microsphere radius [Fig. 4.11(a)]. When a droplet is half illuminated by a square light pattern [Fig. 4.10(a)], hydrogel microspheres on the illuminated side rapidly shrink in size. This indicates a temperature increase in the illuminated side of the droplet by 4°C within 60 seconds [Fig. 4.11(b)]. The total temperature increase was 5.3°C, with the increase primarily attributed to the dissipation of absorbed optical energy. In contrast, by switching to a quarter ring light pattern with θ = 45° [Fig. 4.10(b)], the total temperature rise was only 0.35°C [Fig. 4.11(b)], which is roughly a 15-fold reduction from that of the square pattern. Additional reduction in the temperature rise is possibly by removing the optical illumination when droplets actuation is not necessary.

(a) **(b)**

Fig. 4.10 (a) Square-shaped light pattern projected on a droplet. Hydrogel microspheres are contained within the droplet. Temperature increase of 5.3°C is observed. The scale bar is 1mm; and (b) quarter-ring-shaped light pattern projected on a droplet. Hydrogel microspheres are contained within the droplet. Temperature increase of 0.35°C is observed. The scale bar is 1mm.

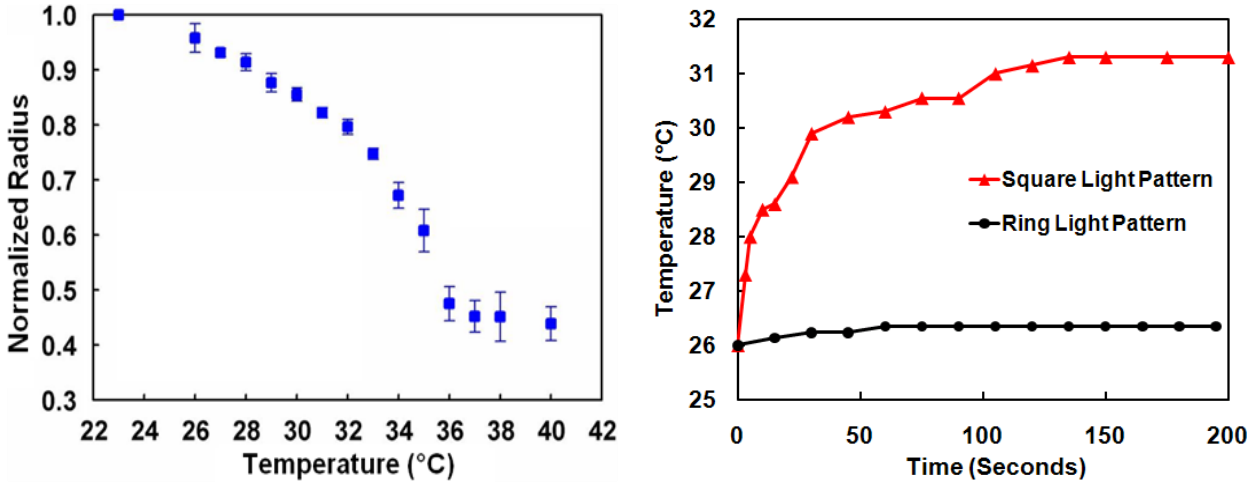

Fig. 4.11 (a) Calibration curve used to derive droplet temperature *in situ* as a function of measured hydrogel microsphere radius, as presented in [60]; and (b) temperature within droplet against time for both the illuminated side of square-shaped electrode and the quarter-ring-shaped electrode.

This section has demonstrated that ring illumination pattern is very effective in reducing heating without sacrificing actuation force in optoelectrowetting. The temperatures of the droplets were measured quantitatively using thermo-sensitive hydrogel microsphere as *in situ* temperature monitors. The heating of the droplet was reduced from 5.3°C to 0.35°C through the use of a ring-shaped electrode, without compromising on droplet actuation speed.

4.5 On-Chip Blade for Accurate Splitting of Droplets

4.5.1 Introduction

The splitting of droplets is an integral operation for digital microfluidics: it is required for both drawing droplets from reservoirs and for controlling droplet volume in multi-step assays, titration, and multiplexing bioassays. The current droplet splitting method relies on hydrodynamic instability as a droplet is pulled apart by two opposing electrowetting electrodes [18, 61]. It is inaccurate because the break point of the unstable neck is unpredictable. The splitting ratio is also limited by the size of the electrode and is constrained to roughly two equal daughter droplets. Improving droplet dispensing accuracy from a reservoir is possible but requires a capacitance measurement and feedback control system [62, 63]. This section describes a novel technique to controllably and accurately slice droplets with integrated "Teflon blades" in the OEW platforms.

4.5.2 Cutting Using Teflon Blade

The schematic of the Teflon blade and the droplet slicing process is illustrated in Fig. 4.12. The Teflon blade is integrated with the OEW device. The blade (3.5 mm long, 400 μm wide, and 130

μm tall) is sandwiched between a top indium-tin-oxide (ITO) and bottom optoelectrowetting electrodes [Fig. 4.12(c)]. The blade has a sharp wedge with a 55° angle. To slice a droplet, the droplet is first elongated by a rectangular light pattern and then moved towards the blade at the desired cutting location. As the elongated droplet moves across the blade, it is effectively "sliced" into two droplets. Because the blade introduces perturbation at a specific location of the droplet, it minimizes instability and unpredictability in the breaking process, resulting in a more accurate and controlled split.

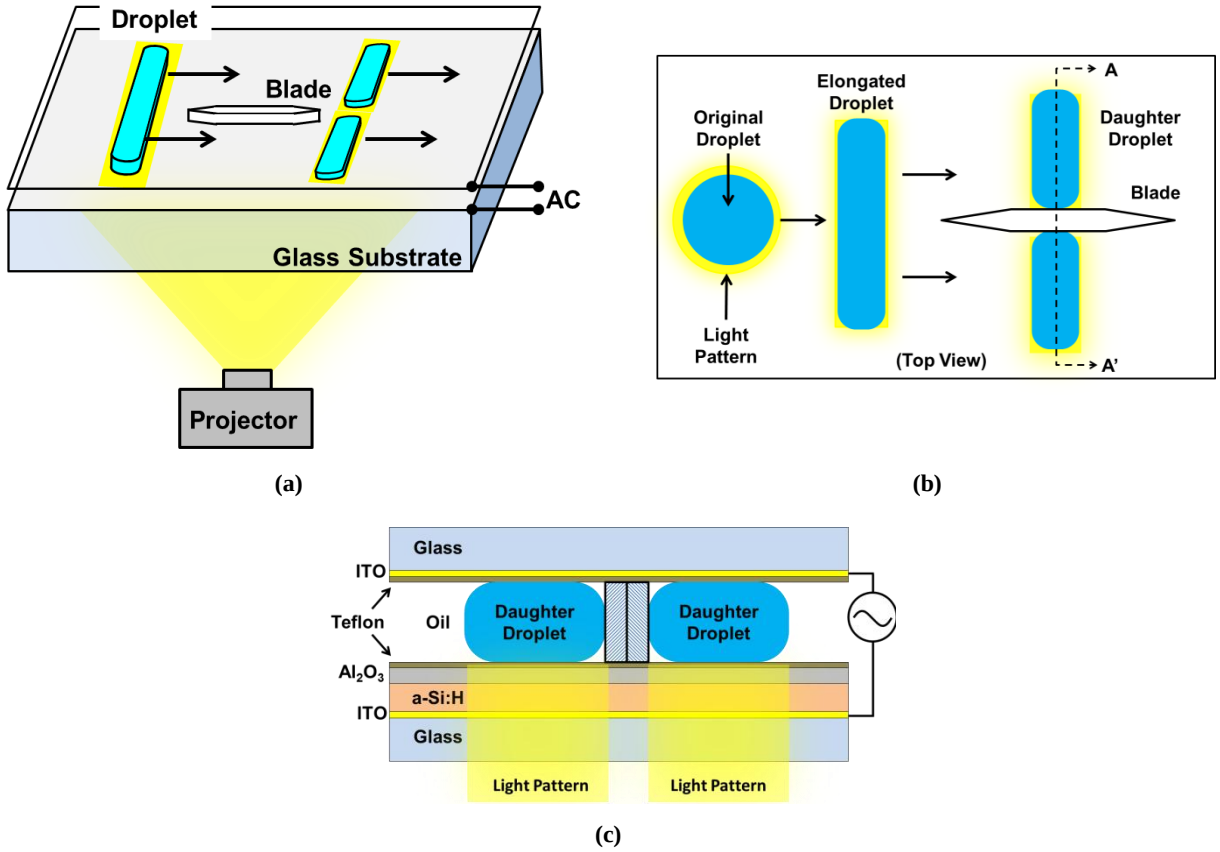

Fig. 4.12 (a) Schematic illustrating droplet slicing with integrated Teflon blade on light-actuated digital microfluidic platform; (b) top view; and (c) cross section along AA′. The droplet is first elongated by a rectangular light pattern. It is sliced into two droplets as it moves across a Teflon blade. The break point of the droplet is precisely defined by the position of the blade, leading to accurate control of droplet splitting ratio and volume.

4.5.3 Droplet Cutting Results and Discussion

The volumes of the daughter droplets depend on the position of the blade. Figure 4.13 shows the captured video images of slicing an elongated 600 nl droplet into two equal (300 nl + 300 nl) and unequal (120 nl + 480 nl) droplets. The droplet splitting ratio can be accurately controlled by the blade position. Figure 4.14 shows the fractional volume of a daughter droplet versus the blade position for a 600 nl mother droplet. The volume varies linearly with the blade position and agrees

well with the theoretical prediction. The theory assumes a linear cut through the droplet at the tip of the blade. The good agreement attests the accuracy and predictability of the droplet cutting process by the blade. Daughter droplets with volumes of 10% to 90% have been obtained by varying the blade position.

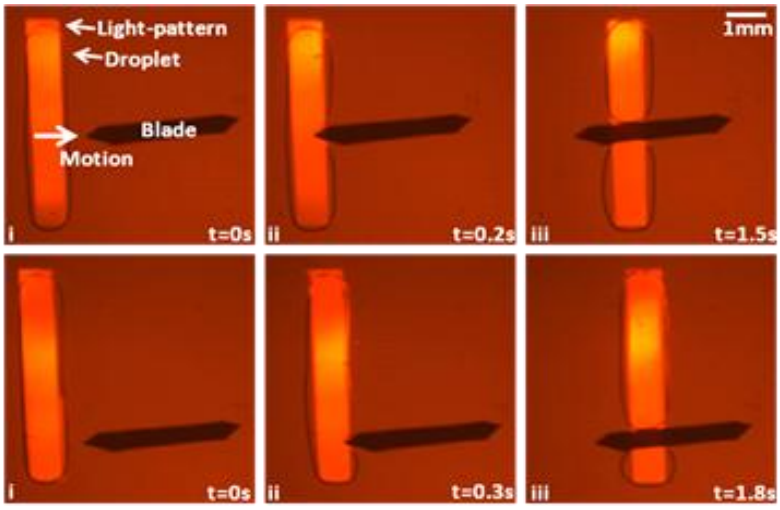

Fig. 4.13 Video images illustrating droplet slicing by a blade. A 600 nl droplet is stretched into a bar and moved towards the Teflon blade. (Top) Splitting into two equal droplets of 300 nl. (Bottom) Splitting into two droplets of 120 nl and 480 nl.

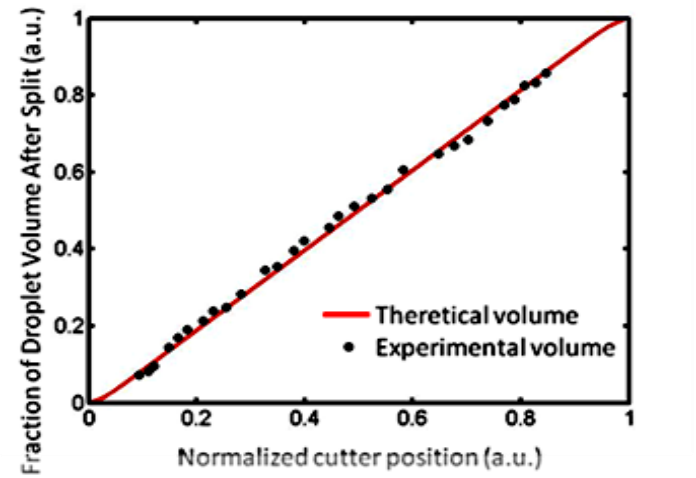

Fig. 4.14 Fractional volume of the daughter droplet versus the position of the blade along the mother droplet for a 600 nl droplet. The volume varies linearly with the blade position and agrees well with theoretical prediction.

As another demonstration of the controllability of the droplet cutting process, a 602 nl droplet was sliced eight times to create eight equal droplets; see in Fig. 4.15. The volumes of the eight daughter droplets are measured to be 75.2 nl, with a standard deviation of 1.6 nl or 2%.

Serial dilution is an integral part of many analytical applications such as multi-step assays and titration. In this demonstration, a 360 nl droplet (droplet 1 in Fig. 4.16) loaded with blue food dye is elongated and split by the blade into two droplets with a 5:1 ratio. The smaller split droplet

(60 nl) is merged with another water droplet of 300 nl to form droplet 2. The merged droplet is rapidly mixed by rolling across the device surface. Droplet 2 then undergoes 5:1 splitting using the blade, and this serial dilution process is repeated such that six droplets are formed with progressive sample dilution of 6×, and total dilution factor of 65 = 7776 (Fig. 4.16). Transmission of red light through these droplets has been measured, and the percentage transmission is presented in Fig. 4.17. A theoretical curve based on Beer-Lambert law is plotted for comparison, with molar absorptivity of 1.3×10^6 $M^{-1}cm^{-1}$, initial dye particle concentration of 0.1M, and absorption length of 100 μm.

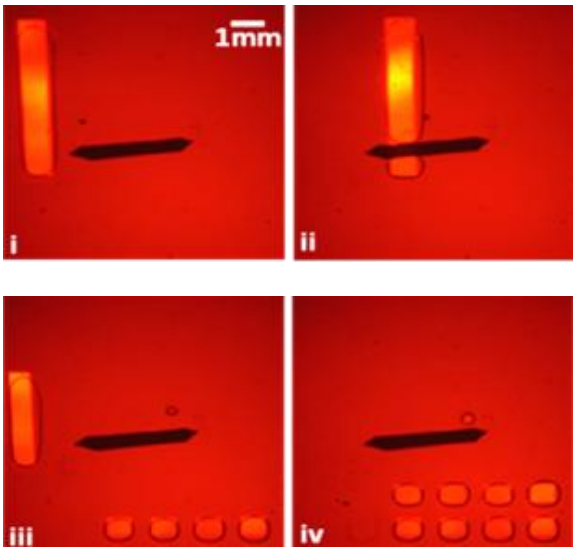

Fig. 4.15 Droplet array created by slicing a 600 nl droplet seven times, resulting in eight droplets of 75 nl each. The standard deviation of the droplets is 1.6 nl (2%).

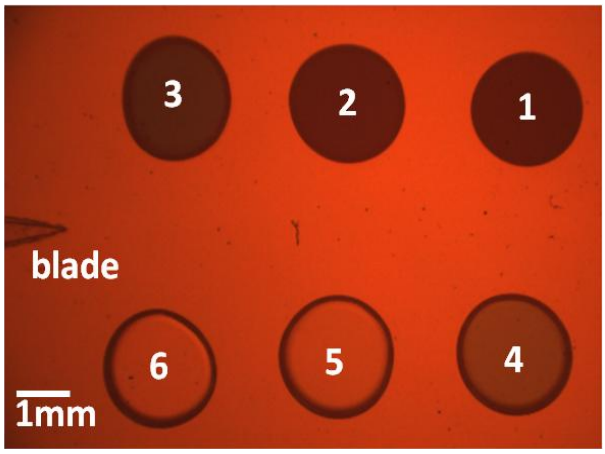

Fig. 4.16 Light micrograph of 300 nl droplets after serial dilution. Droplet 1, loaded with blue food dye, is split 5:1 and the smaller split droplet (60 nl) is merged with another water droplet of 300 nl to form droplet 2. The serial dilution process is repeated such that six droplets are formed.

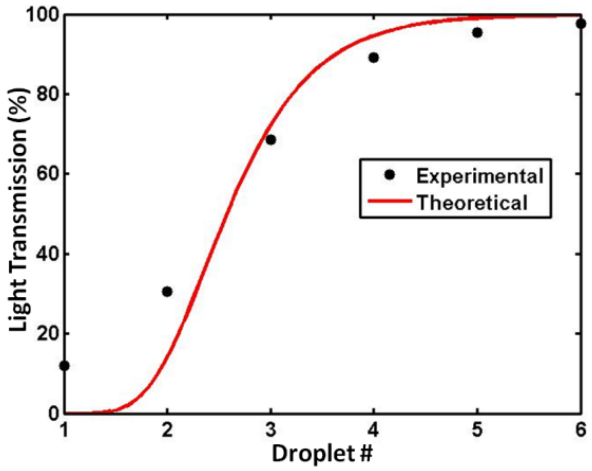

Fig. 4.17 Percentage transmission of light through the six droplets numbered in Fig. 4.16, with droplet 1 being most concentrated, with dye particles (0.1M) and subsequent droplets serially dilution by 6×. Theoretical comparison based on Beer-Lambert law is plotted for reference.

4.6 Conclusion

This chapter described the basic functionalities of OEW devices: namely, droplet dispensing, parallel motion, arraying, splitting and merging, and movement of droplets with different volume. Furthermore, we have demonstrated that droplets could be mixed in seconds when rolled across the device surface in a figure-eight pattern. In addition, novel crescent-shaped electrodes are shown to eliminate heating of the droplets while maintaining the same droplet actuation speed. Lastly, we introduced an on-chip Teflon blade for the precise splitting of droplets. These functions provide the basic building blocks for many Lab-on-chip (LOC) applications.

Chapter 5 Isothermal Real-Time Polymerase Chain Reaction Detection of Herpes Simplex Virus Type 1 on an Optoelectrowetting Platform

5.1 Introduction

Microfluidics-based polymerase chain reaction (PCR) systems have gained much interest in recent years because of their potential to miniaturize and automate the multi-step PCR processes in molecular biology. PCR applications using EWOD (electrowetting-on-dielectric)-based digital microfluidics [22, 23] have been studied by Hua et al. [22], who used EWOD to shuttle droplets back and forth between a hot and a warm zones on a chip for DNA amplification. The different temperature zones limited the PCR droplets to a one-dimensional array; to date, only four simultaneous PCR droplets have been demonstrated by Hua et al. Microdroplet-PCR can pack a large number of surfactant-stabilized, oil-emulsified droplets for digital PCR and large-scale enrichment for targeted sequencing [64]. However, it does not have the flexibility to manipulate individual droplets. Isothermal PCR, such as Helicase-dependent nucleic acid amplification (HDA) [65], does not require separate temperature zones and is attractive for microfluidics.

Herpes simplex, caused by the Herpes Simplex Virus (HSV), is a commonly found sexually transmitted disease; HSV symptoms may include meningitis, sores, and skin infections. Herpes Simplex Virus Type 1 (HSV-1) is typically linked to oropharynx infections whilst HSV-2 is typically linked to neonatal or genital infections [66]. Cell culturing of lesion swab content, such as the Enzyme-Linked Virus Inducible System (ELVIS®, Diagnostics Hybrids Inc., Athens, OH) [67], are the most common way of testing HSV currently. However, cell culture-based diagnostics and test results are slow (16 hours or more). Recently, HDA dependent detection of Herpes Simplex Virus has been demonstrated by BioHelix Corporation (Beverly, MA) [68, 69]. Individual patient samples can be rapidly tested using portable devices. However, in these devices, the reagent volume used is large and each device is only capable of testing one sample.

This chapter describes the optoelectrowetting (OEW) platform for real-time, Helicase-dependent PCR amplification and detection of HSV-1. Similar to EWOD-based digital microfluidics, OEW offers reduced sample/reagent volume, faster reaction time, and higher automation. In addition, OEW can be easily scaled up to larger array format and a wider range of droplet volume. The HSV-1 viral lysate was detected by the HDA amplification on-chip within 45 minutes.

5.2 OEW Isothermal PCR Operation

5.2.1 Operation and Set-Up

The schematic of the OEW device, shown in the inset of Fig. 5.1, consists of an indium-tin-oxide (ITO)-coated glass substrate, a 1 μm thick photoconductive a-Si:H layer deposited via plasma-enhanced chemical vapor deposition, a 100 nm layer of dielectric Al_2O_3 deposited by atomic layer deposition, and a 25 nm film of hydrophobic layer formed by spin coating 0.2% Teflon (3000rpm, 30s). The top electrode consists of a Teflon-coated ITO glass wafer.

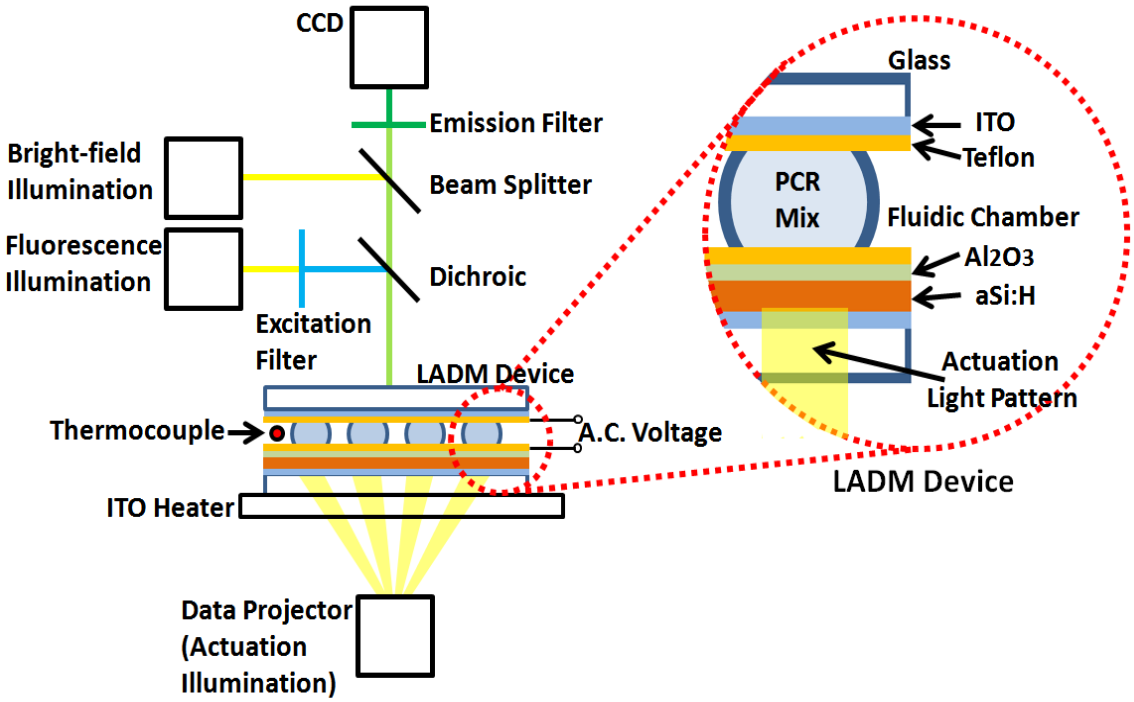

Fig. 5.1 The experimental setup for real-time isothermal PCR in OEW devices. Optical patterns from the projector control the droplet motion on OEW. An ITO heater is positioned below the device, and a thermocouple is inserted into the fluidic chamber to provide uniform heating and temperature feedback control. The fluorescence imaging system allows monitoring of the PCR process in real time. The inset shows the schematic of the OEW device.

The microfluidic chamber is formed between the top and bottom plates separated by a 500-µm-thick spacer. AC bias (40 Vppk, 10 kHz) is applied to the top and bottom ITO substrates. Light from a commercially available projector is focused onto the device (Fig. 5.1). Optical patterns are generated on a computer and sent to the projector. In the absence of light, the externally applied voltage primarily drops across the highly resistive a-Si:H layer. Upon illumination, the conductivity of the a-Si:H increases by more than 10×. This causes the externally applied voltage to drop across the electrically insulating layers (oxide). This imparts an optoelectrowetting force that causes the droplet to move toward the illuminated region. As a result, the illuminated area acts as a virtual electrode. The total manipulation area on chip is 1.5 cm × 1.1 cm. Bright-field illumination and a CCD camera (Sony, XCD-X710) are used for visualization and recording. Green Fluorescence Protein (GFP) excitation and read-out are incorporated into the set-up with emission, excitation and dichromatic mirror (kit 39002 - EGFP/FITC/Cy2/AlexaFluor 488) obtained from Chroma Technology Corp.

5.2.2 Protein Surface Fouling Control with Surfactants

The isothermal PCR mix used in this study contains many proteins such as Helicase, Polymerase, and Single-Strand Binding Protein. These proteins in OEW droplets, when not properly encapsulated in the droplet, will adsorb onto the hydrophobic Teflon surfaces causing non-specific adsorption and unreliable droplet actuation. Non-specific adsorption of biomolecules at interfaces is an issue in microfluidics [70, 71]. For emulsion-based droplets in channels, surfactants are added to droplets to encapsulate biomolecules and to stabilize the droplets [8, 9]. In EWOD-based droplet systems, Pluronics surfactants are added to droplets to encapsulate proteins and to prevent non-specific adsorption [72]. Pluronics are co-block polymers of poly(propylene) (PPO) and poly(ethylene oxide) (PEO). Surfactants are useful in confining biomolecules and prevent non-specific adsorption because it coats the interface of water and oil, with its hydrophobic end facing oil and hydrophilic end facing water [Fig. 5.2]. By coating the interface, surfactants prevent proteins from adhering to the solid-water interface.

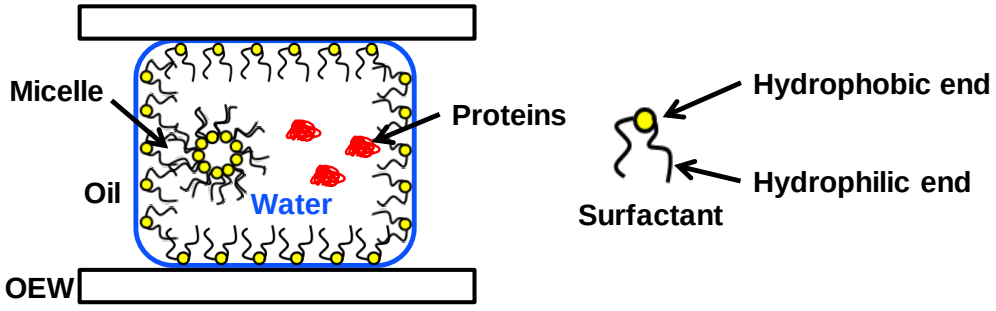

Fig. 5.2 Surfactant coating of an OEW droplet. Surfactant is able to block the oil-water interface hence prevent proteins within the droplet from adhering to the surface of the device.

Surfactant solution has been explored for OEW isothermal PCR. We used Pluronic F-68 as surfactant for OEW droplets due to its high PEO content and high PPO chain lengths, hence acting as a more effective surfactant [73]. The optimal surfactant concentration was determined experimentally. Protein-loaded test droplets were made from phosphate buffer solution containing 1% (10 mg/ml) Bovine Serum Albumin (BSA, Sigma Aldrich, St. Louis, MO), with different % w/v added concentrations of Pluronic F-68. Similar sized test droplets were injected into OEW devices and translated back-and-fourth along a 1 cm test path on chip. Each successful droplet actuation back-and-fourth along this path is recorded as one "lap". The number of completed laps for different Pluronic F-68 concentrations is shown in Table 5.1. Droplets with no BSA and no Pluronic were also tested as control.

Table 5.1 Surfactant Concentration Effect on Actuation of Protein-loaded Droplets

Pluronic F-68 (% w/v)	Droplet Completed Laps
0%	12-18
0.05%	42-59
0.2%	100+
1%	35-67
0% and no BSA (control)	100+

From Table 5.1, we can see that 0.2% is an optimal Pluronic F-68 surfactant concentration for protein-loaded droplet actuation. The critical micelle concentration at room temperature for Pluronic F-68 is 1.05% [73], which means that at low concentrations, not all of the water-solid interface is surfactant coated. We hypothesize that at higher surfactant concentration, liquid-solid interfacial tension γ_{ls} is lowered, causing electrowetting to be less effective.

From this section, we conclude that a 0.2% concentration of Pluronic F-68 surfactant should be added to OEW isothermal PCR droplets to prevent surface fouling and to perform reliable droplet actuation.

5.3 Isothermal PCR Methods

The fluidic chamber is first flooded with silicone oil (1.0 cSt DMS Trimethylsiloxy terminated Polydimethylsiloxane). Droplets are introduced into the fluidic chamber via a syringe pump (KD Scientific, 780210) and Teflon tube. Temperature in the fluidic chamber is monitored by a thermocouple (Omega Engineering, 5SC-GG-K-30-36) and set by a close-loop controller (Omega Engineering, CN7533) regulating the electrical power supplied to a planar ITO-heater attached to the bottomed of the device.

A Helicase-dependent PCR kit (IsoAmp®III tHDA) and blank viral transport medium were acquired from Biohelix Corporation (Beverly, MA), HSV-1 (MacIntyre Strain) Purified Viral Lysate was acquired from Advanced Biotechnologies (Columbia, MD); all viral lysate were centrifuged at 3100 rpm for 10 minutes and supernatant extracted for use. Forward and reverse primers were designed to target and amplify a 100 bp region of the HSV glycoprotein B gene [68], and were acquired from Integrated DNA Technologies (Coralville, IA). The primer

sequences are shown in Table 5.2. EvaGreen Fluorescence dye was acquired from Biotium Corp. (Hayward, CA) and ROX reference dye was acquired from Life Technologies (Carlsbad, CA). The isothermal PCR master mix was prepared with components according to One-Step qHDA of the IsoAmp®III tHDA kit manual [74], except without the component of DNA. The details of the master mix protocol is shown in Appendix C. 0.2% Pluronic F-68 (Sigma Aldrich, St. Louis, MO) surfactant was added to all reagents to prevent non- specific protein adsorption to the device surface [72].

Table 5.2 Sequence of Primers

Forward Primer	5'-TTCAAGGAGAACATCGCCCCGTACAA-3′
Reverse Primer	5'-TAAACTGGGAGTAGCGGTGGCCGAAC-3′

5.4 OEW Isothermal PCR Results

5.4.1 Droplet Array Formation and Amplification

A 4 × 4 array was formed by optoelectrowetting, as shown in Fig. 5.2. 400 nl PCR master mix droplets were dispensed from a tube and transported at 2 mm/s to merge with HSV-1 droplets of 35 nl containing 1.69×10^4 viral- particles/nl (prior to lysis); the final HSV-1 concentration was 1.36×10^3 viral-particles/nl. The merged droplet was then mixed by rolling back and forth [75], and the mixed droplet were transported to a spot in the 4 × 4 array.

The array then underwent isothermal PCR amplification at 64°C for 45 minutes. The real-time amplification curves and final fluorescence signal of the 16 droplets array is shown in Fig. 5.3. At threshold Ct, the mean amplification time was 16.0 minutes with standard deviation of 0.74 minutes. The array size is 4× larger than that achieved with EWOD shuttling between temperature zones [22]. The 16 on-chip droplets were extracted after the reaction, and gel electrophoresis confirmed that the amplified product was 100 bp.

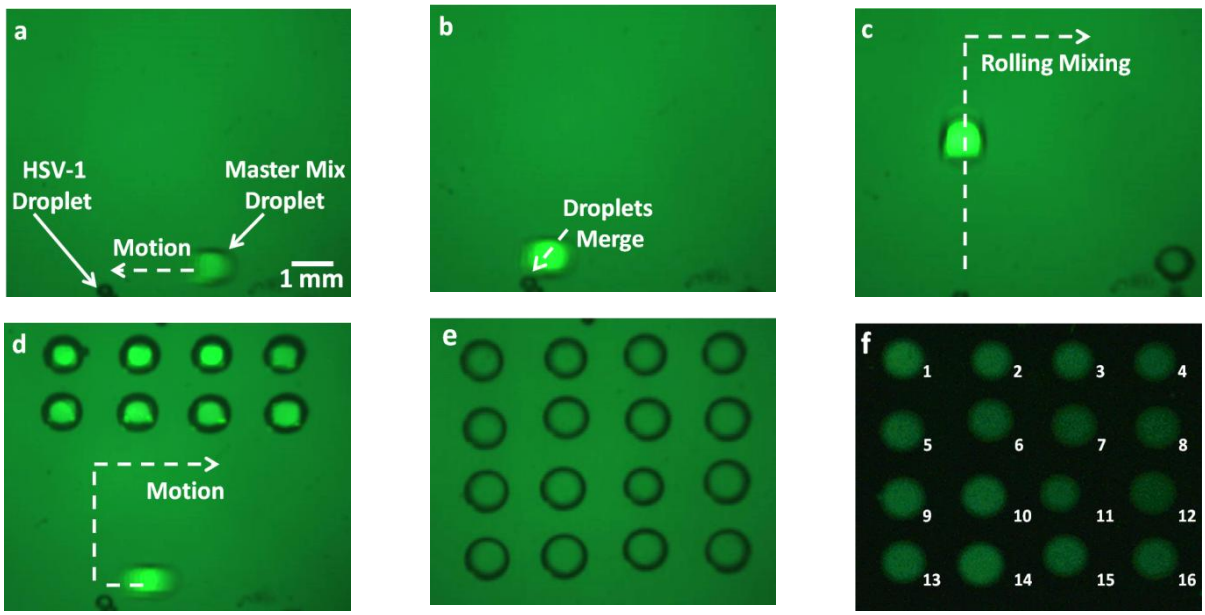

Fig. 5.3 Droplet array formation and amplification. (a)-(c) A droplet of 400 nl isothermal PCR master mix was dispensed from a tube and subsequently transported by a light pattern at 2mm/s and merged with a 35 nl droplet containing HSV-1 viral lysate; the merged droplet is then mixed by rolling on-chip and positioned into an array; (d)-(e) dispensing, merging, mixing and position is repeated to form a 4 × 4 array; and (f) fluorescence signal of droplets after amplification. Labeled droplet number corresponds to droplet # of amplification curve in Fig. 5.3.

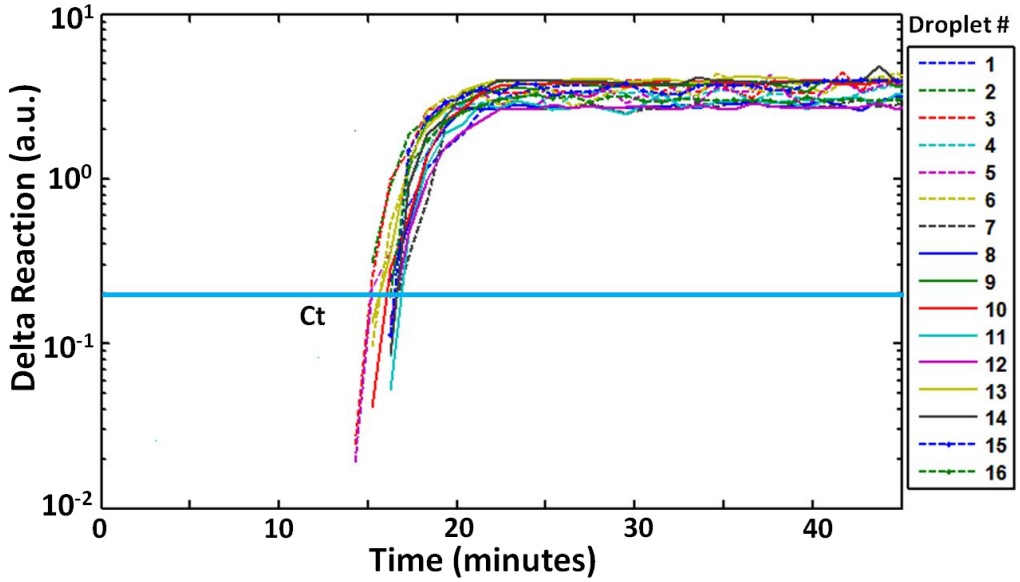

Fig. 5.4 Real-time isothermal PCR amplification curves of the 4 × 4 droplet array with PCR mix containing 1.36×10^3 viral-particles/nl (droplet # as shown in Fig. 5.2(f). At threshold Ct, the mean-amplification time is 16.0 minutes, with standard deviation of 0.74 minutes.

5.4.2 Different DNA Concentration Amplification

A 2 × 2 array with two different viral concentrations, differing by 10×, was formed by optoelectrowetting. Two 800 nl PCR master mix droplets were dispensed from a tube and transported at 2 mm/s to each merge with a HSV-1 droplet of 80 nl containing 1.69×10^4 viral-particles/nl (prior to lysis), resulting in a HSV-1 concentration of 1.45×10^3 viral-particles/nl. The merged droplets were then mixed and transported to the spots in the array. Two other 800 nl PCR master mix droplets were mixed with 80 nl droplets with 1.69×10^3 viral- particles/nl, resulting in a HSV-1 concentration of 1.45×10^2 viral-particles/nl. The final array positioning is shown in Fig. 5.4 inset. The array underwent isothermal PCR amplification at 64°C for 45 minutes. The real-time amplification curves are shown in Fig. 5.4. At threshold Ct, the mean amplification times are 16.75 and 23.55 minutes, respectively, for 1.45×10^3 and 1.45×10^2 viral-particles/nl droplets.

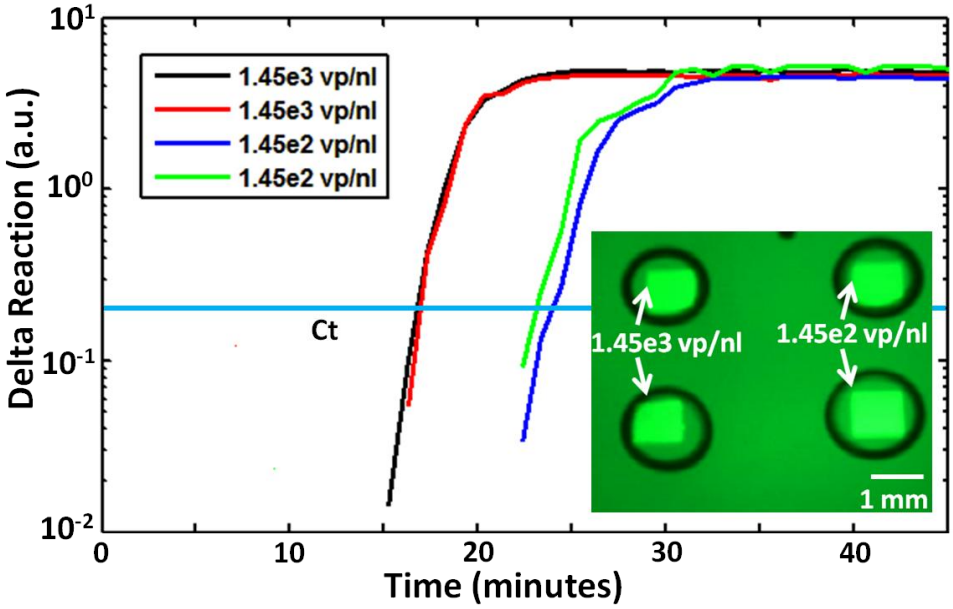

Fig. 5.5 Real-time isothermal PCR amplification curves of four droplets of 880 nl each, with two different viral concentrations. Inset: Droplets on the left contain 1.45×10^3 viral- particles/nl, while those on the right contain 1.45×10^2 viral- particles/nl. At threshold Ct, the amplification time for 1.45×10^3 and 1.45×10^2 viral-particles/nl are 16.75 and 23.55 minutes, respectively.

5.4.3 DNA Cross Contamination Study

To study the cross contamination among droplets, we combine both positive and negative control droplets on the same OEW chip. A 4 × 4 array was formed using pre-mixed droplets of 400 nl each. Eight of the droplets were positive controls that contained PCR master mix and 1.45×10^3 viral-particles/nl HSV-1 viral lysate. The other eight droplets were negative control containing PCR master mix and blank viral transport medium.

Positive and negative control droplets were dispensed from tubes sequentially and

transported to form an array. Figure 5.5 (a)-(c) shows how positive and negative control droplets cross paths on-chip. After arraying, the droplets then went through isothermal PCR amplification at 64°C for 45 minutes. The final fluorescence signal on-chip is shown in Fig. 5.5 (d).

Figure 5.5(d) shows that no negative droplets (columns 2 and 4, indicated as "N") displayed amplification, despite crossing paths with positive control droplets (columns 1 and 3, indicated as "P"). In Fig. 5.6, the average fluorescence reading for the eight positive and eight negative control droplets, normalized over the baseline fluorescence reading, is plotted over time, showing amplification only for the positive control droplets.

To ensure that the negative control reagent was not inhibiting the amplification process, viral lysate was added to negative control reagent such that the viral content within reagent became 1.45×10^3 viral- particles/nl. This reagent displayed amplification thus confirming the negative control reagent was not inhibiting the reactions. Consequently, we confirmed that there was no cross contamination on-chip.

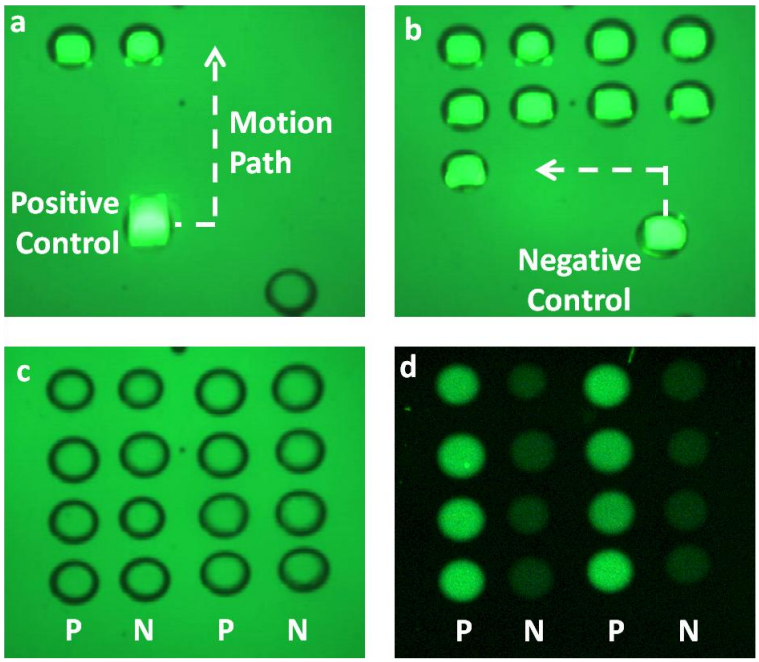

Fig. 5.6 (a)-(c) Positive and negative control droplets were dispensed from tubes and transported into array position. The negative control droplets contain blank viral transport medium while the positive control droplet contain 1.45×10^3 viral-particles/nl. The first and the third columns are positive control droplets, while the second and the fourth columns are negative control; and (d) the fluorescence image of the final amplified products after 45 minutes at 64°C. No cross contamination was observed.

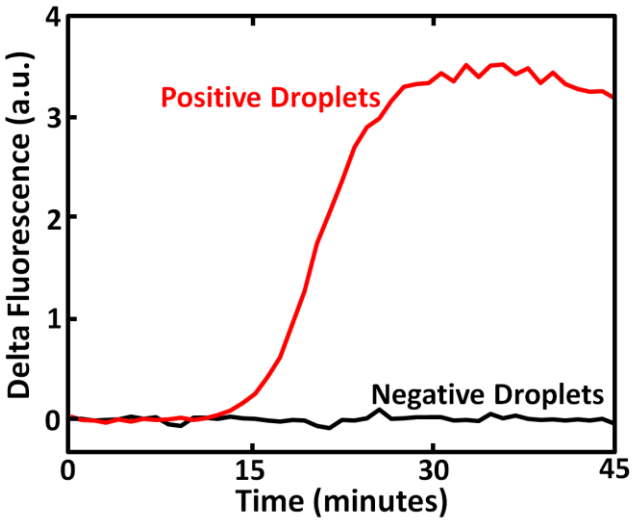

Fig. 5.7 The average fluorescence reading versus time for the 8 positive and 8 negative control droplets. The fluorescence is normalized to the baseline fluorescence reading.

5.5 Conclusion

In conclusion, the OEW platform has been successfully used to perform a biological process. OEW droplet arrays were used for real-time Helicase-dependent isothermal polymerase chain reaction detections of Herpes Simplex Virus Type 1. The OEW set-up was modified to incorporate fluorescence imaging. A 16-droplet array was formed to demonstrate on-chip dispensing, mixing, transporting, and HSV-1 nucleic acid amplification. HSV-1 detection can be performed in 45 minutes without cross contamination on-chip.

Chapter 6 Optoelectronic Tweezers (OET) for Long-Term Single Mammalian Cell Culture

6.1 Introduction

There is increasing interest in single-cell analysis to study the heterogeneity of cells in various biological systems. Microfluidics is an ideal platform for single cell analysis. Various types of microfluidic devices have been reported, including trapping of cells within wells using flow [76], surface modification for cell attachment sites [77], and water droplet encapsulation of single cells [8]. Most microfluidic single-cell studies have focused on gene or protein expression, so isolated cells were usually lysed within hours for analysis [76]. To study the differences in long-term behavior of mammalian cells, such as cancer cells, fibroblasts, or stem cells, a need exists for devices that can effectively culture arrays of single mammalian cells into clonal colonies. Micro-fabricated chamber-based culturing systems have been proposed [78, 79, 80], but they typically involve cumbersome fabrication steps and require careful control of channel input and output for cell loading and selection. Our optoelectronic tweezers (OET) [30] device is well equipped to satisfy the need for an easily-addressable long-term single mammalian cell culturing system. OET as a tool has been previously applied to manipulate particles [81], nanowires [82], embryos [83], and non-adherent mammalian cancer cells [84].

This chapter combines the single-cell manipulation capability of OET with patterned surface modifications to create a new platform for long-term culturing of single adherent cells in large discrete growth patches. The current device has a 10 × 10 array of 0.5-mm-diameter growth patches coated with extracellular matrix to promote cell adhesion and proliferation, allowing for the formation of indexed clonal populations. This OET platform presents a powerful tool for sorting and placement of a selected single cell onto a growth patch using projected light patterns. The large growth area allows the cell to expand into a clonal population over two weeks in culture.

6.2 Optoelectronic Tweezers Principle

6.2.1 Dielectrophoresis

The interaction between a non-uniform electric field and the induced dipole of a dielectric particle within the electric field results in a dielectrophoretic (DEP) force imparted on the particle. For a generalized case of the time-averaged force exerted upon a homogenous dielectric spherical particle in a medium subjected to a non-uniform AC electric field, the dielectrophoretic (DEP) force F_{DEP} is governed by [85, 86]:

$$F_{DEP} = 2\pi r^3 \varepsilon_m Re[K(\omega)] \nabla E_{rms}^2 \tag{6.1}$$

where r is the radius of the particle, ε_m is the permittivity of the medium, E_{rms} is the root-mean-square electric field strength, and $K(\omega)$ is the Clausius-Mosotti factor, in the form of:

$$K(\omega) = \frac{\varepsilon_p^* - \varepsilon_m^*}{\varepsilon_p^* + 2\varepsilon_m^*} \tag{6.2}$$

where ε_p^* and ε_m^* are the complex permittivity of the particle and medium, respectively, in the form of:

$$\varepsilon_p^* = \varepsilon_p - j\frac{\sigma_p}{\omega} \tag{6.3}$$

$$\varepsilon_m^* = \varepsilon_m - j\frac{\sigma_m}{\omega} \tag{6.4}$$

where ω is the angular frequency, σ_p and σ_m are the electrical conductivity of the particle and medium, respectively, and ε_p and ε_m are the permittivity of the particle and medium, respectively.

The frequency of the applied AC electrical field will affect the complex permittivity of both the particle and the surrounding medium; consequently, the real part of the Clausius-Mosotti factor, $Re[K(\omega)]$, may vary in magnitude and may be either positive or negative. When $Re[K(\omega)]$ is positive, particles are attracted to the electric field maxima, which is termed positive DEP. When $Re[K(\omega)]$ is negative, particles are repelled from the electric field maxima, which is termed negative DEP.

For mammalian cells, cellular contents are non-homogenous. The Clausius-Mosotti factor is accordingly affected. Hence, for a typical mammalian cell, ε_p^* is changed to reflect the cell as enclosed in a single shell (surface membrane) [87]:

$$\varepsilon_p^* = C_{mem}^* \frac{r\varepsilon_{int}^*}{\varepsilon_{int}^* + rC_{mem}^*} \tag{6.5}$$

where r is the radius of the cell, ε_{int}^* is the internal complex permittivity of the cell, and C_{mem}^* is the complex membrane capacitance:

$$C^*_{mem} = \frac{\varepsilon_{mem}}{d} - j\frac{\sigma_{mem}}{d} \tag{6.6}$$

Consequently, different cell types and sizes will affect the DEP force variably. Thus, dielectrophoresis can be used as a very versatile tool both for manipulation and sorting of cells.

6.2.2 Optoelectronic Tweezers Principle

Optoelectronic Tweezers (OET) utilize light-induced dielectrophoresis to move nano-micro-particles and biological agents such as cells. Shown in Fig. 6.1, the device comprises of a 1-µm-thick photoconductive film of amorphous silicon (a-Si:H) deposited via plasma-enhanced chemical vapor deposition (PECVD) onto an indium-tin-oxide (ITO)-coated glass substrate. A fluidic chamber is formed between the OET substrate and an ITO-coated cover glass with a 100-µm-thick spacer (Fig. 6.1). Cells suspended in low-conductivity medium are introduced to the chamber. A 10 Vppk, 100 kHz AC voltage is applied between the two ITO layers. Detailed fabrication steps are presented in Appendix D.

A light pattern generated by a projector is focused onto the substrate, locally increasing the conductivity of the illuminated a-Si:H by more than 10×. This change in conductivity switches the voltage drop from the photoconductive layer to the fluidic chamber, forming "virtual electrodes" in the area of illumination. These virtual electrodes create a non-uniform electric field within the fluidic chamber, subsequently imparting a dielectrophoretic force on the cells; see Equation (6.1). At 100 kHz, the DEP force is positive, and as a result, cells are attracted and trapped within the virtual electrodes defined by the light pattern. Visually, cells are attracted to the light pattern. Subsequent demonstrations utilize this frequency and positive DEP to move mammalian cells.

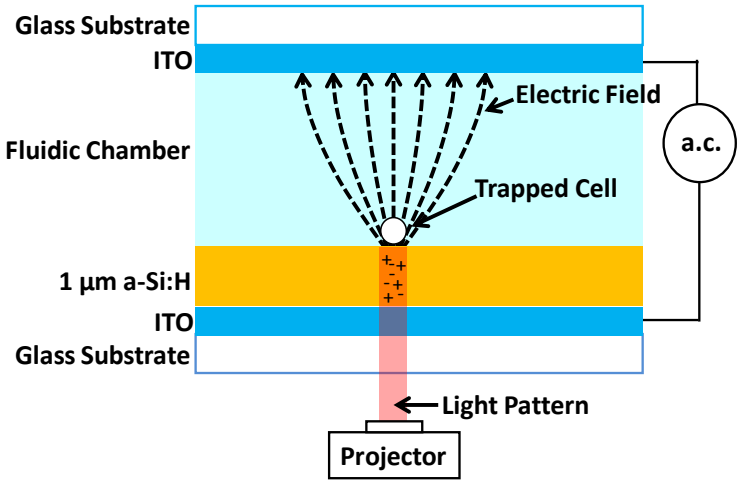

Fig. 6.1 OET operation. An AC bias is applied between the two ITO electrodes. The “virtual electrode” created by a projected light pattern switches the AC voltage drop from the photoconductive a-Si:H layer to the fluidic layer, thus producing a non-uniform electric field in the medium. This non-uniform electric field in turn causes cells to be trapped through dielectrophoretic (DEP) forces.

6.3 OET Surface Modification for Single-Cell Colonal Formation

Previous biological applications of OET involved short-term manipulation and analysis of live or dead mammalian cells [30], mouse embryos [83], human sperm [88], and viruses [89]. Long-term culture of mammalian cells in culture medium was achieved [84], but only with non-adherent cell types and using a phototransistor-based device that involved many fabrication steps.

The focus of this section is the use of OET to culture single adherent mammalian cells on the scale of days or weeks, and to observe their proliferation rates and colony formation potential. In order to corral colonies formed from single cells, surface modification of the OET device is required to define large (0.5 mm) growth patches in which to confine cells. Random seeding onto large growth patches will result in low numbers of patches being loaded with single cells, which is inefficient when sample size per chip is low. The OET platform is attractive for mammalian single-cell colony formation because it is a versatile, reconfigurable manipulation platform for the selection and positioning of single cells into growth patches.

6.3.1 OET Surface Modification Method

The basic concept for adherent cell confinement on the OET substrate involves surface modification to define discrete growth patches on the device surface. Illustrated in Fig. 6.2, the growth patches with extracellular matrix (ECM) are modified to provide binding sites for cell adhesion, i.e., these areas are very "sticky" to cells. Outside of the growth patches, surface coating of polyethylene glycol (PEG) ensures that the surface is repellant to cells. PEG has been proven to both facilitate cell movement on surfaces and inhibit cell adhesion during cell culture [90]. OET is then used to select cells and then transport one and only one cell to each growth patch, where the cell will then adhere and proliferate into a colony within the growth patch.

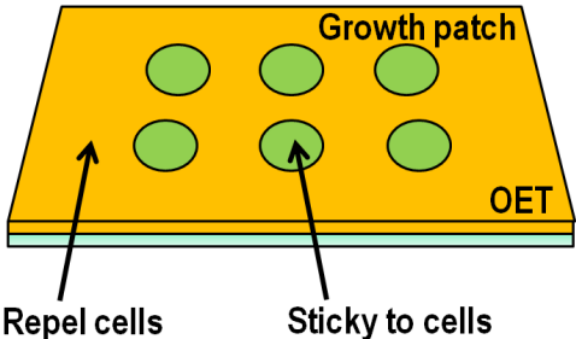

Fig. 6.2 Surface modification to define discrete growth patches on the OET surface. The round growth patches are large (0.5 mm in diameter) and covalently bonded with ECM. PEG is covalently grafted outside of the growth patches to repel cells. OET will select and transport one and only one cell into each growth patch. The positioned single cells will grow into colonal colonies.

6.3.2 OET Surface Modification Fabrication

For the aforementioned application, the OET substrate surface is subjected to many forces: voltages, electric fields, washes, and fluidic exchanges. For consistent performance, surface coating (ECM and PEG) adhesion strength must be strong and stable; therefore, covalent bonding of both PEG and ECM is necessary. In order to satisfy this need, we aimed to functionalize the OET surface with sulfo-SANPAH crosslinked ECM within growth patches, and silanized PEG outside of the growth patches.

Starting from the basic OET device presented in Fig. 6.1, subsequent surface modification processes are shown in Fig. 6.3. Silane-functionalized polyethylene glycol (PEG) is grafted onto the surface of the chip outside of the growth patches, modified from method from Lau et al. [90] and detailed in Appendix D. A 2 μm-thick g-line positive photoresist is spun onto the surface, followed by a 1-minute soft bake. A 10 × 10 array of 0.5-mm-diameter openings is formed in the photoresist by photolithography. The PEG layer in the exposed regions is removed by CF_4-oxygen plasma, which also etches approximately 100 nm of a-Si:H. Extracellular matrix is deposited within the patches by covalently binding collagen I to the substrate through sulfo-SANPAH, a crosslinker [91]. The sulfo-SANPAH crosslinker binds to the substrate and reacts with the amine group of collagen I to covalently coat the device surface with ECM for cell adhesion and culture within the patches. The photoresist layer is subsequently removed by a PRS-3000 photoresist remover at room temperature. See Appendix D for step-by-step details of the surface modification protocol.

The masking layer used for this fabrication process is a g-line photoresist, also explored by Shah et al. [92]. Photoresist is chosen for two reasons: (1) it adheres perfectly to the surface and is easily removed by a stripper, and (2) it forms very reproducible lithographic patterns. We also researched the alternative of a PDMS mask, similar to the method proposed by Jeon et al. [93], but it proved to be less optimal for our application and less consistently reproducible in quality. PDMS masks were prone to shape distortion and did not adhere perfectly to the surface, allowing etchant gases to attack the PEG-silane in unintended areas.

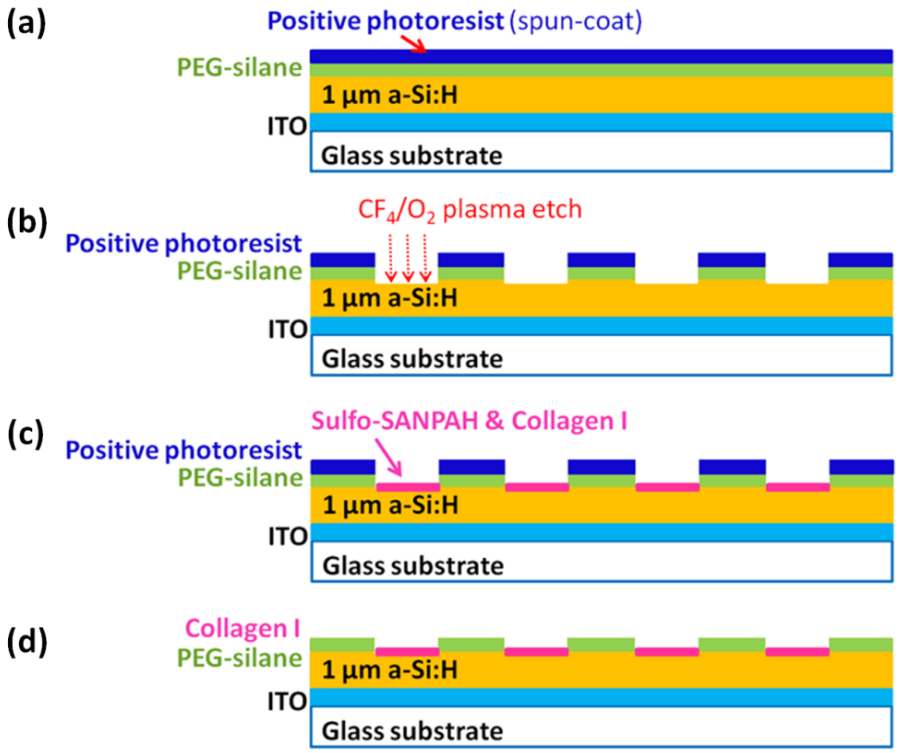

Fig. 6.3 Surface modification of OET: (a) OET surface is functionalized with PEG-silane. Photoresist is then spun coat onto the device surface; (b) photolithography and CF_4-oxygen plasma to remove PEG-silane and 100 nm of a-Si:H in growth patches (500µm diameter); (c) extracellular matrix (ECM) and sulfo-SANPAH in solution is then deposited on the growth patches, the ECM (collagen I) will then adsorb and covalently bind to the growth patches; and (d) removal of the photoresist by PRS 3000 resist stripper.

6.3.3 OET Surface Modification Characterization

A fabricated 10 × 10 patch array on the OET device surface is shown in Fig. 6.4. For visualization purposes, all the a-Si:H within growth patches were etched away using CF_4-oxygen plasma. Collagen I was labeled with anti-collagen I and Alexa Fluor 488 (GFP) immunostaining (protocol in Appendix D) to show its selective conjugation within the growth patches. Note that collagen I is strongly bonded to regions within the growth patches. Immunostaining of growth patches in a typical device, with only 100nm of a-Si:H etched away by CF_4-oxygen plasma, shows similarly selective and stable ECM deposition.

PEG characterization was performed using B16F10 mouse melanoma cells. A very high density (> 5×10^6 cells/ml) of B16F10 cells were loaded onto an OET device with surface silanized PEG. A similar density of B16F10 cells was also loaded onto a control OET device with no surface functionalization (bare a-Si:H and native oxide surface). The medium containing the cell suspension was a low-conductivity (10 mS/m) medium (Cytoporation Medium T). Placed in an incubator for one hour, the cells were allowed to adhere to the modified and unmodified device surfaces at 37°C. After an hour, the surfaces were rinsed three times with the same medium. Presented in Fig. 6.5(a), note that the OET device surface modified with PEG effectively inhibits the adhesion of cells, while in the control experiment [Fig. 6.5(b)], significant adhesion of cells occurred.

A fabricated device, with ECM within growth patches and PEG outside of the patches, was also seeded with a high density (> 5×10^6 cells/ml) of B16F10 cells in the low-conductivity medium and placed in an incubator for three hours before the surface was rinsed with PBS buffer three times. The medium was then changed to a standard cell culture medium (Dulbecco's Modified Eagle Medium with 10% Fetal Bovine Serum and 1% Penicillin and Streptomycin), and the top cover of the device was removed.

The cells were allowed to adhere and proliferate for 24 hours. Shown in Fig. 6.6, note that cells did not adhere or grow outside of the growth patches, but within the growth patches, cells adhered and proliferated very well.

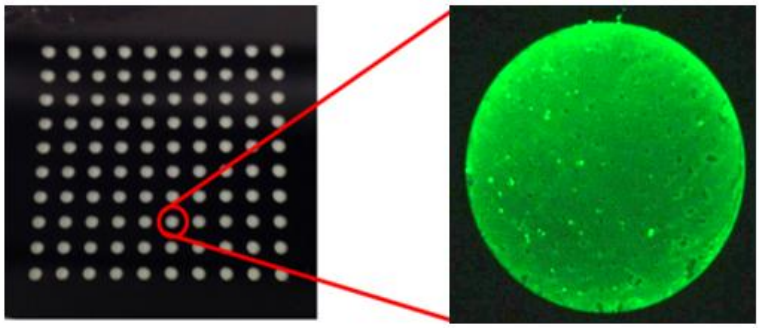

Fig. 6.4 10 ×10 array of ECM-coated patches on OET device surface. Selective ECM deposition within the patches was confirmed with anti-collagen I and- Alexa Fluor 488 (GFP) immunostaining. Sulfo-SANPAH crosslinker binds to the substrate and reacts with the amine group of collagen I to covalently coat the device surface with ECM for cell adhesion and culture within the patches.

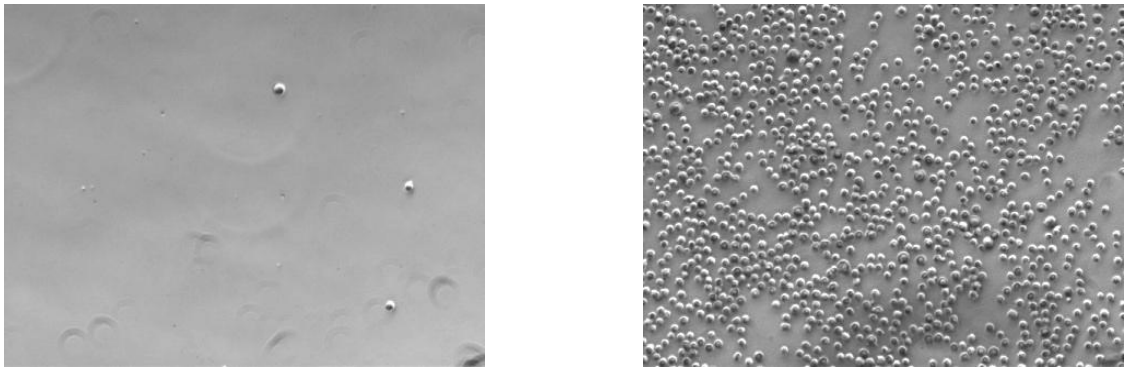

(a) **(b)**

Fig. 6.5 (a) Cell adhesion to OET surface with silanized PEG. After one hour attachment and rinsing, 0-3 cells have adhered per field of view (B16F10 mouse melanoma); (b) Control experiment—Cell adhesion to OET surface with no functionalization (a-Si:H and native oxide). After one hour attachment and washing, 738-1102 cells have adhered per field of view (B16F10 mouse melanoma).

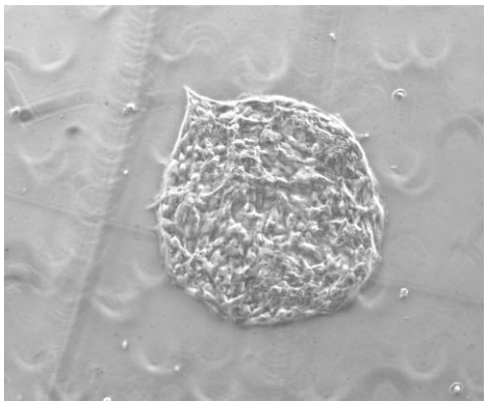

Fig. 6.6 Cells adhere, spread, and proliferate very densely within s growth patch containing ECM (0.5 mm diameter) but not to outside of the growth patch modified with PEG-silane. The cells were allowed to adhere and proliferate for 24 hours in standard cell culture medium. Growth patch is 0.5 mm in diameter.

6.4 Single-Cell Colony Formation using OET Platform

With the OET surface covalently functionalized with ECM and PEG, the OET device was then used to transport single cells onto the growth patches and expand these single cells into colonal colonies.

6.4.1 Single-Cell Positioning and Medium Exchange

For single-cell manipulation, OET was used to sort cells with desired attributes and position them onto the growth patches. Figure 6.7 illustrates the steps of this method. First, cells were seeded into the device fluidic chamber in a low-conductivity medium. Voltage was applied at 10 V_{ppk} and 100 kHz, which is below electroporation voltage as confirmed by Valley et al. [94] and by experimental live-dead assay with B16F10 cells. Light patterns formed virtual electrodes on the device surface and transported a single cell into each growth patch. If random seeding resulted in more than two cells already loaded into a growth patch, OET was used to move cells out of the patch such that only a single cell was left. The arranged cells were then placed in an incubator at 37°C for three hours to allow them to adhere to the growth patches. After the cells adhered, the low-conductivity medium was switched to a standard cell culture medium via perfusion. The top cover was then removed, and the substrate was placed in a petri dish filled with cell culture medium and cultured in an incubator at 37°C.

Figure 6.8 demonstrates the transport of a B16F10 mouse melanoma cell (in low-conductivity medium) using a light pattern. The cell is manipulated by light-induced positive dielectrophesis into a growth patch, where it is isolated. The single B16F10 cells adhere to the growth patches within three hours, and the fluid within the chamber is exchanged for cell culture medium. Extra cells on the PEG surface outside of the patches are purged away during the medium exchange.

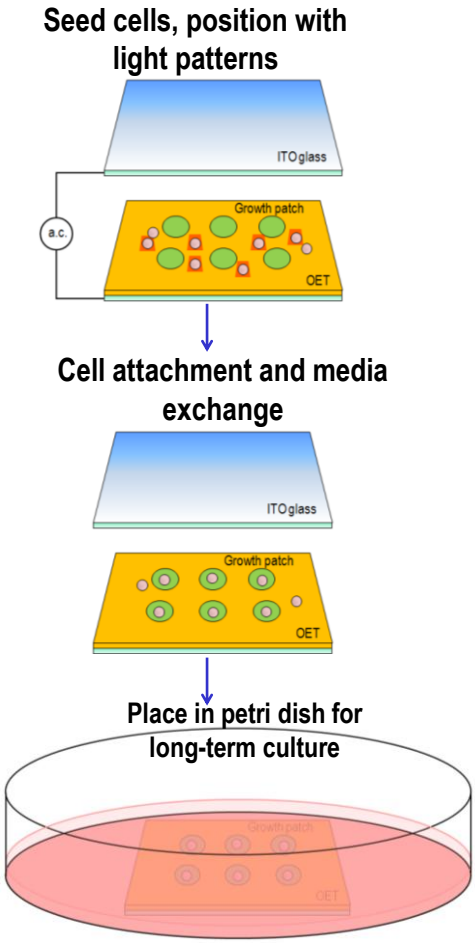

Fig. 6.7 Procedure for positioning a single cell on each growth patch. First, cells were seeded into the device fluidic chamber in low-conductivity medium. Light patterns formed virtual electrodes on the device surface and transported a single cell into each growth patch. If there were more than two cells already loaded into a growth patch, OET was used to move cells out of the patch such that only a single cell was left. Cells were then placed in an incubator at 37°C for three hours to adhere to the growth patches. After the cells adhered, the low-conductivity medium was switched to cell culture medium via perfusion. The top cover was then removed, and the substrate was placed in a petri dish with cell culture medium and cultured in an incubator at 37°C.

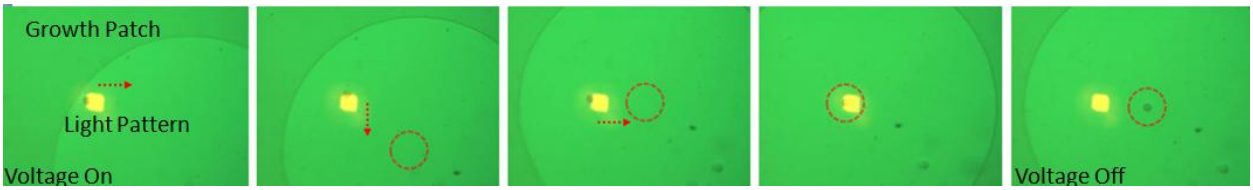

Fig. 6.8 Manipulation and positioning of a single cell via OET. A B16F10 melanoma cell was transported using a light pattern (light-induced dielectrophoresis) into a growth patch (large outer circle). The arrows indicate the movement of the light pattern. The red circle indicates the reference spot of the final cell position on the patch.

6.4.2 Single-Cell Positioning Efficiency

Efficiency of single-cell positioning over the 10 × 10 array on the device surface was characterized and shown in Fig. 6.9. Cells were seeded at a concentration of 5×10^4 cells/ml, which formed a random distribution of cells within growth patches (see the blue bars in Fig. 6.8). OET was then used to transport a cell into each empty growth patch, or transport all but one cell out of any growth patches containing two or more cells. As a result, 96 patches were loaded with single cells (the red bar), representing an enhancement of single-cell positioning by over five-fold.

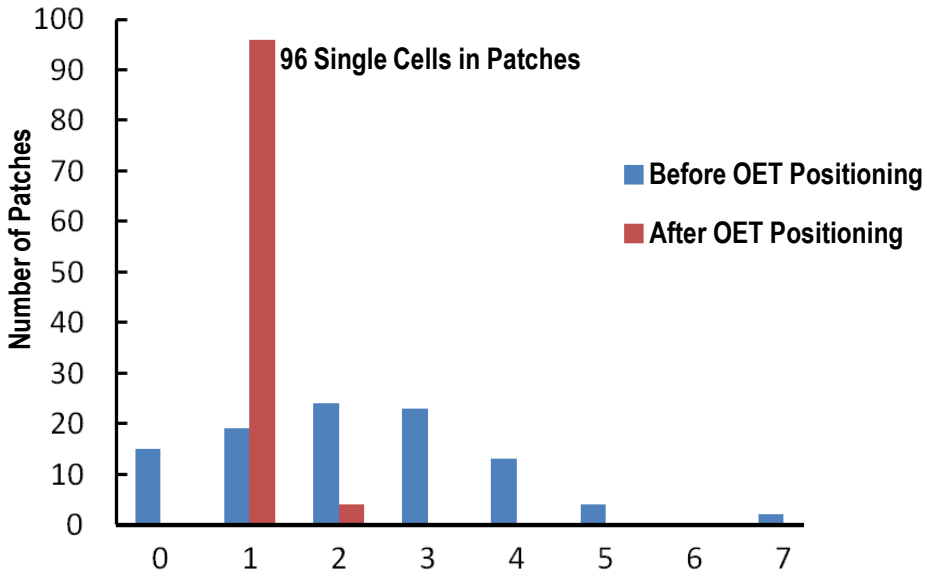

Fig. 6.9 When cells were seeded at a density of 5×10^4 cells/ml onto the device surface, a random distribution of cell numbers were formed in the growth patches, shown as the blue bars. OET was used to manipulate single cells into empty growth patches and manipulate cells out of patches containing multiple cells such that only one cell was left within each growth patch. A single-cell positioning efficiency of five-fold improvement is shown using OET versus passive seeding techniques.

6.4.3 Single-Cell Colony Formation

Patterned single cells were placed in an incubator (37°C, 5% CO_2) and observed for an extended period of time in a standard cell culture medium. Figure 6.10 shows a long-term proliferation study of single B16F10 cells cultured on growth patches. The single cells proliferated to 4 and 7 cells after 1 day and after day 4, respectively, and finally to 31 and 35-cell colonies by day 7. Under similar growth conditions, the doubling rate of B16F10 cells on generic tissue culture dishes has been established as approximately 24.7 hours. Our experimental results are comparable to the doubling time found in previously published literature, proving that the OET device surface modification and positioning process do not adversely affect or change cell behavior. The large growth area allowed a single cell to expand to a clonal population over two weeks in culture.

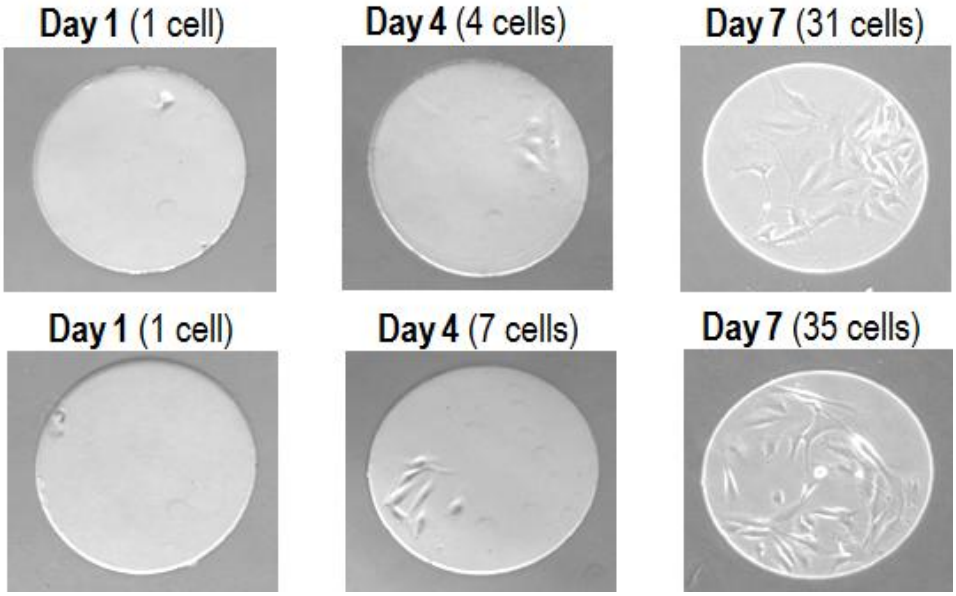

Fig. 6.10 B16F10 melanoma cell proliferation. A single B16F10 cell was positioned and cultured within a 500μm-diameter ECM patch. Isolated and well-contained proliferation of clonal colonies was tracked over the course of seven days.

6.5 Conclusion

This chapter presented an OET platform for the long-term culture of adherent, proliferative single cells. Surface modification and microfabrication techniques were used to create large growth patches on the OET device surface. We showed that cells could be sorted and transported to growth patches, where they adhere and proliferate. Long-term single-cell culture of B16F10 mouse melanoma cells has demonstrated the platform's efficacy. This platform offers a unique opportunity to study the heterogeneity of cells between different clonal colonies, thus elucidating the distinct roles of cellular subpopulations and providing quantitative answers to questions such as the rate of proliferation and other differences in cell behavior.

Chapter 7 Optoelectrowetting and Optoelectronic Tweezers Integration

7.1 Introduction

Digital microfluidics has received much attention over the past decade for their promise to improve both cost and performance of many fields ranging from pharmaceutical development to bio-defense. Traditional EWOD-based digital microfluidic devices use electrically addressable arrays of electrodes to transport droplets [17, 18]. Previously, we have reported microfluidic devices based on optoelectrowetting (OEW), which replaces the lithographically defined electrodes with a continuous film of photoconductor [50]. By translating optical patterns over the surface of the device, "virtual electrodes" are created to enable droplet manipulation. With this methodology, real-time, parallel droplet control can occur without the need for complex electrical addressing schemes. While digital microfluidics provides the ability to manipulate individual droplets, it does not provide a means to manipulate objects within the droplet itself. This is useful for selective sample concentration and single-cell sorting and encapsulation. Our group [95], and other groups [96, 97] have demonstrated the integration of traditional digital microfluidics with dielectrophoresis (DEP) manipulation technique, however, these devices' fabrication and operation are quite complicated.

This chapter present the ability to use the OEW device to perform the light-induced manipulation of both individual droplets (using OEW force) and particles within the droplet (using DEP force), switching between the two modalities involve only a simple change in device bias. This technique requires no lithography since electrodes are created using patterned light. Furthermore, since patterned light acts to define the electrodes, particle/droplet manipulation can occur anywhere on the surface of the device and full two-dimensional single particle control is achieved.

7.2 OEW-OET Integration Theory

The fabrication and operation of an OEW device was treated in depth in Chapter 2 and is shown conceptually in Fig. 7.1(a). Now, for OEW devices operating above a certain critical frequency, the insulating dielectric and Teflon layers act as electrical short circuits, and the bias now drops primarily across the liquid/droplet layer. Due to the spatial localization of the light pattern, electric field gradients are created near the edges of the light pattern. This results in a dielectrophoretic (DEP) force on particles within the droplet [Fig. 7.1(b)]. At these frequencies, the device looks electrically identical to our previously reported Optoelectronic Tweezers (OET) device in Chapter

6 [30]. So, by operating in this regime, particles within the droplet can be manipulated by simply altering the location of the incident optical patterns. Note that there will also be a DEP force on the droplet itself. However, this force is typically much weaker than the electrowetting force experienced at lower frequencies. Furthermore, if the light pattern does not illuminate the droplet contact line, no electrowetting force will be imparted to move the droplet.

The critical frequency at which one is able to transition from droplet manipulation to the manipulation of particles within the droplet is governed by the dimensions of the device itself (namely, the impedances of the liquid, photoconductor, and dielectric). In the case of the device presented here, that frequency is around 100 kHz; see Fig. 7.2(a). In this figure, the normalized electrowetting and DEP forces are calculated for typical device, droplet, and particle dimensions. One can see that the electrowetting effect peaks around 10 kHz, whereas DEP peaks at around 100 kHz, indicating two distinct operating regimes. Therefore, by switching above and below this critical frequency, either droplet or particle manipulation can occur.

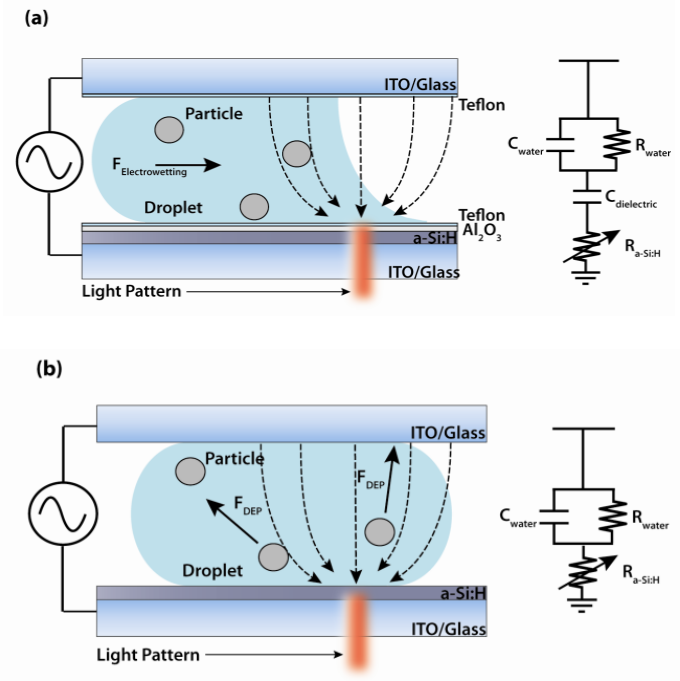

Fig. 7.1 Device schematic. (a) diagram of OEW device operating in electrowetting modality (valid for frequencies, f < 100 kHz). Incident light interacts with photoconductive a-Si:H layer and locally concentrates electric field across a thin Al_2O_3 dielectric layer. This causes aqueous droplets in the vicinity to move towards the light pattern. Particles within the droplet are transported along with the droplet; and (b) diagram of OEW device operating in DEP modality (f > 100kHz). In this modality, the electrically insulating Al_2O_3 and Teflon layers are shorted out, and the field is now concentrated in the liquid/droplet layer. Therefore, particles within the droplet experience a DEP force when in the vicinity of incident optical energy. In this regime, the OEW device electrically looks identical to Optoelectronic Tweezers.

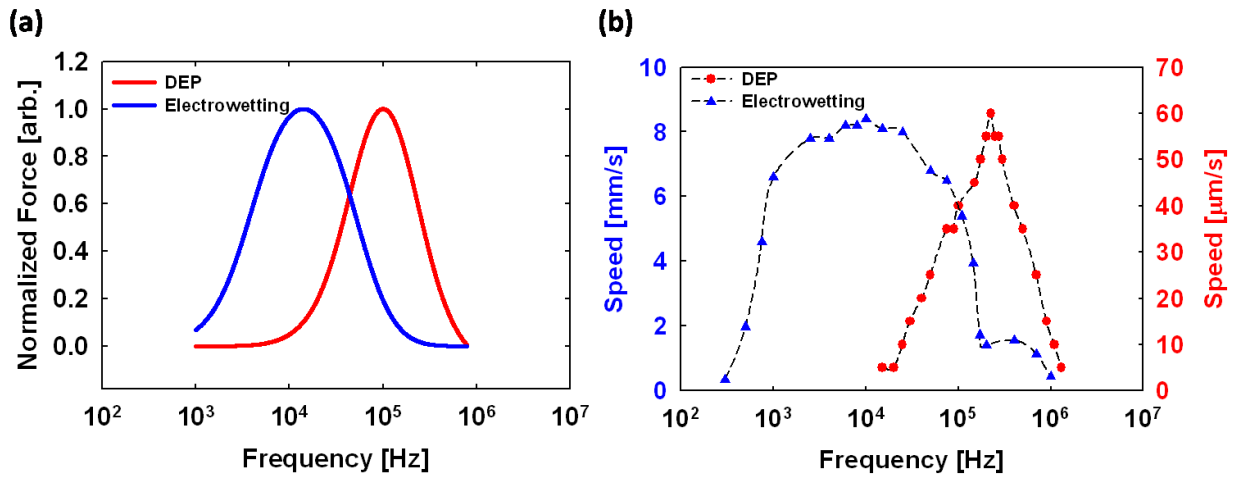

Fig. 7.2 Frequency response. (a) theoretical frequency response of the normalized electrowetting force (blue) acting on a droplet and the OET based DEP force (red) acting on an insulating bead within the droplet. Electrowetting force is maximized at around 10 kHz and DEP actuation is maximized at around 200 kHz; and (b) experimental data showing speed (which is proportional to force) of a 12.5 nl droplet (blue, 40 Vppk) and speed of a 10 μm polystyrene bead (red, 10 Vppk). The droplet movement is maximized at 10 kHz due to electrowetting, though a secondary hump is present at 200 kHz due to DEP enhancement of droplet movement. Bead speed is maximized at 200 kHz due to DEP. Results agree well with theory.

7.3 Experimental Method

The OEW device is depicted in Fig. 7.1(a). The fabrication and operation of an OEW device was treated in depth in Section 2.4.1. Devices used in this chapter were fabricated with 1 μm-thick photoconductive a-Si:H layer and 100 nm ALD Al_2O_3 dielectric layer. The fluidic manipulation chamber was formed by double-sided tape (100–300 μm). Device bias was applied between the two ITO layers (10–40 Vppk, 1–500 kHz).

Optical patterns were generated by a commercial data projector (Dell 4210X), controlled by an external computer, and focused onto the OEW device using a 1:1 telescope. Viewing occurred through a 5× objective connected to a CCD camera (Sony XCD-X710CR). Speed measurements for the polystyrene beads were extracted using a motorized stage controller (Newport ESP300). Samples were prepared by suspending 10 μm polystyrene beads (Polysciences Inc.) in a 10 mS/m aqueous solution along with 0.2% Pluronic F-68 surfactant (Sigma Aldrich). Droplets of the polystyrene mixture were then deposited in the OEW device and surrounded by silicone oil (1.0 cSt Trimethylsiloxy-terminated Polydimethylsiloxane, Gelest Inc).

7.4 Results and Discussion

7.4.1 Experimental Speed and Frequency Verification of Theory

While Fig. 7.2(a) shows the theoretical frequency response of both the electrowetting and DEP modalities, Fig. 7.2(b) shows the corresponding experimental frequency response. The agreement is quite good between the two, with EW dominating at 10 kHz and DEP at 200 kHz. An interesting aspect of Fig. 2b is the secondary peak seen in the EW response at higher frequencies.

The peak occurs at the same frequency as the DEP peak (200 kHz), indicating a DEP enhancement (in addition to electrowetting) of droplet movement. This indicates that both electrowetting and DEP are simultaneously occurring to enact droplet movement. Therefore, when manipulating particles with DEP within the droplet, care must be taken not to move the droplet itself. This is easily achieved by operating at low actuation voltages and using light patterns that are small relative to the overall size of the droplet.

7.4.2 Particle Concentration

One potential application of having an integrated platform for droplet and particle manipulation is the ability to perform on-chip sample concentration/purification. This process is depicted in Fig. 7.3(a). Here, particles are concentrated towards one end of the droplet using OET. Next, the droplet is split using OEW into two droplets, one containing the concentrated particles while the other remains empty. In this manner, the concentration/purity is effectively doubled.

Figure 7.3(b)-(i) shows video frames of this process. Fluorescent polystyrene beads were suspended in a 335 nl, 10 mS/m aqueous buffer. A light pattern was then swept across the droplet at 16 Vppk, 200 kHz and the beads were pushed (via negative DEP) towards the bottom of the droplet. Next, two light patterns were positioned at the top and bottom of the droplet, and a 32 Vppk, 10 kHz bias was applied. This causes the droplet to split into two, resulting in a concentrated droplet [Fig. 7.3(h)] and a diluted droplet [Fig. 7.3(i)]. For this demonstration, 93% of the beads were encapsulated in the concentrated droplet and the remaining 7% remained in the diluted droplet. For serial concentration and serial dilution, these steps can be performed again on the concentrated droplet or diluted droplet.

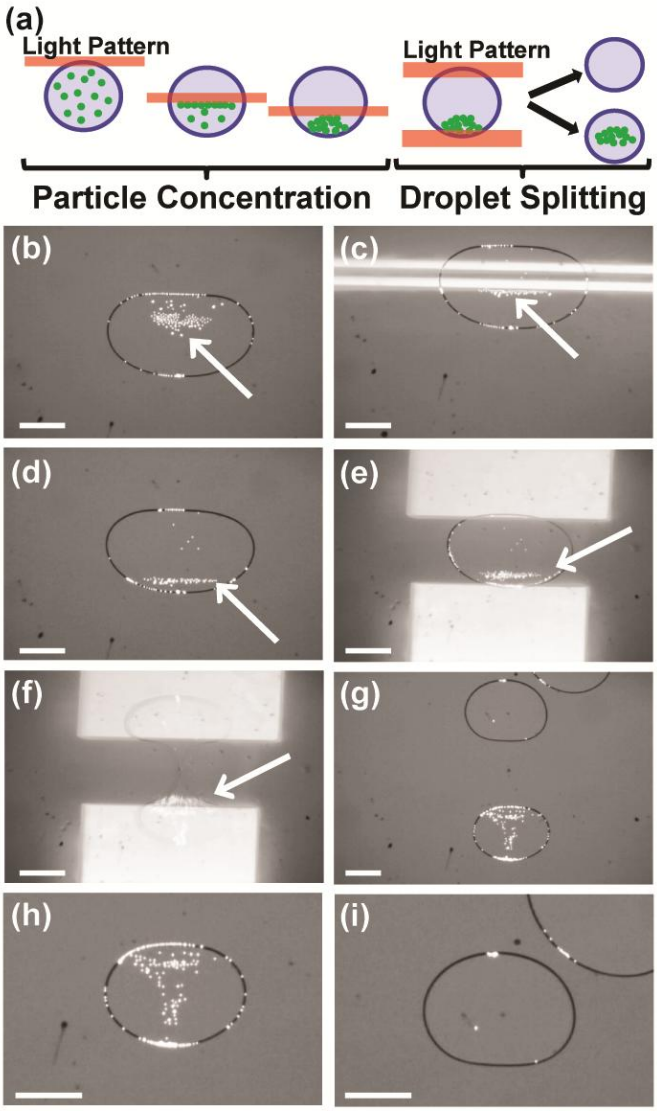

Fig. 7.3 (a) Method of particle concentration; (b)-(i) experimental demonstration of particle concentration. A 335 nl droplet containing fluorescent polystyrene beads (white arrow) is placed in the device (b). A light pattern (double bars) is swept across the device (c) (16 Vppk, 200 kHz), which push beads to one end of the droplet (d). Next the droplet is split (e)-(g) using OEW (32 Vppk, 10 kHz), resulting in a concentrated (h) and diluted (i) droplet. Scale bar = 750 μm.

7.4.3 Single-Cell Selection and Encapsulation

The ability to encapsulate single cells in micro-scale droplets is of great interest for single-cell analysis and/or sorting. Traditionally, this process relies on a statistical approach that ensures that some percentage of generated droplets contain single cells and does not afford the ability to select individual cells from a population for encapsulation [16, 9]. Although techniques using optical tweezers have achieved the ability to encapsulate individual cells selectively [98], the large optical power necessitated by optical tweezers is often detrimental to living structures [99]. The technique presented here requires several orders of magnitude less optical power.

Figure 7.4 demonstrates the ability to select an individual HeLa cell from a cohort and then encapsulate it. The process is depicted in Fig. 7.4(b)-(g), where an individual HeLa cell is selected from a group of three. The selected cell is moved via OET (16 Vppk, 10 kHz) to one end of the droplet, while the other two cells are moved towards the other end of the droplet. Then the droplet is split using OEW (32 Vppk, 200 kHz), resulting in one 75 nl droplet containing the selected cell [Fig. 7.4(f)] and the other 75 nl droplet containing the remaining two cells [Fig. 7.4(g)]. This demonstrates the ability to select and encapsulate single particles.

Once again, this would be very difficult to implement with non-optically-based techniques (i.e., microelectrode-based), as a large number of individually addressed electrodes would be necessary to ensure single particle control.

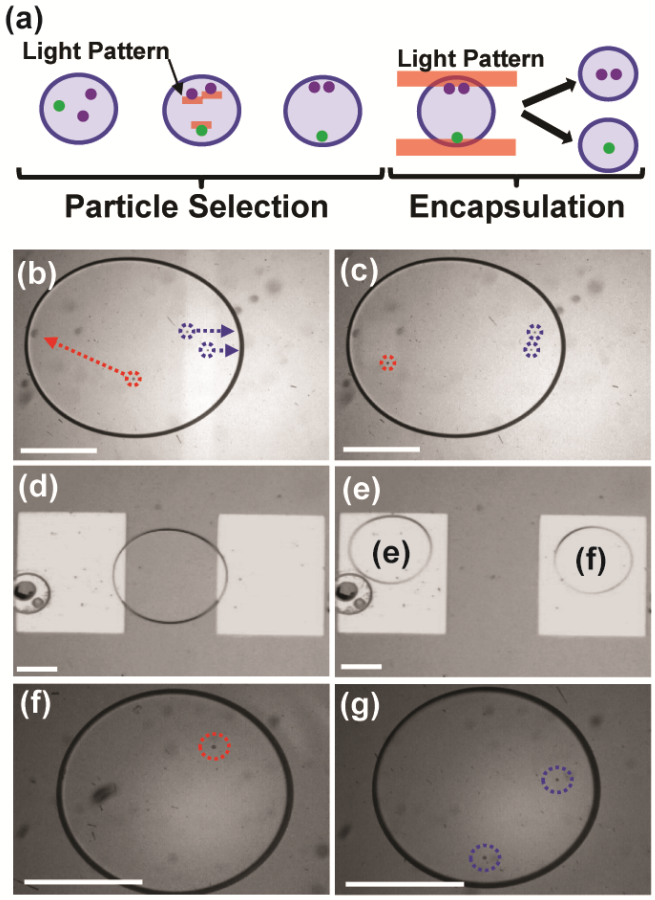

Fig. 7.4 (a) Method of single-cell selection and encapsulation; (b)-(c) A group of three HeLa cells exists within a 150 nl droplet. One cell is selected (red) and moved towards one side of the droplet while the other two (blue) are moved towards the opposite side (16 Vppk, 200 kHz); (d)-(e) next, the droplet is split with OEW into two 75 nl droplets (36 Vppk, 10kHz); (f) the resulting droplets contain the cell of interest; and (g) the remaining two cells. Scale bar = 500 μm.

7.5 Conclusion

This chapter introduced an integrated platform for on-chip particle and droplet manipulation. The technique uses OEW and OET as the manipulation modalities. Switching between droplet and particle manipulation is achieved through a change in the externally applied electrical frequency. The device allows for the continuous manipulation of both droplets and particles over its surface Finally, the use of light to pattern the electrodes enables full two-dimensional single-particle control. Concentration of particles and encapsulation of mammalian cells in a droplet has been achieved using this integrated technique. The development of a device that allows for a seamless integration of both droplet and particle manipulation that is simultaneously low-cost, high-resolution, and reconfigurable may one day form a foundation for a multitude of applications in both biology and chemistry.

Chapter 8 Conclusion

The abilities of our optofluidic platforms - optoelectrowetting (OEW) and optoelectronic tweezers (OET), and their integration have been presented in this thesis. For both devices, light from commercially available projectors were able to create "virtual electrodes" to move droplets in OEW and cells in OET for various demonstrations and applications.

In OEW, we have developed a distributed circuit model of the photoconductor that allowed us to optimize OEW structures for actuation with digital projectors. This enables simultaneous control of a large number of droplets over a large area (~ cm x cm). We have demonstrated 96 droplet array with droplet volume of 220 nl over 1.6 cm x 1 cm. Various digital microfluidic functions, such as droplet dispensing from reservoir or Teflon tubes, droplet splitting and merging, droplet motion with crescent electrodes, and droplet cutting using an integrated hydrophobic blade were demonstrated. Consequently, OEW is equipped with all the necessary tools to make OEW droplets discretely operable micro-reactors. Combining these functions, we have demonstrated an OEW optofluidic platform for detection of Herpes Simplex Virus Type 1 using real-time isothermal polymerase chain reactions in 16 parallel droplets. Surfactant was loaded into droplets to prevent protein surface fouling. Experiments confirmed that there was no DNA cross contamination.

In addition, a single-sided OEW device was conceptualized and demonstrated. Instead of a conductive top over the surface, a metal mesh ground is integrated on the device surface. This enabled droplets to be actuated freely on just one device surface, which has many interesting applications when integrated with packaging and fluidic input/output.

In OET, an application in long-term culture of adherent mammalian cells was explored. The main effort was to position single cells on 10 × 10 array of large (0.5 mm diameter) growth patches where cells can adhere and proliferate. The large growth patches allowed the single cells to expand to a colonal population over two weeks. This was achieved by device surface functionalization where extracellular matrices were covalently bonded to growth patches to promote cell adhesion and silanization of polyethylene glycol outside of growth patches was developed to inhibit cell adhesion.

Finally, although the two aforementioned optofluidic devices utilize different physical forces, their device structures are somewhat similar. Hence, by altering the frequencies, we are able to switch from OET (high-frequency 100 kHz) to OEW (low-frequency 10 kHz) in the same physical device. Applications such as particle concentration and single cell encapsulation were successfully demonstrated.

The research presented in this thesis demonstrates the potential of the OEW and OET platforms for implementing various optofluidic lab-on-chips functionalities and applications. Light actuation decouples the microfluidic device from the control circuits and systems. When

combined with a digital projector, the OEW/OET devices are transformed into million pixel optofluidic systems that can handle a large number of cells and/or droplets. Together, they offered a powerful platform that can potentially bring Moore's law to biological assays.

Bibliography

[1] "Special Report: 50 Years of Moore's Law," IEEE Spectrum, 2015. [Online]. Available: http://spectrum.ieee.org/static/special-report-50-years-of-moores-law.

[2] C. Humphries, "A Moore's Law for Genetics," MIT Technology Review, 2010. [Online]. Available: http://www.technologyreview.com/article/417628/a-moores-law-for-genetics/.

[3] G. M. Whitesides, "The origins and the future of microfluidics," *Nature,* vol. 442, pp. 368-373, 2006.

[4] T. U. Daim and P. Suntharasaj, "Technology Roadmap: Lab-on-a-Chip," *Rev. Adm. UFSM, Santa Maria,* vol. 3, no. 1, pp. 160-173, 2010.

[5] A. Manz, N. Graber and H. Widmer, "Miniaturized total chemical analysis systems: A novel concept for chemical sensing," *Sensors and Actuators B: Chemical,* vol. 1, no. 1-6, pp. 244-248, 1990.

[6] T. Thorsen, S. J. Maerkl and S. R. Quake, "Microfuidic large-scale integration," *Science,* vol. 298, no. 5593, pp. 580-584, 2002.

[7] H. Song, D. L. Chen and R. F. Ismagilov, "Reactions in Droplets in Microfluidic Channels," *Angewandte Chemie ,* vol. 45, no. 44, pp. 7336-7356, 2006.

[8] L. Mazutis, J. Gilbert, W. L. Ung, D. A. Weitz, A. D. Griffiths and J. A. Heyman, "Single-cell analysis and sorting using droplet-based microfluidics," *Nat. Prot.,* vol. 8, p. 870–891, 2013.

[9] S. Koster, F. E. Angile, H. Duan, J. J. Agresti, A. Wintner, C. Schmitz, A. C. Rowat, C. A. Merten, D. Pisignano, A. D. Griffiths and D. A. Weitz, "Drop-based microfluidic devices for encapsulation of single cells," *Lab Chip,* vol. 8, pp. 1110-1115, 2008.

[10] N. A. Mousa, M. J. Jebrail, H. Yang, M. Abdelgawad, P. Metalnikov, J. Chen, A. R. Wheeler and R. F. Casper, "Droplet-Scale Estrogen Assays in Breast Tissue, Blood, and Serum," *Sci. Transl. Med.,* vol. 1, no. 1, p. 1ra2, 2009.

[11] A. Wixforth, C. Strobl, C. Gauer, A. Toegl, J. Scriba and Z. v. Guttenberg, "Acoustic manipulation of small droplets," *Analytical and Bioanalytical Chemistry,* vol. 379, no. 7-8, pp. 982-991, 2004.

[12] D. D. Carlo, L. Y. Wu and L. P. Lee, "Dynamic single cell culture array," *Lab Chip,* vol. 6, pp. 1445-1449, 2006.

[13] D. Psaltis, S. R. Quake and C. Yang, "Developing optofluidic technology through the fusion of

microfluidics and optics," *Nature*, vol. 442, pp. 381-386, 2006.

[14] S. N. Pei, J. Valley, S. Neale, A. Jamshidi, H.-Y. Hsu and M. Wu, "Light-actuated digital microfluidics for large-scale, parallel manipulation of arbitrarily sized droplets," *Micro Electro Mechanical Systems (MEMS), 2010 IEEE 23rd International Conference on*, pp. 252-255, 2010.

[15] D. N. Adamson, D. Mustafi and J. X. Zhang, "Production of arrays of chemically distinct nanolitre plugs via repeated splitting in microfluidic devices," *Lab Chip*, vol. 6, p. 1178–1186, 2006.

[16] J. Clausell-Tormos, D. Lieber, J.-C. Baret, A. El-Harrak, O. J. Miller, L.Frenz, J. Blouwolff, K. J. Humphry, S. Köster, H. Duan, C. Holtze, D. Weitz, A. D. Griffiths and C. A. Merten, "Droplet-Based Microfluidic Platforms for the Encapsulation and Screening of Mammalian Cells and Multicellular Organisms," *Chem. & Biol.*, vol. 15, no. 5, p. 427–437, 2008.

[17] M. G. Pollack, R. B. Fair and A. D. Shenderov, "Electrowetting-based actuation of liquid droplets for microfluidic applications," *Appl. Phys. Lett.*, vol. 77, pp. 1725-1726, 2000.

[18] S. K. Cho, H. Moon and C.-J. Kim, "Creating, transporting, cutting, and merging liquid droplets by electrowetting-based actuation for digital microfluidic circuits," *J. Microelectromech. Syst.*, vol. 12, pp. 70-80, 2003.

[19] S. Teh, R. Lin, L. Hung and A. P. Lee, "Droplet microfluidics," *Lab Chip*, vol. 8, pp. 198-220, 2008.

[20] M. Abdelgawad and A. R. Wheeler, "The digital revolution: a new paradigm for microfluidics," *Adv. Mater.*, vol. 21, pp. 920-925, 2009.

[21] V. Srinivasan, V. K. Pamula and R. B. Fair, "Droplet-based microfluidic lab-on-a-chip for glucose detection," *Analytica Chimica Acta*, vol. 507, pp. 145-150, 2004.

[22] Z. Hua, J. L. Rouse, A. E. Eckhardt, V. Srinivasan, V. K. Pamula, W. Schell, J. L. Benton, T. G. Mitchell and M. G. Pollack, "Multiplexed real-time polymerase chain reaction on a digital microfluidic platform," *Anal. Chem.*, vol. 82, no. 6, pp. 2310-2316, 2010.

[23] Y. Chang, G.-B. Lee, F. Huang, Y. Chen and J. Lin, "Integrated polymerase chain reaction chips utilizing digital microfluidics," *Biomedical Microdevices*, vol. 8, pp. 215-225, 2006.

[24] A. R. Wheeler, H. Moon, C. A. Bird, R. R. Loo, C.-J. Kim, J. A. Loo and R. L. Garrell, "Digital microfluidics with in-line sample purification for proteomics analyses with MALDI-MS," *Anal. Chem.*, vol. 77, pp. 534-540, 2005.

[25] I. Barbulovic-Nad, S. Au and A. Wheeler, "A microfluidic platform for complete mammalian cell culture," *Lab Chip*, Vols. 1536-1542, p. 10, 2010.

[26] J. R. Millman, K. H. Bhatt, B. G. Prevo and O. D. Velev, "Anisotropic particle synthesis in dielectrophoretically controlled microdroplet reactors," *Nat. Mater.*, vol. 4, pp. 98-102, 2005.

[27] P. Y. Chiou, H. Moon, H. Toshiyoshi, C. J. Kim and M. C. Wu, "Light actuation of liquid by optoelectrowetting," *Sens. Actuat. A: Phys.,*, vol. 104, no. 3, pp. 222-228, 2003.

[28] P. Y. Chiou, Z. Chang and M. C. Wu, "Droplet manipulation with light on optoelectrowetting device," *J. Microelectromech. Syst.,* vol. 17, pp. 133-138, 2008.

[29] P. Y. Chiou, S.-. Y. Park and M. C. Wu, "Continuous optoelectrowetting for picoliter droplet manipulation," *Appl. Phys. Lett.,* vol. 93, pp. 221110-221113, 2008.

[30] P. Y. Chiou, A. T. Ohta and M. C. Wu, "Massively parallel manipulation of single cells and microparticles using optical images," *Nature,* vol. 436, pp. 370-372, 2005.

[31] A. T. Ohta, P.-Y. Chiou, T. H. Han, J. C. Liao, U. Bhardwaj, E. R. B.McCabe, R. S. F. Yu and M. C. Wu, "Dynamic Cell and Microparticle Control via Optoelectronic Tweezers," *J. Microelectromech. Sys.,* vol. 16, no. 3, pp. 491-499, 2007.

[32] S.-Y. Park, M. Teitell and P.-Y. Chiou, "Single-sided continuous optoelectrowetting (SCOEW) for droplet manipulation with light patterns," *Lab Chip,* vol. 10, pp. 1655- 1661, 2010.

[33] W.-Y. Lin, Y.-H. Lin and G.-B. Lee, "Separation of micro-particles utilizing spatial diffference of optically induced dielectrophoretic forces," *Microfluid. Nanofluid.,* vol. 8, pp. 217-229, 2000.

[34] W. Liang, S. Wang, Z. Dong, G.-B. Lee and W. J. Li, "Optical Spectrum and Electric Field Waveform Dependent Optically-Induced Dielectrophoretic Micro-Manipulation," *Micromach.,* vol. 3, pp. 492-508, 2012.

[35] F. Mugele and J.-C. Baret, "Electrowetting: from basics to applications," *Journal of Physics: Condensed Matter,* vol. 17, no. 28, p. R705, 2005.

[36] T. B. Jones, J. D. Fowler, Y. S. Chang and C. J. Kim, "Frequency-based relationship of electrowetting and dielectrophoretic liquid microactuation," *Langmuir,* vol. 19, pp. 7646-7651, 2003.

[37] F. M. Fowkes, "Attractive forces at interfaces," *Ind. Eng. Chem.,* vol. 56, no. 12, pp. 40-52, 1964.

[38] J. K. Valley, A. Jamshidi, A. T. Ohta, H.-. Y. Hsu and M. C. Wu, "Operational regimes and physics present in optoelectronic tweezers," *J. Microelectromech. Syst.,* vol. 17, pp. 342-350, 2008.

[39] H. Moon, S. K. Cho, R. L. Garrell and C. J. Kim, "Low voltage electrowetting-on-dielectric," *J. Appl. Phys.,* vol. 92, pp. 4080-4087, 2002.

[40] Y. Li, W. Parkes, L. Haworth, A. Stokes, K. Muir, P. Li, A.J.Collin, N. Hutcheon, R. Henderson, B. Rae and A. Walton, "Anodic Ta2O5 for CMOS compatible low voltage electrowetting-on-dielectric device fabrication," *Solid-State Electronics,* vol. 52, no. 9, pp. 1382-1387, 2008.

[41] J.-H. Chang, D. Choi, S. Han and J. Pak, "Driving characteristics of the electrowetting-on-dielectric device using atomic-layer-deposited aluminum oxide as the dielectric," *Microfluid. Nanofluid.,* vol. 8, pp. 269-273, 2010.

[42] H. Liu, S. Dharmatilleke, D. K. Maurya and A. A. O. Tay, "Dielectric materials for electrowetting-on-dielectric actuation," *Microsyst. Technol.,* vol. 16, p. 449–460, 2010.

[43] L. Kang, B. H. Lee, W.-J. Q. Y. Jeon, R. Nieh, S. Gopalan, K. Onishi and J. C. Lee, "Electrical Characteristics of Highly Reliable Ultrathin Hafnium Oxide Gate Dielectric," *IEEE Electron. Dev.*

Lett., vol. 21, no. 4, pp. 181-183, 2000.

[44] "Thin-film silicon solar cells," Delft University of Technology Open Course Ware, [Online]. Available: http://ocw.tudelft.nl/fileadmin/ocw/courses/SolarCells/res00030/CH7_Thin_film_Si_solar_cells.pdf.

[45] Y. Hishikawa, S. Tsuge, N. Nakamura, S. Tsuda, S. Nakano and Y.Yukinori, "Device-quality wide-gap hydrogenated amorphous silicon films deposited by plasma chemical vapor deposition at low substrate temperatures," *Jpn. J. Appl. Phys.*, vol. 69, pp. 508-510, 1991.

[46] V. Bahadur and S. V. Garimella, "An energy-based model for electrowetting-induced droplet actuation," *J. Micromech. Microeng.*, vol. 16, no. 8, p. 1494, 2006.

[47] B. S. Yoon, S. J. Yoo, J. E. Lee, S. You, H. T. Lee and H. S. Yoon, "Enhanced differentiation of human embryonic stem cells into cardiomyocytes by combining hanging drop culture and 5-azacytidine treatment," *Differentiation,* vol. 74, no. 4, pp. 149-159, 2006.

[48] U.-C. Yi and C.-J. Kim, "Characterization of electrowetting actuation on addressable single-side coplanar electrodes," *J. micromech Microeng.*, vol. 16, pp. 2053-2059, 2006.

[49] M. Abdelgawad, S. Freire, H. Yang and A. Wheeler, "All-terrain droplet actuation," *Lab Chip,* vol. 8, pp. 672-677, 2008.

[50] S. Pei, J. Valley, Y.-L. Wang and M. Wu, "Distributed Circuit Model for Multi-Color Light-Actuated Opto-Electrowetting Microfluidic," *J. Lightwave Devices,* vol. 33, no. 16, pp. 1-8, 2015.

[51] H.-S. Chuang, A. Kumar and S. T. Wereley, "Open optoelectrowetting droplet actuation," *Appl. Phys. Lett.*, vol. 93, p. 064104, 2008.

[52] R. B. Fair, A. Khlystov, V. Srinivasan, V. K. Pamula and K. N. Weaver, "Integrated chemical/biochemcal sample collection, pre-concentration, and analysis on a digital microfluidic lab-on-a-chip platform," *Proc. of SPIE,* p. 5591, 2004.

[53] G. Venezian, "On the resistance between two points on a grid," *Am. J. Phys.*, vol. 62, p. 1000, 1994.

[54] T. Squires and S. Quake, "Microfluidics: Fluid physics at the nanoliter scale," *Reviews of modern physics,* vol. 77, pp. 977-1026, 2005.

[55] P. Paik, V. Pamula and R. Fair, "Rapid droplet mixers for digital microfluidic systems," *Lab Chip,* vol. 3, p. 253, 2003.

[56] P. Paik, V. Pamula, M. Pollack and R. Fair, "Electrowetting-based droplet mixers for microfluidic systems," *Lab Chip,* vol. 3, pp. 28-33, 2003.

[57] J. Fowler, H. Moon and C. Kim, "“Enhancement of mixing by droplet-based microfluidics,”," *Micro Electro Mechanical Systems, 2002. The Fifteenth IEEE International Conference on,* pp. 97-80, 2002.

[58] F. Mugele, J.-C. Baret and D. Steinhauser, "Microfluidic mixing through electrowetting-induced

droplet oscillations," *Applied Physics Letters,* vol. 88, no. 20, p. 204106, 2006.

[59] P. García-Sánchez, A. Ramos and F. Mugele, "Electrothermally driven flows in ac electrowetting," *Phys. Rev. E,* vol. 81, p. 015303, 2010.

[60] H.-Y. Hsu, S. Vogler, A. Jamshidi, J. Valley, S. N. Pei, S. Pautot and M. Wu, "Thermo-sensitive microgels as in-situ sensor for temperature measurement in optoelectronic tweezers," *23rd IEEE International Conference on Micro Electro Mechanical Systems (MEMS),* pp. 1123-1126, 2010.

[61] J. Berthier, P. Clementz, O. Raccurt, D. Jary, P. Claustre, C. Peponnet and Y. Fouillet, "Computer aided design of an EWOD microdevice," *Sensors and Actuators A: Physical,* vol. 127, no. 2, p. 283–294, 2006.

[62] J. Gong and C. Kim, "All-electronic droplet generation on-chip with real-time feedback control for EWOD digital microfluidics," *Lab Chip,* vol. 8, pp. 898-906, 2008.

[63] H. Ren, R. Fair and M. Pollack, "Automated on-chip droplet dispensing with volume control by electro-wetting actuation and capacitance metering," *Sensors and Actuators B: Chemical,* vol. 98, no. 2-3, pp. 319-327, 2004.

[64] M. Kiss, L. Ortoleva-Donnelly, N. Beer, J. Warner, C. Bailey, B. Colston, J. Rothberg, D. Link and J. Leamon, "High- throughput quantitative polymerase chain reaction in picoliter droplets," *Anal. Chem.,* vol. 80, pp. 8975-8981, 2008.

[65] V. Myriam, Y. Xu and H. Kong, "Helicase-dependent isothermal DNA amplification," *EMBO reports,* vol. 5, no. 8, pp. 795-800, 2004.

[66] K. Yeung-Yue, M. Brentjens, P. Lee and S. Tyring, "Herpes simplex viruses 1 and 2," *Dermatol. Clin.,* vol. 20, p. 249–266, 2002.

[67] G. Crist, J. Langer, G. Woods, M. Procter and D. Hillyard, "Evaluation of the ELVIS plate method for the detection and typing of herpes simplex virus in clinical specimens," *Diagn. Microbiol. Infect. Dis.,* vol. 49, p. 173–177, 2004.

[68] H.-J. Kim, Y. Tong, W. Tang, L. Quimson, V. Cope, X. Pan, A. Motre, R. Kong, J. Hong, D. Kohn, N. Miller, M. Poulter, H. Kong, Y.-W. Tang and Y.-L. B., "A rapid and simple isothermal nucleic acid amplification test for detection of herpes simplex virus types 1 and 2," *J. Clini. Virolo.,* vol. 50, p. 26–30, 2011.

[69] Y. Tong, K. McCarthy, H. Kong and B. Lemieux, "Development and Comparison of a Rapid Isothermal Nucleic Acid Amplification Test for Typing of Herpes Simplex Virus Types 1 and 2 on a portable Fluorescence Detector," *J. Molec. Diagn.,* vol. 14, no. 6, pp. 569-576, 2012.

[70] D. B. Weibel and G. M. Whitesides, "Applications of microfluidics in chemical biology," *Current Opinion in Chemical Biology,* vol. 10, no. 6, p. 584–591, 2006.

[71] S. Choi and J. Chae, "Methods of reducing non-specific adsorption in microfluidic biosensors," *J. Micromech. Microeng.,* vol. 20, no. 7, p. 075015 , 2010.

[72] V. Luk, G. Mo and A. Wheeler, "Pluronic additives: a solution to sticky problems in digital microfluidics," *Langmuir,* vol. 24, no. 12, pp. 6382-6389, 2008.

[73] S. H. Au, P. Kumar and A. R. Wheeler, "A New Angle on Pluronic Additives: Advancing Droplets and Understanding in Digital Microfluidics," *Langmuir,* vol. 27, pp. 8586-8594, 2011.

[74] "IsoAmp® III Universal tHDA Kit," [Online]. Available: http://www.biohelix.com/pdf/H0120S_IsoAmp%20III_BH_eDatacard.pdf.

[75] S. Pei, J. Valley, S. Neale, H.-Y. Hsu, A. Jamshidi and M. Wu, "Rapid Droplet Mixing Using Light-Actuated Digital Microfluidics," *in Conference on Lasers and Electro-Optics,* p. CTuJJ2, 2010.

[76] D. D. Carlo and L. P. Lee, "Dynamic single-cell analysis for quantitative biology," *Anal. Chem.,* vol. 23, pp. 7918-7925, 2006.

[77] C. Chen, M. Mrksich, S. Huang, G. Whitesides and D. Ingber, "Micropatterned surfaces for control of cell shape, position, and function," *Biotech. Prog.,* vol. 14, no. 3, pp. 356-363, 1998.

[78] P. J. Hung, P. J. Lee, P. Sabounchi, R. Lin and L. P. Lee, "Continuous perfusion microfluidic cell culture array for high-throughput cell-based assays," *Biotechnology and Bioengineering,* vol. 89, no. 1, pp. 1-8, 2005.

[79] H. Kimura, T. Yamamoto, H. Sakai, Y. Sakaia and T. Fujii, "An integrated microfluidic system for long-term perfusion culture and on-line monitoring of intestinal tissue models," *Lab Chip,* vol. 8, pp. 741-746, 2008.

[80] R. Gómez-Sjöberg, A. A. Leyrat, D. M. Pirone, C. S. Chen and S. R. Quake, "Versatile, Fully Automated, Microfluidic Cell Culture System," *Anal. Chem.,* vol. 79, no. 22, p. 8557–8563, 2007.

[81] A. Ohta, P.-Y. Chiou, T. Han, J. Liao, U. Bhardwaj, E. McCabe, F. Yu, R. Sun and M. Wu, "Dynamic Cell and Microparticle Control via Optoelectronic Tweezers," *J. Microelectromech. Syst.,* vol. 16, no. 3, pp. 1057-7157, 2007.

[82] A. Jamshidi, P. J. Pauzauskie, P. J. Schuck, A. T. Ohta, P.-Y. Chiou, J. Chou, P. Yang and M. C. Wu, "Dynamic manipulation and separation of individual semiconducting and metallic nanowires," *Nature Photonics* , vol. 2, pp. 86-89, 2008.

[83] J. K. Valley, P. Swinton, W. J. Boscardin, T. F. Lue, P. F. Rinaudo, M. C. Wu and M. M. Garcia, "Preimplantation Mouse Embryo Selection Guided by Light-Induced Dielectrophoresis," *PLOS One,* vol. 5, no. 4, p. e10160, 2010.

[84] H. Hsu, A. Jamshidi, S. Shekarchian, W. Lam, J. Valley, S. Pei and M. Wu, "Open-access phototransistor-based optoelectronic tweezers for long-term single cell heterogeneity study," *Micro Electro Mechanical Systems (MEMS), 2011 IEEE 24th International Conference on,* pp. 63-66, 2011.

[85] H. A. Pohl, Dielectrophoresis: The Behavior of Neutral Matter in Nonuniform Electric Fields, Cambridge University Press , 1978.

[86] T. B. Jones, Electromechanics of Particles, Cambridge University Press, 1995.

[87] P. R. C. Gascoyne, F. F. Becker and X. B. Wang, "Numerical-analysis of the influence of experimental conditions on the accuracy of dielectric parameters derived from electrorotation measurements," *Bioelectrochemistry and Bioenergetics,* vol. 36, pp. 115-125, 1995.

[88] A. T. Ohta, M. Garcia, J. K. Valley, L. Banie, H.-Y. Hsu, A. Jamshidi, S. L. Neale, T. Lue and M. C. Wu, "Motile and non-motile sperm diagnostic manipulation using optoelectronic tweezers," *Lab Chip,* vol. 10, pp. 3213-3217, 2010.

[89] P. J. Pauzauskie, T. Laurence, B. Chromy, H.-Y. Hsu and M. Wu, "Parallel, Non-Contact Trapping and Translation of Yersenia Pestis Bacteria with Optoelectronic Tweezers," *Biophysical Journal,* vol. 98, no. 3, pp. 610a-611a, 2010.

[90] A. N. K. Lau, A. T. Ohta, H. L. Phan, H.-Y. Hsu, A. Jamshidi, P.-Y. Chiou and M. C. Wu, "Antifouling coat-ings for optoelectronic tweezers," *Lab Chip,* vol. 20, pp. 2952-2957, 2009.

[91] J. R. Tse and A. J. Engler, "Preparation of hydrogel substrates with tunable mechanical properties," *Curr. Protoc. Cell Biol.,* pp. 47:10.16.1-10.16.16., 2010.

[92] S. S. Shah, M. C. Howland, L.-J. Chen, J. Silangcruz, S. V. Verkhoturov, E. A. Schweikert, A. N. Parikh and A. Revzin, "Micropatterning of Proteins and Mammalian Cells on Indium Tin Oxide," *Applied Materials and Interfaces,* vol. 1, no. 11, p. 2592–2601, 2009.

[93] H. Jeon, R. Schmidt, J. E. Barton, D. J. Hwang, L. J. Gamble, D. G. Castner, C. P. Grigoropoulos and K. E. Healy, "Chemical Patterning of Ultrathin Polymer Films by Direct-Write Multiphoton Lithography," *J. of Am. Chem. Soc.,* vol. 133, p. 6138–6141, 2012.

[94] J. K. Valley, S. Neale, H.-Y. Hsu, A. T. Ohta, A. Jamshidi and M. C. Wu, "Parallel single-cell light-induced electroporation and dielectrophoretic manipulation," *Lab Chip,* vol. 9, pp. 1714-1720, 2009.

[95] G. J. Shah, A. T. Ohta, E. P. Y. Chiou, M. C. Wu and C.-J. Kim, "EWOD-driven droplet microfluidic device integrated with optoelectronic tweezers as an automated platform for cellular isolation and analysis," *Lab Chip,* vol. 9, pp. 1732-1739, 2009.

[96] S.-K. Fan, P.-W. Huang, T.-T. Wang and Y.-H. Peng, "Cross-scale electric manipulations of cells and droplets by frequency-modulated dielectrophoresis and electrowetting," *Lab Chip,* vol. 8, pp. 1325-1331, 2008.

[97] Y. Zhao, U.-C. Yi and S. K. Cho, "Microparticle concentration and separation by traveling-wave dielectrophoresis (twDEP) for digital microfluidics," *Journal of Microelectromechanical Systems,* vol. 16, pp. 1472-1481, 2007.

[98] M. He, J. S. Edgar, G. D. M. Jeffries, R. M. Lorenz, J. P. Shelby and D. T. Chiu, "Selective Encapsulation of Single Cells and Subcellular Organelles into Picoliter- and Femtoliter-Volume Droplets," *Analytical Chemistry,* vol. 77, pp. 1539-1544, 2005.

[99] K. C. Neuman, E. H. Chadd, G. F. Liou, K. Bergman and S. M. Block, "Characterization of

photodamage to escherichia coli in optical traps," *Biophysical Journal*, vol. 77, pp. 2856-2863, 1999.

Appendix A Optoelectrowetting (OEW) Device Fabrication

A.1. OEW Device Fabrication

1) ITO coated 6" glass wafers were acquired from Thin Film Devices Inc. (Anaheim, CA). Thicknesses of ITO deposited are 2800 ± 100Å, with resistivity 10 ± 2 ohms/sq. The glass substrate used was 0.7mm ± 0.1mm thick Corning Eagle XG glass.

2) On this substrate, on the ITO coated side, a 1-μm-thick photoconductive a-Si:H layer was deposited via plasma-enhanced chemical vapor deposition (PECVD) (Oxford Plasmalab 80plus) - The a-Si:H recipe was: 400 sccm Ar, 100 sccm 10% SiH4:Ar, at a pressure of 900 mTorr, a temperature of 350°C, and with an RF bias of 200 W.

3) On the photoconductive layer, a 100-150 nm Al_2O_3 was deposited by atomic layer deposition (ALD) (Picosun Sunale R150), with a thickness of 1Å per pulse. Chamber temperature was 300°C.

4) On the ALD layer, a 25 nm Teflon layer was formed by spin-coating 0.2% Teflon AF film (Dupont, Wilmington, DE) at 3000 rpm for 30s.

A.2. Top Cover Fabrication

1) The ITO coated 6" glass wafers were acquired from Thin Film Devices Inc. (Anaheim, CA). Thicknesses of ITO deposited are 2800 ± 100Å, with resistivity 10 ± 2 ohms/sq. The glass substrate used was 0.7mm ± 0.1mm thick Corning Eagle XG glass.

2) On the ITO layer, a 25 nm Teflon layer was formed by spin-coating 0.2% Teflon AF film (Dupont, Wilmington, DE) at 3000 rpm for 30s.

Appendix B Single-Sided Optoelectrowetting Device Fabrication

B.1. Single-Sided OEW Device Fabrication

1) ITO coated 6" glass wafers were acquired from Thin Film Devices Inc. (Anaheim, CA). Thicknesses of ITO deposited are 2800 ± 100Å, with resistivity 10 ± 2 ohms/sq. The glass substrate used was 0.7mm ± 0.1mm thick Corning Eagle XG glass.

2) On this substrate, on the ITO coated side, a 1-μm-thick photoconductive a-Si:H layer was deposited via plasma-enhanced chemical vapor deposition (PECVD) (Oxford Plasmalab 80plus) - The a-Si:H recipe was: 400 sccm Ar, 100 sccm 10% SiH4:Ar, at a pressure of 900 mTorr, a temperature of 350°C, and with an RF bias of 200 W.

3) On the photoconductive layer, a 100-150 nm Al_2O_3 was deposited by atomic layer deposition (ALD) (Picosun Sunale R150), with a thickness of 1Å per pulse. Chamber temperature was 300°C.

4) On the ALD layer, photoresist LOR 3A (MicroChem Corp. Westborough, MA) was spun on at 5000 rpm for 30 seconds, followed by bake for 5 minutes at 200°C. On the LOR-3A photoresist, 1.1-μm I-line photoresist was spun on at 4100 rpm for 30 seconds. The I-line photoresist was then soft baked for 90 seconds at 90°C.

5) The photoresist layers were then exposed with Karl-Suss-MA6 Mask Aligner and developed with OPD 4262 developer solution.

6) Titanium at 5 nm and Gold at 25 nm was then evaporated onto the wafer surface at a pressure of 10^{-6} Torr.

7) Wafer was then soaked with Remover PG photoresist stripper (MicroChem Corp. Westborough, MA) to lift-off of photoresist and the metal deposited on the photoresist. The metal mesh ground is left behind after the lift-off.

8) On the ALD and metal mesh ground layer, a 25 nm Teflon layer was formed by spin-coating 0.2% Teflon AF film (Dupont, Wilmington, DE) at 3000 rpm for 30s.

Appendix C Isothermal Polymerase Chain Reaction Protocol

C.1 PCR Master Mix Protocol

Set up a 50 µl reaction in a MicroAmp optical tube (Applied Biosystems) in a PCR Workstation.

1	Water	X µl
2	10X Annealing buffer II	5.0 µl
3	$MgSO_4$ (100 mM)	2.0 µl
4	NaCl (500 mM)	4.0 µl
5	IsoAmp dNTP Solution	3.5 µl
6	DNA template	X µl
7	Forward Primer (5 µM)	0.75 µl
8	Reverse Primer (5 µM)	0.75 µl
9	IsoAmp III Enzyme Mix	2.0 µl
10	EvaGreen (20X, Biotium)	0.5 µl
11	ROX Reference Dye (50X, Invitrogen)	1.0 µl
12	**Total Volume**	**50.0 µl**

Where X values for water and DNA template are varying, but overall total volume should be 50.0 µl.

Appendix D Optoelectronic Tweezers (OET) Device Fabrication and Surface Functionalization

D.1. OET Device Fabrication

1) ITO coated 6" glass wafers were acquired from Thin Film Devices Inc. (Anaheim, CA). Thicknesses of ITO deposited are 2800 ± 100Å, with resistivity 10 ± 2 ohms/sq. The glass substrate used was 0.7mm ± 0.1mm thick Corning Eagle XG glass.

2) On this substrate, on the ITO coated side, a 1-μm-thick photoconductive a-Si:H layer was deposited via plasma-enhanced chemical vapor deposition (PECVD) (Oxford Plasmalab 80plus) - The a-Si:H recipe was: 400 sccm Ar, 100 sccm 10% SiH4:Ar, at a pressure of 900 mTorr, a temperature of 350°C, and with an RF bias of 200 W.

D.2. Sulfo-SANPAH crosslinker and Collagen I Conjugation Protocol

Sulfo-SANPAH Conjugation

- Weigh out 0.5 mg of Sulfo-SANPAH per chip
- Use 5 µl of DMSO (*# of chips) to dissolve the Sulfo-SANPAH into solution
- Add 250 µl (*# of chips) of 50 mm HEPES buffer to the tube
- Pipette 250 µl onto each chip
- Put under UV light for 5 min. @ RT
- Wash three times with 200 mm HEPES buffer for 5 min. per wash @ RT

Collagen I Conjugation

- Make 250 µl of 0.2 mg/ml Collagen I solution per chip (Stock solution of Rat Tail Collagen type I is diluted with 0.1% acetic acid)
- Pipette 250 µl per chip and incubate for 1 hr @ RT
- Wash three times with 1x PBS for 5 min. per wash @ RT

D.3. Immunostaining for Collagen I Protocol

- Block with 1% BSA for 30 min. @ RT
- Add 250 µl of anti-Collagen I primary antibody (diluted 1:200) per chip. Keep @ 4°C overnight. (Abcam (ab34710): Rb antibody to Collagen I)
- Wash three times with 1x PBS for 5 min. per wash @ RT
- Add 250 µl of Alexa Fluor 633 anti-rabbit secondary antibody (diluted 1:500) per chip. Keep @ RT for 45 min.
- Wash three times with 1x PBS for 5 min. per wash @ RT
- Image

D.4. Polyethylene Glycol (PEG) Silanization Protocol

- Solublize PEG-silane (PEG-Silane, Molecular Weight 30kDa, acquired from Laysan Bio, Inc., Arab, AL) in 95% Ethanol (5% deionized water) in a 1.5% weight/volume ratio
- Add 250 µl Solublize PEG onto OET device surface (total area 2 cm by 2 cm), at 65°C, solute should dry within minutes, leaving a film of PEG-silane over the device surface
- Bake device with surface PEG-silane at 65°C for 16 hours
- Soak device in deionized water to wash off excess PEG-silane